

*Synthesis of Chitosan:UiO-67
Beads and Preliminary
Catalytic Testing using
Methanol Conversion*

Master thesis in Nanomaterials Science

O'Beirn, N. (Naoise)
n.obeirn@students.uu.nl

Abstract:

Composites of chitosan (CS), an abundant biopolymer derived from the exoskeletons of crustaceans, and UiO-67, a metal organic framework (MOF) which exhibits high chemical and thermal stability, were drop-casted in different ratios using an acetic acid solution in an attempt to produce stable beads which may be used for useful applications such as catalysis. The CS, MOF, and composite beads were characterised using ATR-IR spectroscopy, XRD, SEM-EDX, and N₂ physisorption. CO-IR was used to identify the presence of catalytic acid sites on the MOF while TGA was used to study the thermal properties of the MOF, CS and composite beads. The results of these characterisations indicated that bead drop-casting using the acetic acid solution was degrading the MOF structure. Stability tests in acetic acid were conducted to study the effects of acetic acid on the MOF structure. Methanol (MeOH) conversion was chosen as a test reaction which was carried out on the pure MOF and CS:MOF beads to study the catalytic acid sites of the MOF and how they are affected when combined with CS in a bead. MeOH conversion is also an environmentally relevant process since MeOH can be converted into dimethyl ether (DME) which can be used as an alternative fuel source to conventional liquid petroleum gases. Mechanical degradation was seen when preparing the MOF for catalysis. MeOH conversion was observed in the MOF and a 1:4 CS:MOF ratio bead. Two unknown products were formed during MeOH conversion most likely as a consequence of the MOF being degraded by the acetic acid solution in drop-casting. Further in-situ data of these products and the effects of catalysis are needed, however.

Abbreviations:

Abbreviation	Meaning
MOF	Metal organic framework
SBU	Secondary building unit
UiO	University of Oslo
CS	Chitosan
NP	Nanoparticle
IUPAC	International Union of Pure and Applied Chemistry
BPDC	Biphenyl-4,4'-dicarboxylic acid
DMF	N,N-dimethylformamide
IR	Infrared
ATR	Attenuated total reflectance
XRD	X-ray diffraction
TGA	Thermogravimetric analysis
SEM	Scanning electron microscopy
EDX	Energy dispersive X-ray
SE	Secondary electron
BSE	Backscattered electron
RPM	Rotations per minute
DCM	Dichloromethane
AA	Acetic acid
UiO-67 BA	UiO-67 with benzoic acid modulator
UiO-67 AA	UiO-67 with acetic acid modulator

Contents

Abstract:.....	1
1 Introduction	5
1.1 Metal Organic Frameworks: Definition, Characteristics, Structure, and Synthesis.....	5
1.2 Chitosan: Definition, Characteristics, and Structure.....	8
1.3 CS:MOF Composites.....	8
1.4 Test Reaction: Methanol Conversion.....	9
1.5 Characterisation Principles	9
1.6 Project Aim and Research Question	16
2 Experimental Methods.....	18
2.1 Synthesis of UiO-67 Using Benzoic Acid and HCl (UiO-67 BA)	18
2.2 Synthesis of UiO-67 Using 30 Equivalents of Acetic Acid (UiO-67 AA)	18
2.3 1% Chitosan Solution	18
2.4 CS:UiO-67 Composites	18
2.5 Alkali Method: Bead Formation Without Freeze Drying	20
2.6 Alkali Method: Bead Formation with Freeze Drying.....	20
2.7 Drop-Casting CS in Liquid N ₂	20
2.8 With Different Bead Formation Times.....	20
2.9 Direct Drop-Casting of 1:4 Ratio Bead with Liquid N ₂	20
2.10 Material Characterisation	21
3 Results and Discussion:	21
3.1 CS and UiO-67 Characterisation:.....	21
3.2 Sieving for the Effective Dispersion of MOF crystals:	30
3.3 Different Drop-Casting Techniques and their Efficacy for Producing CS:UiO-67 Beads:	31
3.4 Bead Characterisations	33
4. MeOH Conversion Test Reaction	54
4.1 ATR-IR Results of Catalysis and Sample Preparation	55
4.2 XRD Results of Sample Preparation and Catalysis	57
4.3 Product Selectivity and MeOH Conversion Using a Modified Setup	59
4.4 MeOH Conversion Using a Linkam Cell.....	69
4.5 Pre- and Post-Catalysis SEM-EDX Regional Analysis of 1:4 Bead.....	70
5. Conclusions and Outlook	71
6. Acknowledgements.....	73

7. References 73

1 Introduction

The majority of the work carried out involved the synthesis and characterisation of Chitosan: Metal Organic Framework beads. Chitosan (CS) was chosen because it is the second-most abundant biopolymer in the world after cellulose¹. CS is also soluble in aqueous acids and has strong affinities for metal ions². These properties have made CS an attractive candidate for catalyst supports which would give it a new useful purpose instead of being discarded as a waste product. The catalyst that will be hosted in the CS matrix for this project is the porous, crystalline metal organic framework (MOF) UiO-67. UiO-67 is a Zr cluster-based MOF which exhibits strong thermal and chemical stability. The composites of CS:UiO-67 were shaped as beads since in industry catalyst powders have associated diffusion limitations which may result in pressure drops in catalytic reactor vessels. Shaping the MOF in CS as a bead also allows for it to be retrieved after the catalytic process has been completed i.e., less waste. Previous studies have shown that UiO-67 is catalytically active for CO₂ hydrogenation which can be used to produce methanol (MeOH)³. This is an environmentally relevant process since it can reduce the amount of CO₂ (a harmful greenhouse gas) in the atmosphere while producing useful chemical compounds. CO₂ conversion is made possible by the presence of defect sites in the Zr-nodes of the MOF framework. These defect sites afford UiO-67 with reactive Lewis acid sites which confer catalytic activity. For this thesis the catalytic conversion of MeOH to dimethyl ether (DME) was chosen as a test reaction to study the acid sites of UiO-67 in its pure form and when it is incorporated into a CS matrix as a bead. DME is a promising alternative fuel source to conventional liquid petroleum gases (LPGs). CO₂ emissions are 30 – 80% lower for DME compared to traditional LPGs making it an environmentally benign fuel. The following sub-sections will discuss the materials and methods used throughout this master's thesis.

1.1 Metal Organic Frameworks: Definition, Characteristics, Structure, and Synthesis

Metal organic frameworks (MOFs) are composed of metallic ions that are connected through organic linkers known as secondary building units (SBUs)⁴. Additional chemical functionality can be added to the linkers to promote desirable properties through post-synthetic modification⁵. According to IUPAC "A metal-organic framework, abbreviated to MOF, is a coordination network with organic ligands containing potential voids"⁶. They have an organic-inorganic duality and exhibit attractive properties i.e., ultrahigh porosity, adjustable pore sizes, and large internal surface areas (above 6000 m² g⁻¹)⁷. The properties of MOFs make them ideal candidates as host frameworks for catalytic applications. The ability to functionalise the linker SBUs allows for the homogenous-phase catalysts to be present in the solid state⁸. The MOF being used for this thesis is UiO-67, a zirconium-based MOF developed by the University of Oslo⁹. The zirconium oxide metal clusters (Zr₆O₄(OH)₄) are connected by biphenyl-4,4'-dicarboxylate (BPDC) linkers as can be seen in Figure 1, reproduced from Reference 9⁹. These linkers form octahedral cages which gives the MOF its structure. The detailed structure of the BPDC linker is given in Figure 2. Zirconium-based MOFs are renowned

for their mechanical and chemical stability¹⁰. X-ray powder diffraction (XRPD) and thermogravimetric analysis (TGA) data have shown that UiO-67 can remain stable up to 450 °C¹¹. The framework possesses both octahedral and tetrahedral cavities (23 and 11.5 Å, respectively). As a result, UiO-67 has a remarkably large surface area (2700 m² g⁻¹ when 12 linkers are bound to each Zr node⁹).

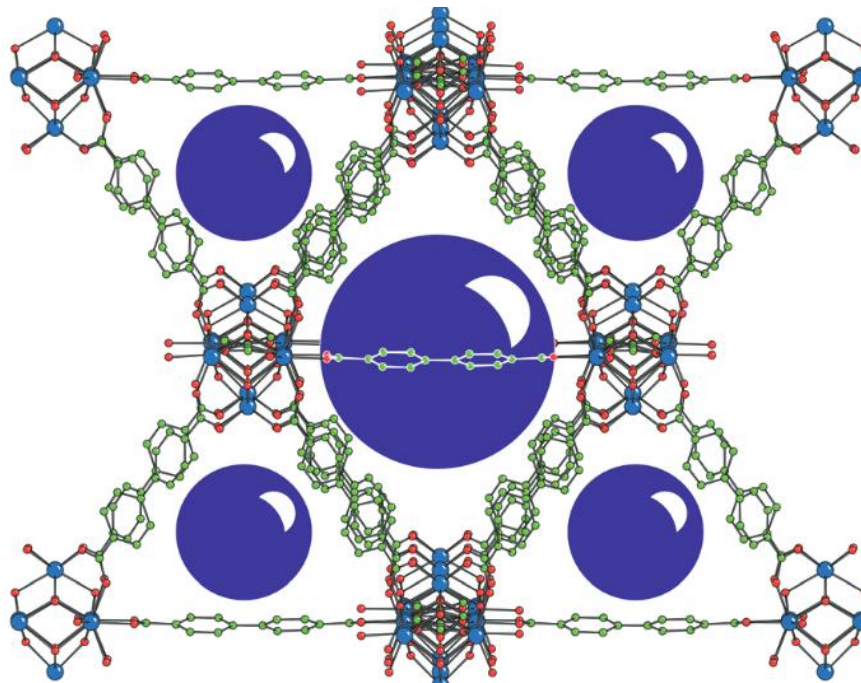


Figure 1. UiO-67 structure showing Zr nodes (blue spheres), BPDC linker (green spheres), an octahedral cage (large purple sphere), and tetrahedral cages (small purple spheres). Reproduced from reference 9.

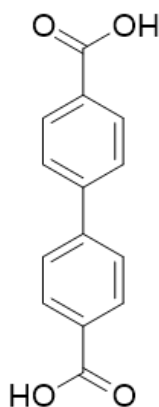


Figure 2. BPDC linker structure

As a sidenote for potential work in the future the BPDC linker may be modified with other metal ions e.g. Pt nanoparticles (NP). To achieve this a number of methods may be employed to functionalise the linkers. The methods include pre-made linker synthesis (PMLS)⁸, post-synthetic functionalization (PSF)⁵, and one pot synthesis (OPS)¹². PMLS involves the coordination of a metal species (Zr in this case) to a functionalised linker molecule. These are then mixed in with the rest of the components that are needed for the synthesis of UiO-67. Alternatively, PSF attaches the linker to the metal species after the synthesis of UiO-67 is

complete. OPS, the crudest of the methods, mixes all the precursors together to form the UiO-67 framework. The method of synthesis can indeed affect the characteristics of the resultant MOF as demonstrated in Table 1.

Table 1. Sample characteristics for UiO-67 MOFs synthesised via PMLS and PSF³.

Sample	S_g (m^2g^{-1})	V_m (cm^3g^{-1})	Crystal size (μm)
UiO-67-Pt-PMLS	2442	0.96	2.5
UiO-67-Pt-PSF	2392	0.97	2
UiO-67-Pt-PSF, pellets	2305	0.94	2

The zirconium building block provides the MOF with high chemical and thermal stability. The inorganic node binds strongly to the organic linker and as a result confers the enhanced stability. This node has the formula $Zr_6O_4(OH)_4(CO_2)_{12}$ and is 12-coordinated. The incorporation of the linear organic linkers expands the cubic close packed structure of the MOF which provides it with its large surface area. In the case of UiO-67, BPDC moieties act as the organic linkers. TGA experiments have shown that at the temperature of lattice breakdown a benzene fragment is observed suggesting that the bond between the benzene rings and the terminal carboxyl group is the weakest point in the framework. The structure of the inorganic node is depicted in Figure 3, reproduced from Reference 13¹³. The faces of the Zr_6 octahedron are capped by alternating μ_3-O and μ_3-OH groups while carboxylate groups ($-CO_2$) bridge the polyhedron edges which results in the formation of the $Zr_6O_4(OH)_4(CO_2)_{12}$ cluster. This all leads to the formation of intergrown cubic crystals which can be as small as 1 – 2 μm . Charge stabilisation is achieved by the presence of four $-OH$ groups. The Zr_6 cluster can reversibly rearrange when μ_3-OH groups are added or removed¹⁴ which makes it structurally flexible.

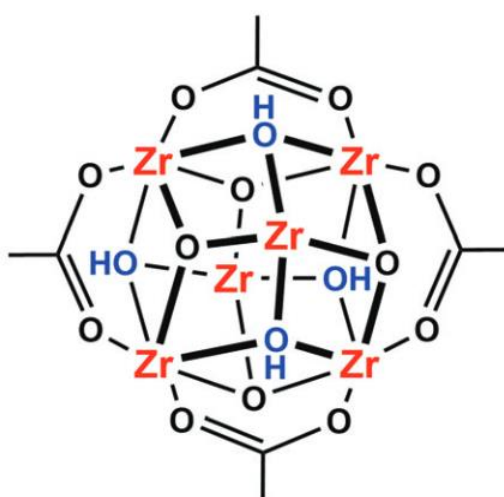


Figure 3. Structure of $Zr_6O_4(OH)_4$ node in UiO-67 showing four of the 12 coordinated BPDC linkers. Reproduced from reference 13.

1.2 Chitosan: Definition, Characteristics, and Structure

Chitosan (CS) was chosen for this project due to its large abundance and attractive properties as a biodegradable host material for catalysts. CS is the *N*-deacetylated derivative of chitin which is a mucopolysaccharide found in the exoskeletons of marine crustaceans. CS is formed when the degree of deacetylation of chitin is at least 50%¹⁵. The -NH₂ moiety at the C2 position allows the polysaccharide to behave like a polyelectrolyte. The chemical structure of CS is depicted in Figure 4, reproduced from Reference 17. Chitin is a highly insoluble material with low chemical reactivity while CS on the other hand is soluble in aqueous acids (e.g. acetic acid) due to the deacetylation of its nitrogen atom. This solubility means that CS can be used in a wide variety of applications (flocculants, antibacterial agents, drug delivery)¹⁶ and can be synthesised in many shapes (powders, beads, pellets, films) making it more versatile than chitin. The fact that CS is soluble in aqueous acidic media is a focal point of this project since drop-casting of CS solutions to form beads with different ratios of CS:MOF will be conducted.

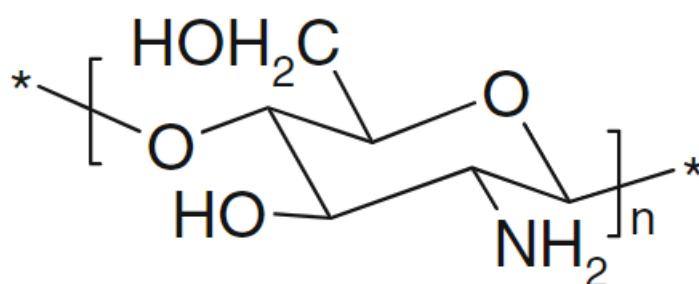


Figure 4. Chemical structure of CS showing the deacetylated amine at C2 position. Reproduced from reference 17.¹⁷

However, the improved processability of CS over chitin comes at a price since the stability of CS and its derivatives tend to be lower when compared to chitin¹⁷. The improved processability of CS is due to the presence of the amine moiety at the C2 position which can form complexes with metal ions which is a key process for this project since the MOF will need to interact with the CS when the two are combined in a bead. The sorption of metal ions is possible on CS due to the presence of amine groups which possesses a nitrogen atom with a free electronic doublet. This electronic doublet is available at near neutral pH which is an important parameter for metal ion sorption¹⁸. The efficiency of this complex formation is linked to the degree of deacetylation of the methyl amide from chitin. This implies that complex formation is related to the abundance of -NH₂ and its distribution¹⁵. Metal ions may interact with CS in a number of ways. The three most common mechanisms are i) metal chelation; ii) electrostatic attraction (ion exchange); and iii) through the formation of ion pairs. For catalysis, the two main modes of metal ion sorption on CS are chelation and electrostatic attraction.

1.3 CS:MOF Composites

As discussed in the previous section CS is an attractive host material for catalytic metal species because of its high sorption capacity, its affinity toward metal ions (due to amine groups present in the polymer), and its physico-chemical versatility. It can also be manipulated to form different shapes such as fibres, sheets, and beads. For this project we have chosen to synthesise beads with different ratios of CS to UiO-67 to see how the concentrations of the two materials affect the properties of the beads. To be able to synthesize polymer-MOF

hybrids which retain the desirable properties of both materials is an attractive concept (i.e., the abundance of CS produced as a biodegradable host material and the physico-chemical stability of UiO-67). Embedding a MOF into a biodegradable polymer would increase the number of its potential applications since its crystal structure may make it incompatible with certain technologies¹⁹.

CS-based beads may be produced when the CS is dissolved in an acetic acid (AA) solution which is subsequently drop-casted through a needle into a basic solution. A dehydration reaction occurs and the composite beads are formed. Alternatively, the CS and MOF may be added to an AA solution which will then be drop-cast directly into liquid nitrogen. This freezes the beads in place which are subsequently freeze dried to maintain their shape and expel any water present. These techniques for bead synthesis will be investigated throughout this project. Beads are useful because they may be loaded into and unloaded from reactor vessels with minimal loss of the catalytically active material.

1.4 Test Reaction: Methanol Conversion

As mentioned in the introduction to this thesis, the acid sites of UiO-67 will be probed using MeOH conversion as a test reaction. In addition to this, the influence of mixing CS with UiO-67 on these acid sites will also be studied. If this reaction is successful the CS:UiO-67 beads may be used to catalyse the formation of useful compounds such as dimethyl ether (DME). DME is the simplest ether compound which has a promising future as an alternative, clean fuel source to replace traditional liquid fuels. To the best of our knowledge, DME catalytic synthesis via UiO-67 incorporated into a CS matrix has not been reported previously. The consequences of embedding UiO-67 in chitosan to produce a composite and then forming beads from these composites will be studied in terms of the change in catalytic activity with respect to methanol conversion using pure MOF i.e., how the acid sites of the MOF are affected when CS is present.

1.5 Characterisation Principles

The following subsections will discuss the underlying principles of the characterisation techniques that were used throughout this project as well as the reasoning for choosing them.

1.5.1 Attenuated Total Reflectance (ATR) Infrared (IR) Spectroscopy

Attenuated total reflectance (ATR) infrared (IR) spectroscopy is a contact sampling technique which will be used in this project to characterize the materials being employed i.e., UiO-67, CS, and the beads that will be formed from their composites. An IR beam travels from a crystal which has a medium to high refractive index into the sample which has a comparatively lower refractive index. At a certain angle of incidence all of the light waves from the beam will be reflected back. This is known as total internal reflection. Some of the light will escape and travel a distance of 0.1 – 5µm from the crystals surface as waves known as evanescent waves. These waves may be absorbed by the sample when it is placed on the crystal's surface which is depicted in Figure 5. This absorbance yields the sample's IR absorption spectrum which gives information about the functional groups present²⁰

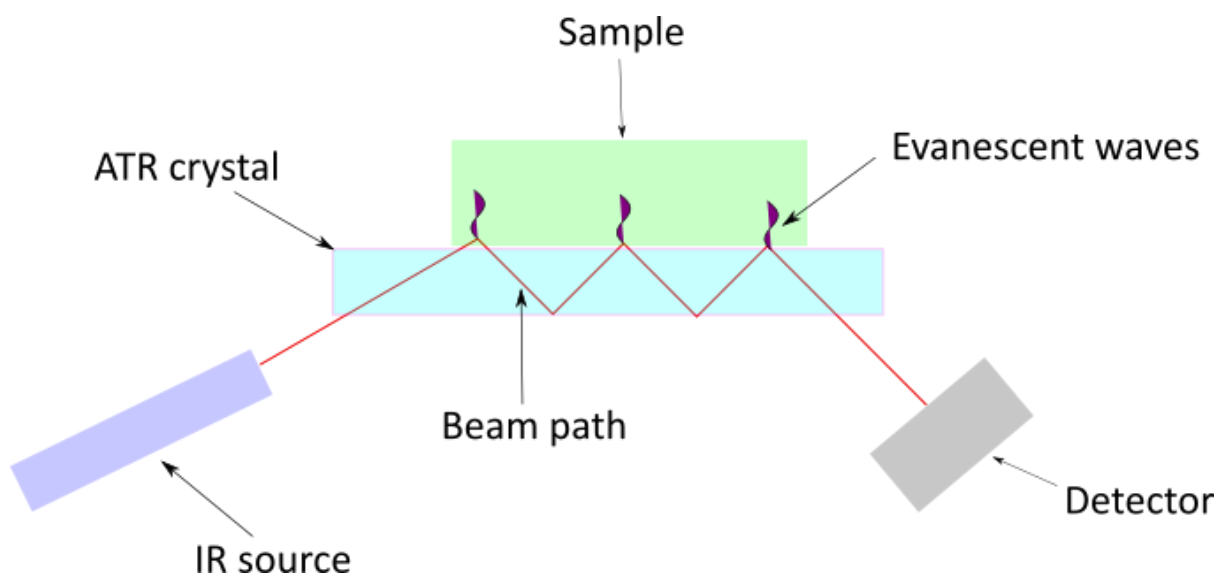


Figure 5. ATR-IR setup and working principal. An IR beam passes through the ATR crystal which has a higher refractive index than the sample. A portion of the incoming light will travel from the crystal to the sample in the form of evanescent waves. The absorbance of these waves yields an IR spectrum of the sample²⁰.

1.5.2 X-ray Diffraction (XRD)

X-ray diffraction (XRD) works on the principle of X-rays being scattered from electrons in the atoms being studied. A relative phase shift is picked up by the detector which gives information about the position of the atoms. These measurements can be used to determine the crystal structure of UiO-67 since the wavelength of the X-rays are on the same length scale as the distance between the atoms in the crystal lattice of the MOF²¹. The Bragg Law, Equation 1, is used to evaluate the structural information relating to the MOF, where λ is the wavelength of the X-ray. This technique is based on the principle of X-rays being reflected by the lattice planes of the material. These parallel planes (also known as Miller indices) are characterised by a triplet index hkl . The parallel planes are separated by the distance d_{hkl} . 2θ is the diffraction angle i.e., the angle that arises between the incident and outgoing X-rays. Figure 6, reproduced from Reference 22, shows the simplified geometry of X-ray diffraction.

$$n\lambda = 2d_{hkl}\sin\theta$$

Equation 1. The Bragg Law which explains the working principle of XRD. λ is the wavelength of the X-ray, and d_{hkl} is the spacing between the parallel lattice planes which is characterised by a triplet index (hkl). 2θ is the diffraction angle between the incident and outgoing x-rays²².

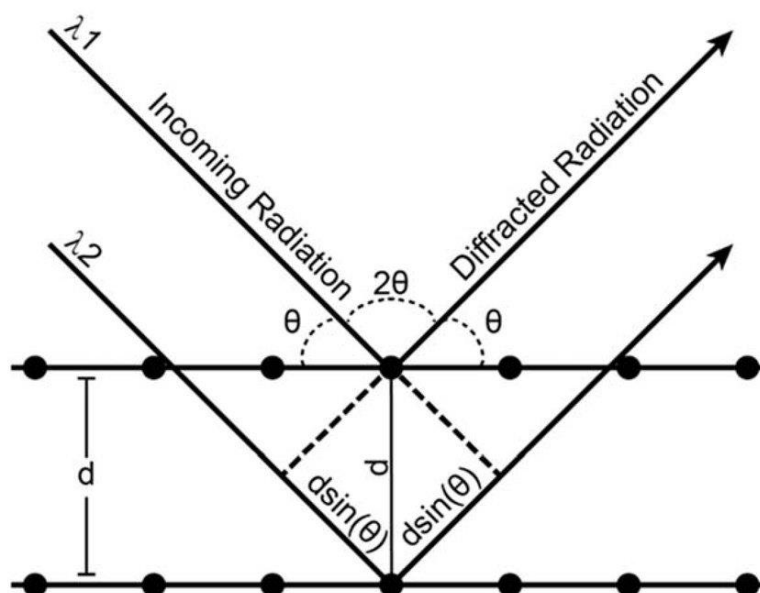


Figure 6. Geometry of simplified Bragg's law. The black spheres represent the crystal lattice of the material. λ_1 and λ_2 are the wavelengths of the two incident X-rays. 2θ is the diffraction angle between the incoming and diffracted X-rays. d is the spacing between adjacent lattice planes. Reproduced from Reference 22²².

Gutterød *et al.*³ demonstrated through XRD spectra that the microcrystalline lattice of UiO-67-Pt-PSF was stable under the experimental conditions they subjected it to as seen in Figure 7, reproduced from Reference 3. XRD data can give information about the structural integrity of the MOF “after pressing, pre-activation and testing”³. This will be important for this thesis since the CS:MOF composites will be subjected to different physical and chemical parameters i.e., drop-casting in liquid nitrogen to form beads and pelletising/sieving prior to catalytic tests. XRD will be used to study the crystallinity of the materials used in this project as well as the structural changes that may occur when they are processed.

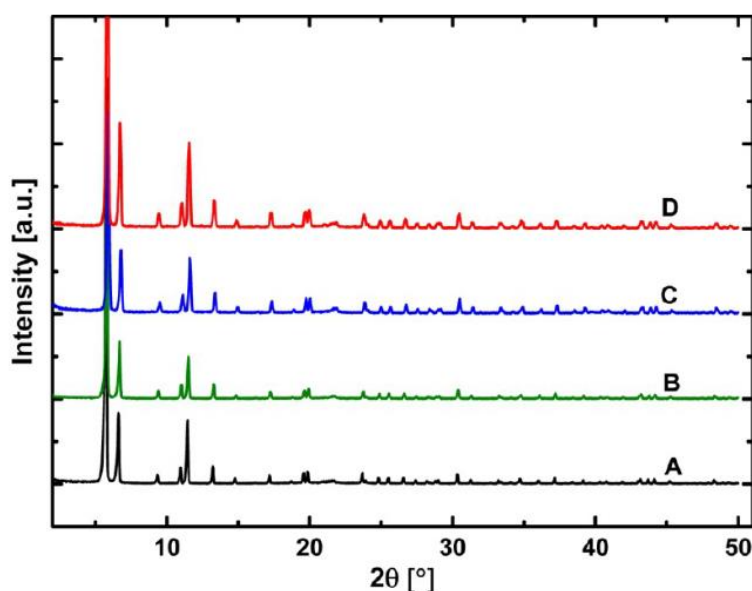


Figure 7. XRD data of UiO-67-Pt-PSF as a powder (A), pellet (B), after pre-activation in 10% H₂/Ar followed by testing for CO₂ hydrogenation; not relevant to this project (C), and UiO-67- bipy; not relevant to this project (D). Reproduced from Reference 3³.

1.5.3 N₂ Adsorption Isotherms

N₂ physisorption is used to determine surface area and pore size distribution of porous materials via physical adsorption (physisorption) at 77 K. To interpret the nitrogen isotherm, one must determine the mechanism of physisorption i.e., monolayer-multilayer adsorption, capillary condensation or micropore filling²³. Adsorption isotherms are taken at constant temperatures and can be described by Equation 2. n^a is the amount of gas adsorbed by the analyte and p/p^0 is the equilibrium relative pressure. The shape of the isotherm gives details about the type of gas – solid interaction that is occurring.

$$n^a = f\left(\frac{p}{p^0}\right)_{T, \text{ gas, solid}}$$

Equation 2. Adsorption isotherm equation for a porous solid at a constant temperature. n^a is the amount of gas adsorbed and p/p^0 is the equilibrium relative pressure.

The material being studied (i.e., the adsorbent) can be classified according to the size of their pores. Porous adsorbents can be classified as microporous (diameters less than 2 nm), mesoporous (2 – 50 nm), and macroporous which are not significant in nitrogen physisorption. Nitrogen isotherms themselves exist in a number of forms. Type II isotherms are related to non-porous solids which exhibit monolayer – multilayer adsorption. Type IV isotherms are the same as Type II until capillary condensation occurs in the mesoporous parts of the material. Type I isotherms are related to micropore filling at low p/p^0 . Identifying the type of isotherm allows for an estimation of the physisorption mechanism which is occurring²³. N₂ adsorption isotherms (Figure 8, inset, reproduced from Reference 9) also give information about the pore-size distribution. As an example, the results in Figure 8 indicated that the octahedral pore sizes for UiO-67, UiO-67-NO₂, and UiO-67-NH₂ had a diameter of 23, 21, or 21.5Å, respectively.⁹

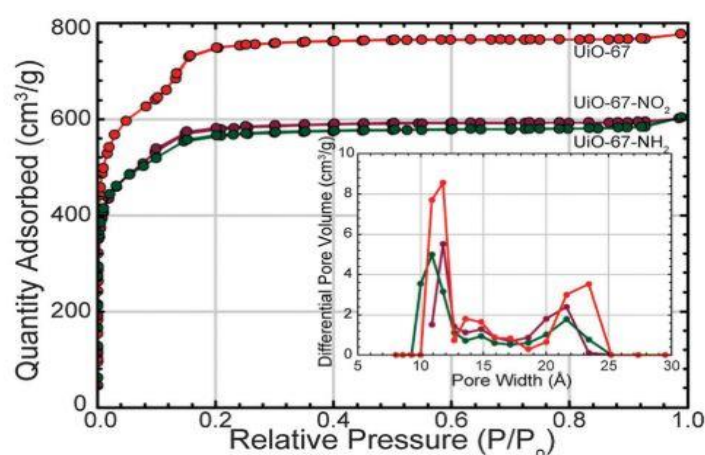


Figure 8. N₂ isotherm showing a step at approximately 0.1 p/p^0 on account of the two types of pores present in UiO-67 (see Figure 1). Inset shows N₂ adsorption isotherms of UiO-67 and derivatives with associated pore volumes. Reproduced from Reference 9⁹.

1.5.4 Carbon Monoxide IR (CO-IR) for UiO-67 Acid Site Analysis:

In carbon monoxide (CO) adsorption spectroscopy CO molecules adsorb to the surface of the MOF species when the pressure of CO applied is increased. UiO-67 and other Zr-based MOFs have undercoordinated metal sites present as a result of missing linker and node defects (the number of which can be increased via the use of AA as a modulator). The concentration of these defects is indicative of the potential catalytic activity of the MOF structure²⁴. CO adsorption spectroscopy can be used to determine the types of defect sites present within UiO-67 (i.e., Lewis or Bronsted acid sites) and the types of interactions that are occurring between the two species. This is achieved by examining the spectra of the adsorbed CO and comparing it with the spectrum of the free CO molecule. CO interacting with a Lewis acid site for example will lead to a blue-shift relative to the free gas molecule since the electron density at the carbon atom of CO is donated to the electron deficient Lewis acid site on the MOF²⁵. CO-IR will therefore be used to analyse the acid sites present in UiO-67.

Figure 9 shows a schematic workflow for CO-IR spectroscopy. To effectively dose the MOF with CO the water molecules present at the MOF surface and within its interior are evacuated under ultra-high vacuum (UHV). The chamber containing the sample is then dosed with CO at $-188\text{ }^{\circ}\text{C}$ so that the CO molecules can effectively interact with the MOF surface and there is less thermal motion, so they do not leave the MOF surface easily. Higher pressures of CO being applied afford more interactions between CO and the MOF surface which gives rise to sharp characteristic peaks in the adsorption spectra of CO. This can be attributed to the type of interaction between the acid site and the CO molecule. Therefore, CO-IR is a useful technique for evaluating the acid site characteristics of the MOF.

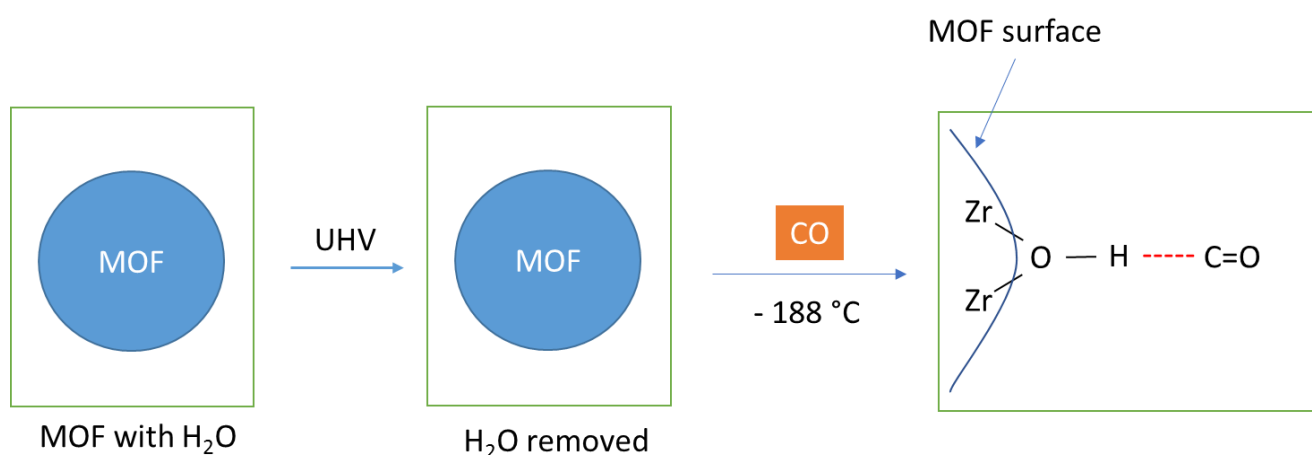


Figure 9. Schematic workflow of CO-IR spectroscopy. MOF has its water content removed under UHV. The chamber holding the sample is then dosed with CO at $-188\text{ }^{\circ}\text{C}$. CO molecules interact with the acid site of the MOF surface.

1.5.5 Scanning Electron Microscopy (SEM):

Scanning electron microscopy (SEM) is a versatile imaging technique which has applications in material science, forensics and the semiconductor industry. A variety of electron sources may be used such as a CeB₆ source in our case. The incident beam of SEM can have a diameter from 10 to 1 nm when a field-emission source is used. This technique will prove invaluable to the project since the MOF particles which will be incorporated into the CS matrix are present at the nano-meter scale. The electron beam which hits the sample leads to a number of electron emissions such as secondary electrons (SE) and back-scattered electrons (BSE)²⁶.

These electrons are then registered by a detector which processes the signal to yield an image of the sample. SEM is a very useful technique which will be utilised frequently during this project to elucidate the morphology of the CS and UiO-67 structures that will be synthesized. Figures 10 and 11 show examples of SEM images of CS²⁷ and UiO-67-Pt-PSF powder³, reproduced from References 27 and 3, respectively.

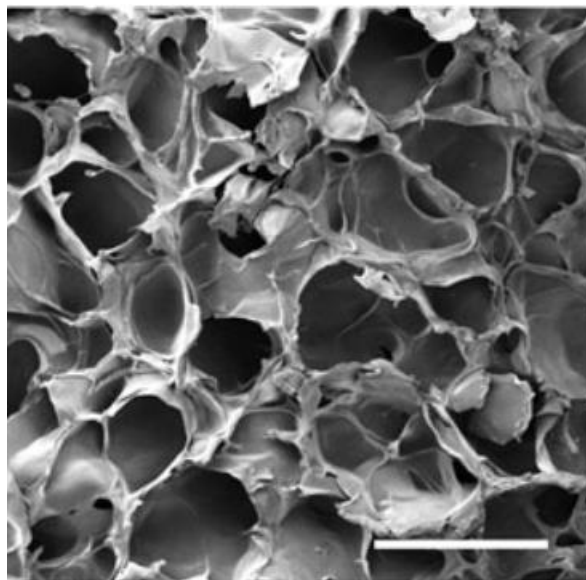


Figure 10. SEM image of CS. Scale bar = 200 μm . Reproduced from Reference 27²⁷.

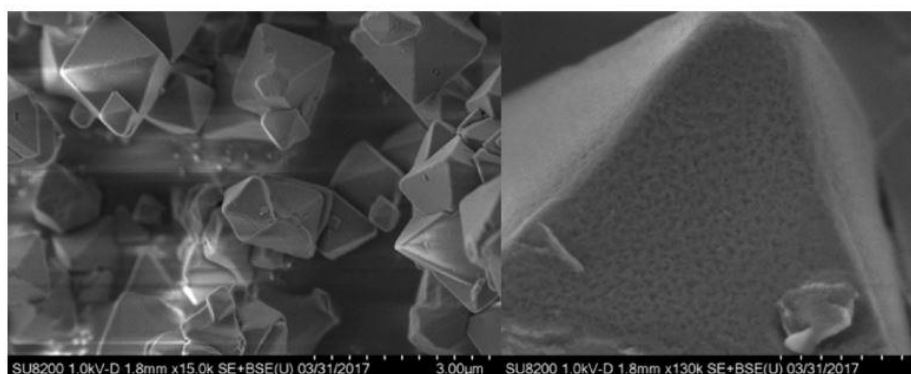


Figure 11. SEM image of UiO-67-Pt-PSF as a powder showing its characteristic bipyramidal morphology. Reproduced from Reference 3³

1.5.6 Scanning Electron Microscopy Energy-Dispersive X-ray (SEM-EDX) Analysis

EDX will be used in tandem with SEM to gain further insight into the chemical nature of the beads that will be synthesised in this project. The inner shells of the atoms present in the beads are hit with an electron beam which displaces the electron present in the target shell. This leaves a positively charged “hole” which attracts an electron from a higher energy outer shell of the atom. The electron filling this lower energy inner shell hole releases an X-ray which has an energy equal to the difference in energy between the higher (outer) and lower (inner) energy shells as can be seen in Figure 12, reproduced from Reference 28. The energy of the X-ray and the transition itself are both element-specific. A silicon drift detector collects the information contained within this X-ray and produces a unique chemical fingerprint of the sample. This technique can be used to study a single point or a given area of a sample. The

latter measurement is referred to as a “map”. The concentrations of the different atoms present may also be determined via EDX²⁸. It is therefore both a quantitative and qualitative technique.

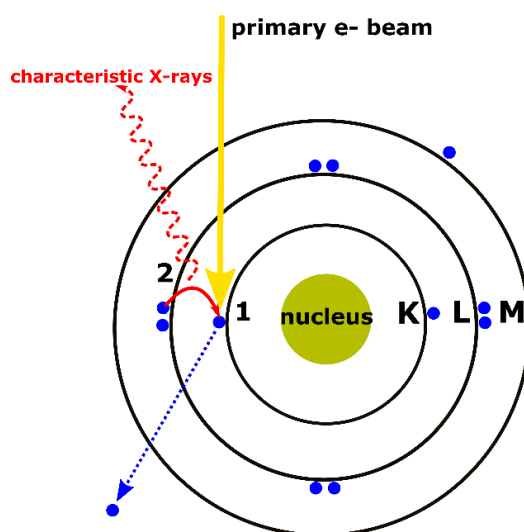


Figure 12. Working principle of EDX analysis. Incoming electron beam displaces an electron from the target shell creating a positively charged hole which is filled by an electron from an outer shell. This transition releases an X-ray characteristic of the sample. Reproduced from Reference 28²⁸

1.5.7 Thermogravimetric analysis (TGA)

Thermogravimetric analysis (TGA) is a thermal analysis technique which measures the change in weight of a material as a function of time (isothermal mode) or temperature (scanning mode). For this project the focus will lie with the scanning mode. The thermogravimetric (TG) curves produced give information about the material’s thermal properties. The technique can be used to measure the occurrence of thermal events (e.g. water loss) under a given set of conditions such as absorption, adsorption, and desorption (among others). It can also be used to detect the proliferation of volatile compounds. In addition, the thermal stability of the material may also be evaluated²⁹. TGA will be used in this project to evaluate the thermal properties of CS, UiO-67, and the beads that will be formed from their composites in different ratios. The effects of drop-casting and catalysis on the thermal properties of the materials will also be measured. Figure 13 depicts a schematic workflow of TGA.

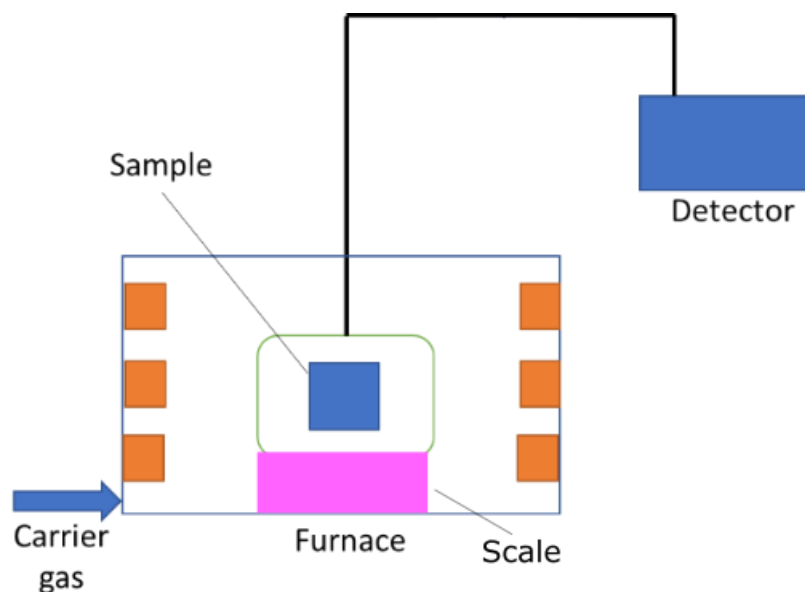


Figure 13. Schematic workflow of TGA. Sample is placed in furnace on a scale and the weight loss is measured as either a function of time or temperature.

1.6 Project Aim and Research Question

The main focus of this project is to develop a method for synthesizing CS:UiO-67 composites as beads and to determine which synthetic techniques produce beads which are stable and retain the desirable characteristics of the two materials as outlined in the introduction. To achieve this a variety of established synthetic techniques will be used e.g., drop-casting acidic solutions of the composite materials into alkali solutions. The efficacy of these synthesis techniques will then be evaluated using a number of analytical techniques. ATR-IR spectroscopy will be used to identify the functional groups present in CS and UiO-67. TGA will be used to study the thermal stability of the composites compared to the pure starting materials. CO-IR spectroscopy will be used to analyse the acid sites which the MOF possesses. SEM will be used to visualise the homogeneity of the MOF particles when they are added to the CS matrix and EDX will be used in tandem with SEM to get an indication of the chemical species present. The data obtained will be used to evaluate the properties of the beads and to see how future improvements can be made to the underlying synthetic approaches.

Beads were chosen since they can be retrieved from industrial catalytic reactors without losing the catalytically active material. CS was chosen as a host material for UiO-67 because it is produced in large quantities which ends up as a waste product. Recycling CS as a binder is therefore environmentally advantageous. With this in mind CS can be given a new purpose as a binder for catalytically active MOFs such as UiO-67. The effectiveness of CS as a binder for such an application will be studied. UiO-67 has received attention in the last few years because of its high thermal stability and large surface area. It has also been implicated as a catalyst for a number of different reactions due to the presence of its Lewis acid sites. MeOH conversion will be used as a probe reaction to test these acid sites in the presence and absence of CS. As an added bonus, MeOH conversion is an environmentally relevant process since it can be used to produce DME which can be used as an alternative fuel source. The presence of CS may affect the acid sites of UiO-67 which could have implications for MeOH conversion, i.e., the CS may block the acid sites of UiO-67 and so may affect the catalytic properties of the MOF. The effects of the different synthesis parameters on the acid sites of

the MOF will also be studied i.e. how will drop-casting affect the MOF structure and catalytic ability.

2. Experimental Methods

The following chapter provides the details of the experimental work conducted. Two different experimental procedures were tested to synthesize UiO-67. The first involved the use of benzoic acid (BA) as a modulator (UiO-67 BA) while the second used acetic acid (AA) as a modulator (UiO-67 AA). In the end AA was chosen as a modulator since CS could also be solubilised in it. For each MOF batch synthesised analytical measurements e.g., ATR-IR spectra, XRD, etc., were collected to determine whether the MOF had been produced. The analytical data obtained was compared with literature values to verify this. Different drop-casting methods were also tested for synthesising beads. All drop-casting methods involved the use of a syringe with a needle which had a diameter of 0.8 mm. First an alkali drop-casting method was tested and then a technique involving liquid nitrogen and freeze drying was tested.

2.1 Synthesis of UiO-67 Using Benzoic Acid and HCl (UiO-67 BA)

DMF (0.65 mol), HCl (1.72 mmol), and BA (21.50 mmol) were mixed together. This solution was then heated at 80 °C with continuous mixing at 150 rotations per minute (RPM). $ZrCl_4$ (2.15 mmol) was added to the solution. Biphenyl-4,4'-dicarboxylic acid (2.15 mmol) was added slowly with continuous mixing. The temperature was increased to 150 °C. The solution turned from white to transparent within a few seconds. The temperature was decreased to 120 °C and left for 24 hours. The solution was washed twice with 15 mL of DMF and three times with THF.

2.2 Synthesis of UiO-67 using 30 equivalents of acetic acid (UiO-67 AA)

$ZrCl_4$ (0.514 mmol) and AA (15.42 mmol) were dissolved in DMF (40 mL) via sonication for 1 min. Biphenyl-4,4'-dicarboxylic acid (0.514 mmol) was then added. This solution was heated to 120 °C with continuous stirring (150 RPM) for 24 hours. The solution was then cooled to room temperature and the precipitates were isolated via centrifugation and suspended in 10 mL of DMF for 2 – 6 hours. The DMF was decanted off and the solids were washed with ethanol. The solids were dried in an oven at 150 °C. The characterisation data obtained for this procedure and for the benzoic acid procedure were compared with literature values³⁰.

2.3 1% Chitosan Solution for Drop-casting

1 g of CS was dissolved in 100 mL of AA solution (1% v/v) with continuous stirring (150 RPM) at 60 °C for 24 hours or until a viscous solution was produced. This solution was used for drop-casting experiments.

2.4 CS:UiO-67 composites

The initial strategy for synthesising CS:MOF composite beads is depicted in Figure 14. First the MOF was synthesised. This was then added to the 1% CS AA solution to form the CS:UiO-67 composites which were produced in different ratios. The composites were then used to form beads either via an alkaline or liquid nitrogen drop-casting method with subsequent freeze drying.

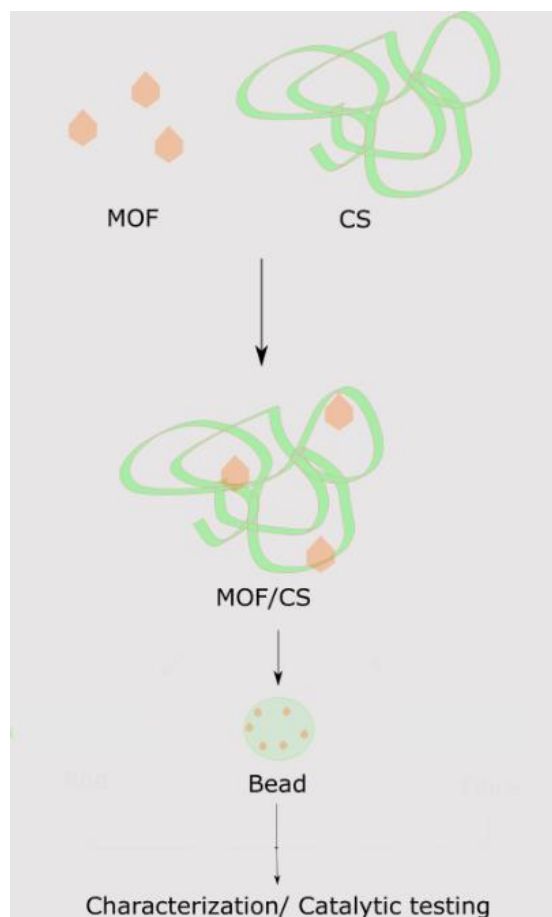


Figure 14. Synthesis strategy for CS:UiO-67 composites followed by shaping into beads. MOF crystals are depicted in orange. CS is represented by the green string. The composites are depicted in the middle and the beads formed from these composites are depicted at the end. Characterization techniques were used to determine the physical and chemical properties of the beads.

The composites were formed in ratios with increasing amounts of UiO-67. Table 2 provides details of the different ratios. The ratios 1:1, 1:2, 1:4, and 2:1 were synthesised with and without sieving using a 78 – 38 μm sieve to study the effects on UiO-67 dispersion within the CS matrix.

A 1% CS solution was prepared. The different masses of UiO-67 were added to this according to their ratios. The samples were stirred (150 RPM) overnight at 50 °C. The samples were then filtered over a Buchner funnel and dried at 60 °C in an oven for 48 hrs.

Table 2. Ratios of CS to UiO-67 in initial composite syntheses

Ratio CS:UiO-67	CS volume (mL)	UiO-67 mass (mg)
10:1	5	5
5:1	5	10
2:1	5	25
1:1	5	50
1:2	5	100
1:4	3	120

2.5 Alkali Method: Bead Formation Without Freeze Drying

Two different procedures were used for the drop-casting of CS:UiO-67 composites via an alkali method without freeze drying.

The first method involved adding solid UiO-67 AA (50.0 mg) to a 1% CS solution (5.0 mL). This was heated to 40 °C and stirred at 150 RPM for 24 hrs. The solution was then drop-casted into a 1.0 M NaOH solution. The beads formed were washed with deionised water over a Buchner funnel three times and dried in an oven overnight at 60 °C.

The second technique involved suspending solid UiO-67 AA (50.0 mg) in acetic acid (5.0 mL) with stirring (150 RPM) for 6 hrs. 2.5 mL of this solution was added to 5 mL of 1% CS solution. This was heated (40 °C) and stirred (150 RPM) for 24 hrs. The solution was then drop-cast into a 1.0 M NaOH solution. The beads formed were washed with deionised water over a Buchner funnel three times and dried in an oven overnight at 60 °C.

2.6 Alkali method: Bead Formation With Freeze Drying

2% CS solution (5.0 mL), UiO-67 AA (25.0 mg), and acetic acid (5.0 mL) were mixed in a beaker and then sonicated. This mixture was then drop-casted into a 1.0 M solution of NaOH. The resulting beads were transferred to a centrifuge tube where they were submerged in water and placed in a freezer overnight. The frozen beads were then freeze dried overnight.

2.7 Drop-Casting CS in Liquid N₂

The following methods included liquid N₂ as a means of freezing the beads in place after drop-casting. The beads were subjected to the liquid N₂ with and without washing.

The first method involved washing. A 2% CS solution (5.0 mL) was drop-cast directly into a 1.0 M NaOH solution. The beads formed were washed with H₂O three times and then placed in a liquid N₂ bath. The beads were subsequently freeze dried.

The same procedure described above was repeated except without washing i.e., the CS solution was drop-cast into the NaOH solution and then from there was added directly into liquid N₂. The beads were subsequently freeze dried.

2.8 With Different Bead Formation Times

2% CS solution (5.0 mL) was drop-cast directly into a 1.0 M NaOH solution. Half of the beads formed were left for 5 minutes and the other half were left for 30 minutes in the NaOH solution. Both samples were then washed three times with H₂O. The beads were transferred to separate centrifuge tubes where they were submerged in water and placed in a freezer overnight. The frozen beads were then freeze dried.

2.9 Direct Drop-Casting of 1:4 Ratio Into Liquid N₂

UiO-67 AA (80.0 mg) was sieved with a 38 – 78 µm sieve which was then sonicated for 5 mins. The smallest fraction (< 38 µm) was added to a 1% CS solution (2.0 mL) and mixed at 150 RPM for 1 hr at 60 °C. This was drop-cast directly into liquid N₂. The resulting beads were then

freeze dried overnight. The procedure was repeated with the same volume of 1% CS solution for a 1:2 (40.0 mg of UiO-67 AA) and 1:3 ratio (60.0 mg of UiO-67 AA).

2.10 Material Characterisation

ATR-IR spectra of the materials used were acquired using a Perkin Elmer Frontier FT-IR spectrometer with a universal ATR sampling accessory. 32 spectra were averaged per acquisition with a resolution of 4 cm^{-1} . A Bruker D2 Phaser was used for acquiring XRD diffractograms. TGA thermograms were obtained using a Perkin Elmer TGA 8000 analyser. GC-MS data was acquired using a Shimadzu QP2010 mass spectrometer which was fitted with an AOC-20i auto-injector. Carbon monoxide IR (CO-IR) spectroscopy was conducted using a Perkin Elmer System FT-IR 2000. A Pfeiffer HiCube vacuum was used in conjunction with the spectrometer for CO-IR. N_2 physisorption experiments were conducted using a Micromeritics ASAP 2400. SEM-EDX measurements were acquired using a Phenom Pro Desktop SEM. GC data from section 4.3 were obtained using an online Rtx-Wax fused silica gas chromatography (GC) column.

3 Results and Discussion:

3.1 CS and UiO-67 Characterisation:

This subsection will provide details relating to CS and UiO-67 characterisations.

3.1.1 ATR-IR Spectroscopy

The initial experiments carried out in this thesis involved the synthesis of UiO-67 using either AA (UiO-67 AA) or BA (UiO-67 BA) as modulators. Modulators are capable of affecting the crystal sizes of the MOF produced. The synthesis involving AA was used throughout the project since it required fewer steps and CS was solubilised in AA as well. The ATR-IR spectra of UiO-67 BA and UiO-67 AA modulator are provided in Figures 15 and 16, respectively. UiO-67 AA has a peak at 769 cm^{-1} highlighted in blue which is indicative of Zr-O-Zr stretching. This characteristic peak was used as an indicator to see whether UiO-67 AA was present when forming composites with CS.

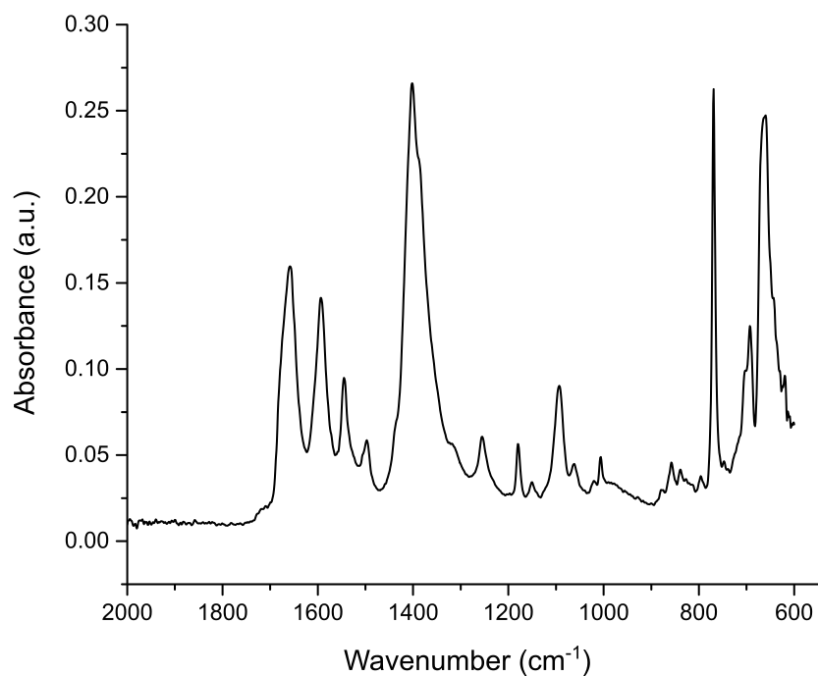


Figure 15. UiO-67 BA ATR-IR spectrum

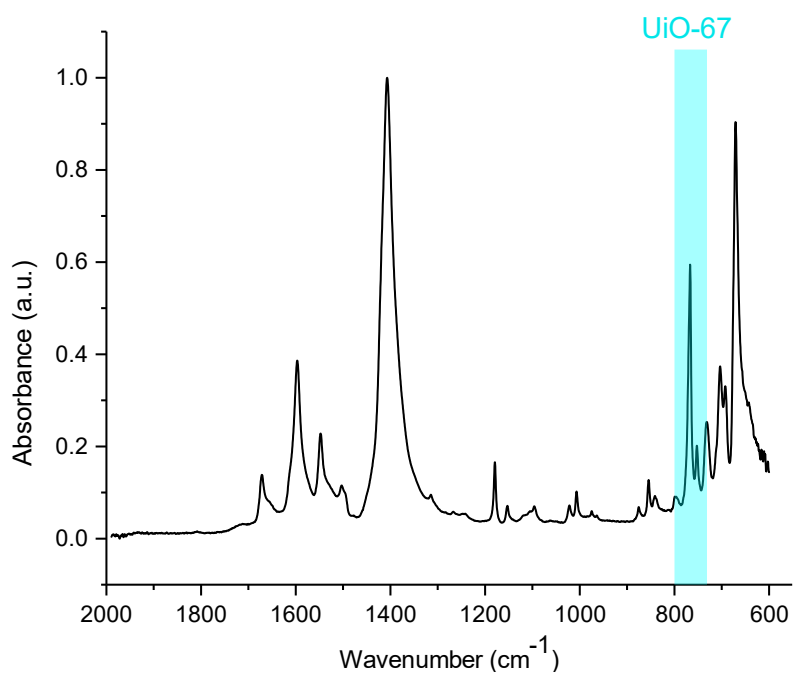


Figure 16. ATR-IR spectrum of UiO-67 AA with characteristic peak highlighted in blue at 769 cm⁻¹ indicating Zr-O-Zr stretching

The ATR-IR spectrum of pure CS powder is given in Figure 17. Like UiO-67 AA, a characteristic peak for the CS was selected as an indicator for mixing. The apex of this broad peak is 1027 cm⁻¹ and corresponds to the C-O stretching vibration of the CS³¹.

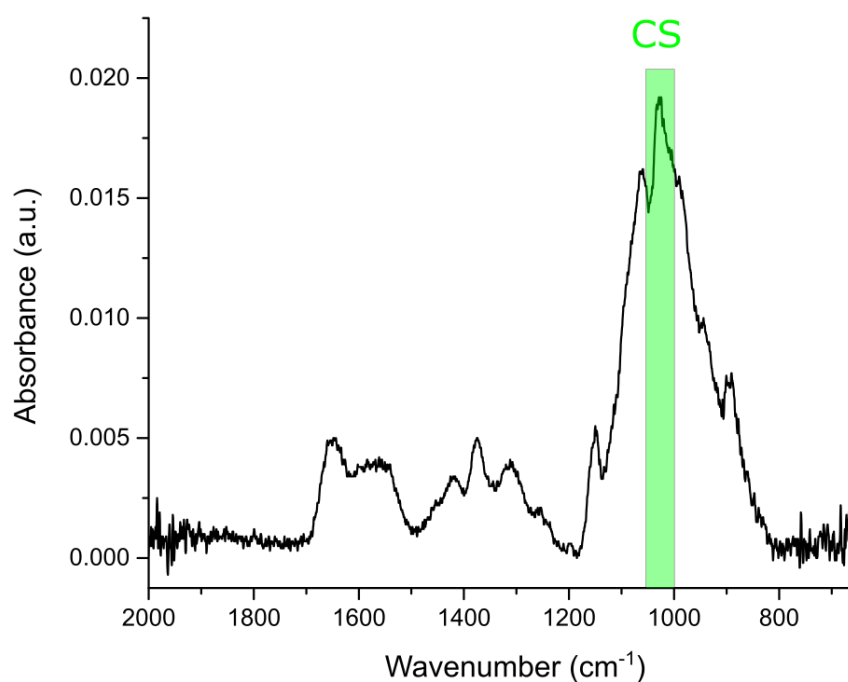


Figure 17. ATR-IR spectrum of CS powder with characteristic peak highlighted in green at 1027 cm⁻¹ indicating a C-O stretching vibration

ATR-IR spectra in Figure 18 below show characteristic peaks for CS with an apex of 1027 cm⁻¹ (green highlight, corresponding to C-O stretching) and UiO-67 AA with a wavenumber value of approximately 769 cm⁻¹ (light blue highlight, corresponding to Zr-O-Zr stretching). The intensities of these peaks differ depending on the concentration of MOF in the composite. These tests were conducted to give an indication of the CS:UiO-67 mixing.

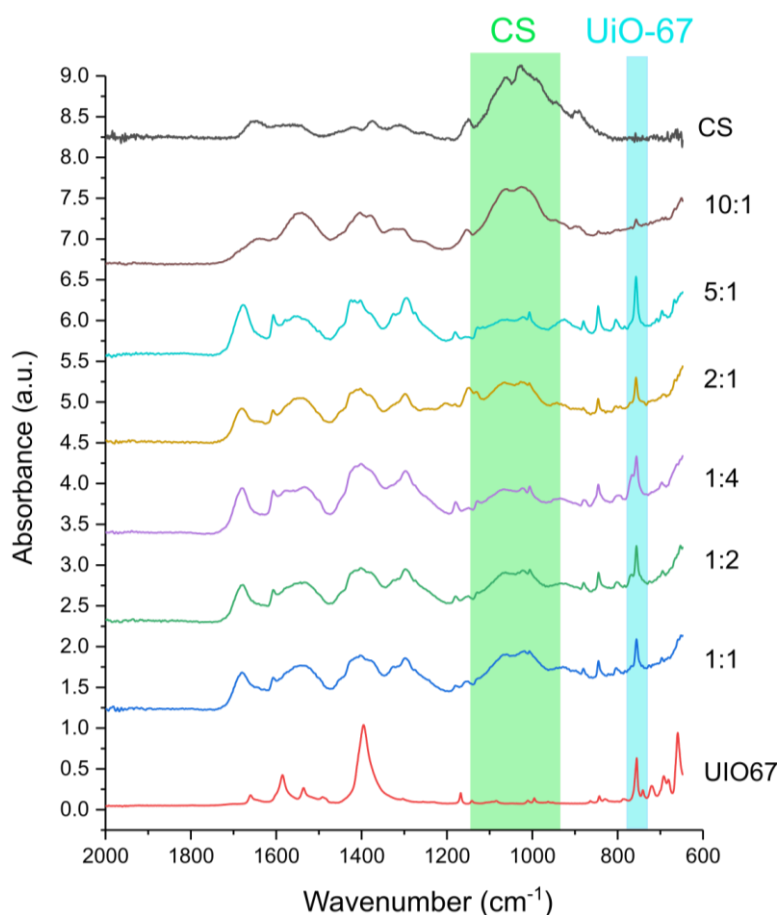


Figure 18. Stacked ATR-IR spectra of UiO-67 AA, CS, and CS:UiO-67 AA composites in different ratios. Characteristic UiO-67 (Zr-O-Zr stretching, highlighted in blue) and CS (C-O stretching, highlighted in green) peaks are depicted.

3.1.2: Scanning Electron Microscopy: CS and UiO-67

SEM images of CS and UiO-67 were used to visualise the nano-scale structure of the materials. The images depicted show CS present as a bead after drop-casting with liquid N₂ in Figure 19 and UiO-67 AA in Figure 20. The MOF was also sieved (< 38 μm) and sonicated prior to measuring. The images highlight the inherent differences in the structure of the materials. CS contains many folds and is more fibrous whereas UiO-67 AA displays its characteristic pyramid-like structure.

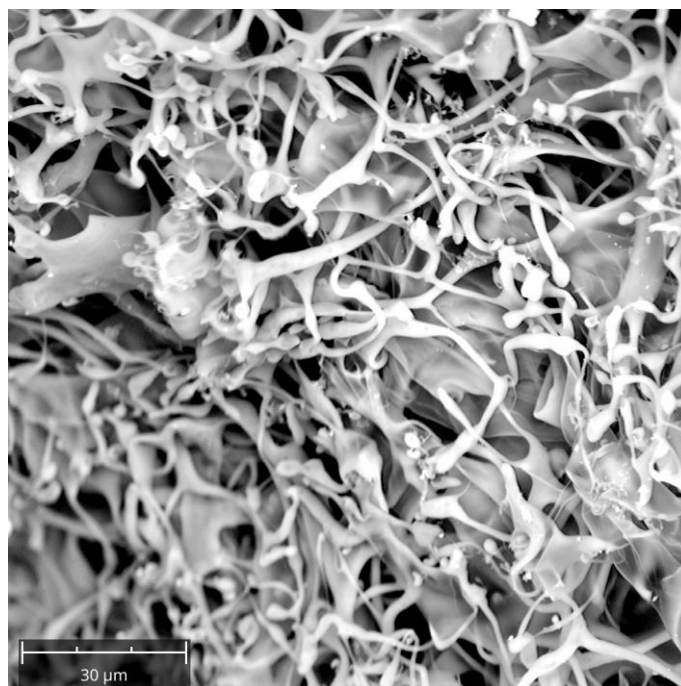


Figure 19. SEM image of CS bead drop-casted in liquid N₂. The image shows the fibrous, folded nature of the biopolymer.

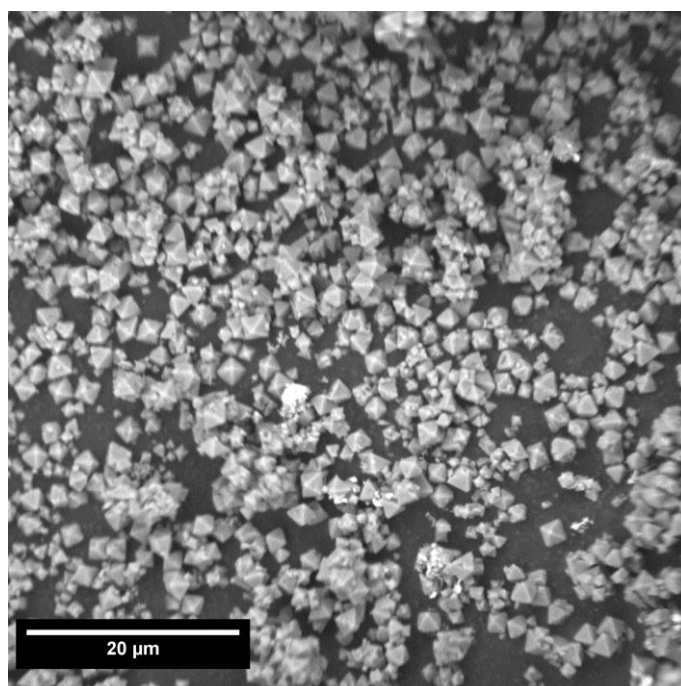


Figure 20. SEM image of UiO-67 AA showing the distinctive bipyramidal structure of the MOF. The MOF in this image was sieved at < 38 μm and sonicated prior to measuring. This was done to improve the dispersion of the MOF.

3.1.3 N₂ Physisorption

N₂ physisorption was also conducted to evaluate the porosity of the two materials. CS exhibits a type II isotherm (Figure 21) meaning it contained macropores (> 75 μm). The CS had a BET (Brunauer, Emmett and Teller) surface area of 39.63 m²/g. The surface area of CS is generally difficult to compare as the properties are affected by the source of the material and the process of manufacturing. For example, CS microspheres developed by Zhang et al.³² using an emulsion polymerisation technique exhibited a BET surface area of 35.04 m²/g. An AA

solution was also used to form these microspheres. UiO-67 AA exhibited a type I isotherm (Figure 22) meaning it was microporous (< 2 nm). The BET surface area for UiO-67 AA was substantially larger than that of the CS bead at 1,803.32 m²/g. This differed from literature values when an AA modulator was used (2400 m²/g)³⁰. The literature procedure made use of an oven and static conditions when leaving the MOF to form overnight while our procedure involved the use of a hotplate with continuous stirring at 150 RPM. These different methods of heating and mechanical action may explain the differences in BET surface area values. The N₂ isotherms highlight the inherent structural differences between the CS and UiO-67 AA.

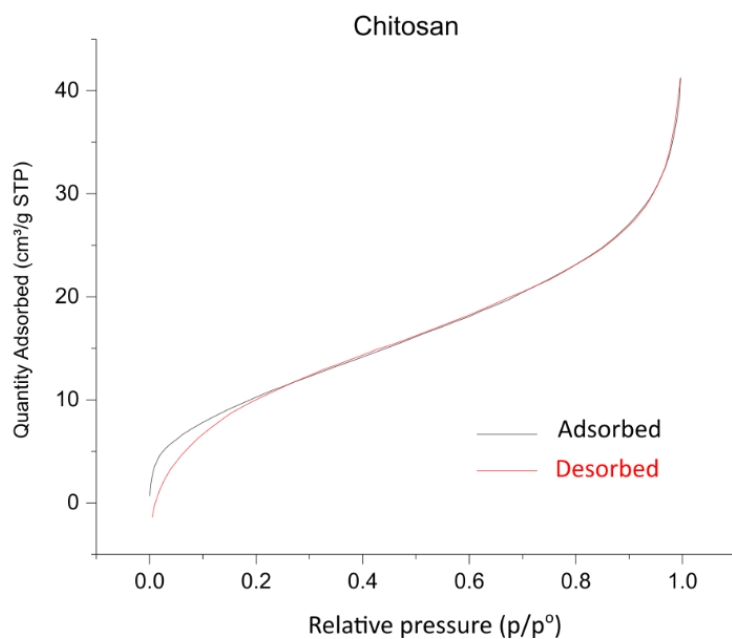


Figure 21. N₂ adsorption isotherm of CS at 77 K. The shape of the curve (Type II) indicates the presence of macropores (> 75 μm)

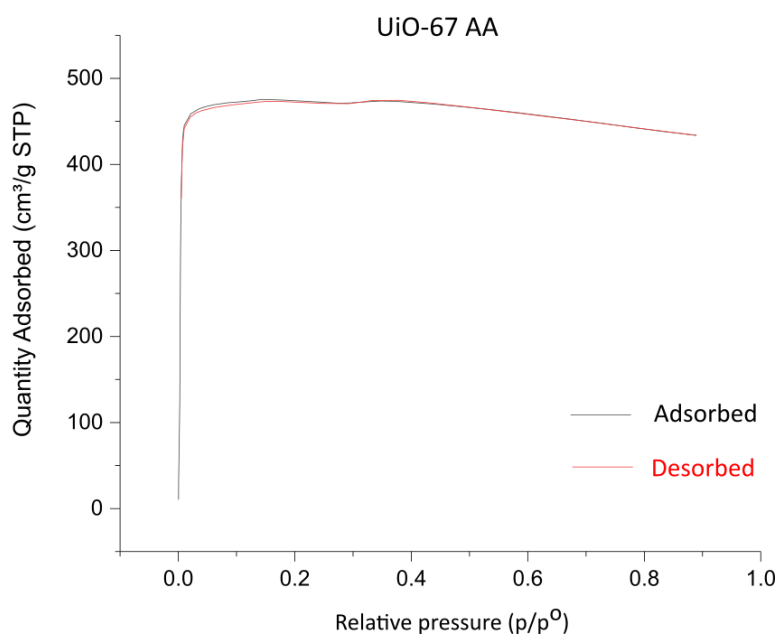


Figure 22. N₂ adsorption isotherm of UiO-67 AA at 77 K. The shape of the curve (Type I) indicates the presence of micropores (< 2 nm)

3.1.4 XRD

The XRD diffractogram of UiO-67 AA is given in Figure 23. This diffractogram highlights the crystalline nature of the MOF. Characteristic signals with 2θ values of 6.57° , 7.58° , and 13.21° are indicated.

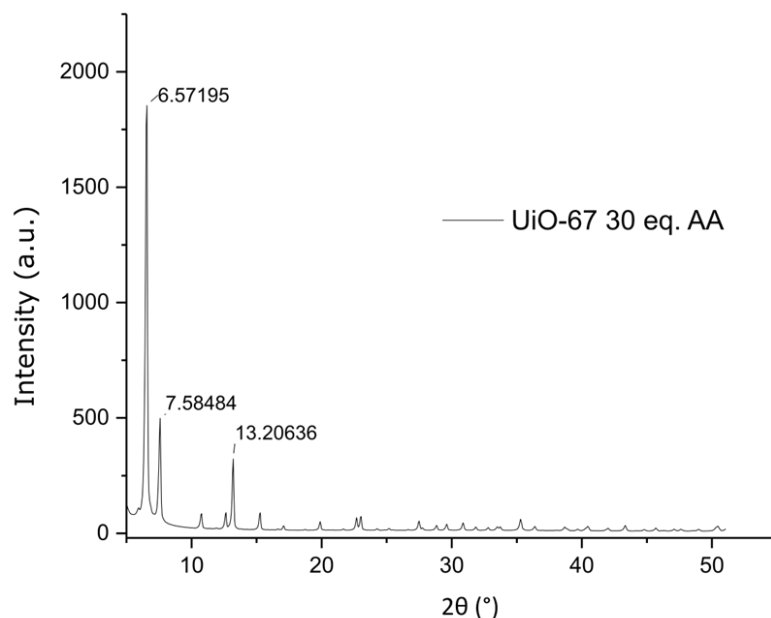


Figure 23. X-ray diffractogram of UiO-67 synthesised with 30 equivalents of an acetic acid modulator

3.1.5 CO-IR

CO-IR data shows the presence of Lewis acid (LA) sites in UiO-67. These acid sites are beneficial for catalysis as they can adsorb reactants. This was the underlying reason for choosing MeOH conversion as a test reaction. Figure 24 shows the different types of interaction that occur between the LA sites of UiO-67 and CO as well as the associated wavenumbers.

The purple highlighted section at 2152 cm^{-1} , in Figure 24, indicates the interaction between the carbon of CO and the LA site of the MOF. The orange highlighted section at 2135 cm^{-1} in the same figure is indicative of the interaction between the oxygen of CO and the LA sites of UiO-67. The interaction between the carbon of CO and the acid sites of UiO-67 occurs at a lower pressure of applied CO than the interaction between the oxygen of CO and the LA site of the MOF. The former interaction occurs at a CO pressure of 0.82 mbar while the latter occurs at 1.6 mbar. This is highlighted in Figure 25 which plots the emergence of the interactions at a given pressure of CO.

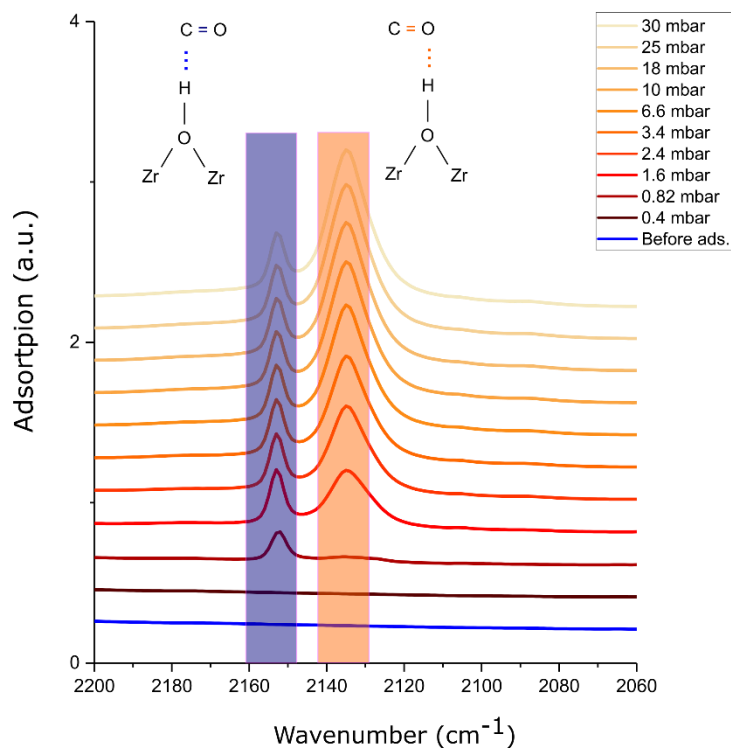


Figure 24. CO-IR analysis of UiO-67 at different pressures of CO. The purple highlighted section (2152 cm^{-1}) represents the interaction between the LA site of UiO-67 and the carbon atom of CO. The orange highlighted section (2135 cm^{-1}) represents the interaction between the oxygen atom of CO and the LA site of UiO-67 AA.

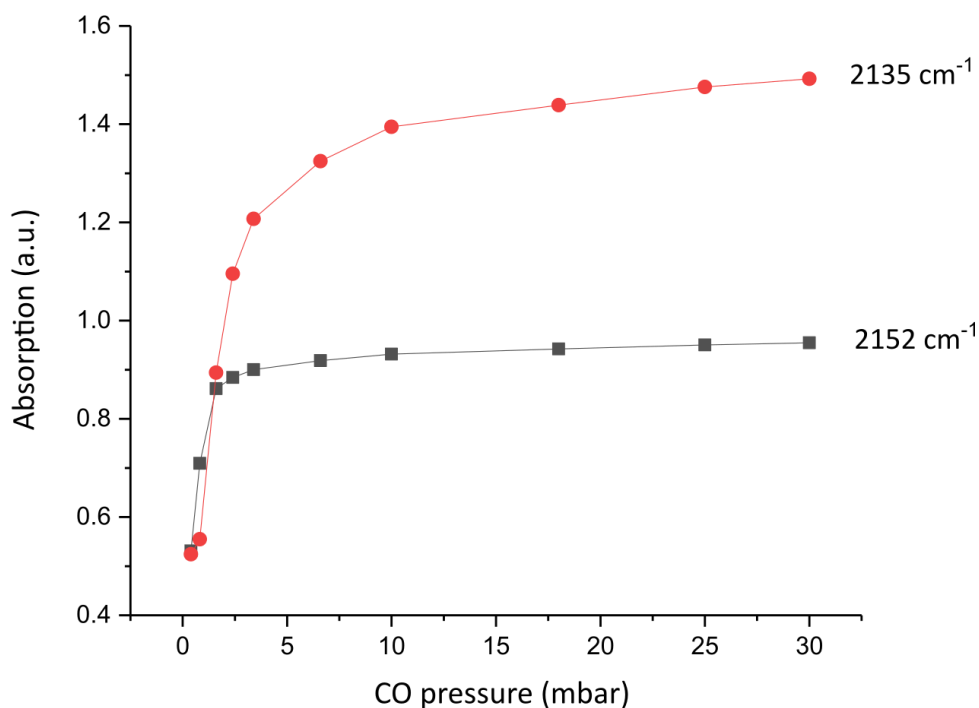


Figure 25. Absorption (a.u.) versus CO pressure applied (mbar) of UiO-67 CO-IR analysis showing emergence of characteristic UiO-67 acid site wavenumbers 2152 cm^{-1} and 2135 cm^{-1} at a given pressure. The plot shows that the interaction between the carbon of CO and the LA sites of UiO-67 at 2152 cm^{-1} (black) occurs at a lower pressure than the interaction between the oxygen of CO and the LA sites of UiO-67 AA at 2135 cm^{-1} (red).

The strength of the Brønsted acid sites present in the MOF were also analysed. Figure 26 shows the occurrence of a bathochromic shift i.e., the change in absorption to a longer wavelength (lower wavenumber) in the wavenumber range typical of hydrogen atoms. The CO before acid site adsorption has an absorption of 3674 cm^{-1} but shifts to 3610 cm^{-1} after sufficient adsorption of CO. There is also a slight increase in the wavenumber values before the bathochromic shift occurs. This indicates that the absorption is increasing in energy before the shift to the lower wavenumber. The shift occurs at 0.82 mbar pressure of CO. The interaction that is occurring involves the lone pair of CO and the OH groups of the MOF³³. The CO molecule interacts with the bridged hydroxyl group of the MOF which changes the energy of the OH vibration. This is indicated by the disappearance of the band at 3674 cm^{-1} with the concurrent rise of the band at 3610 cm^{-1} .

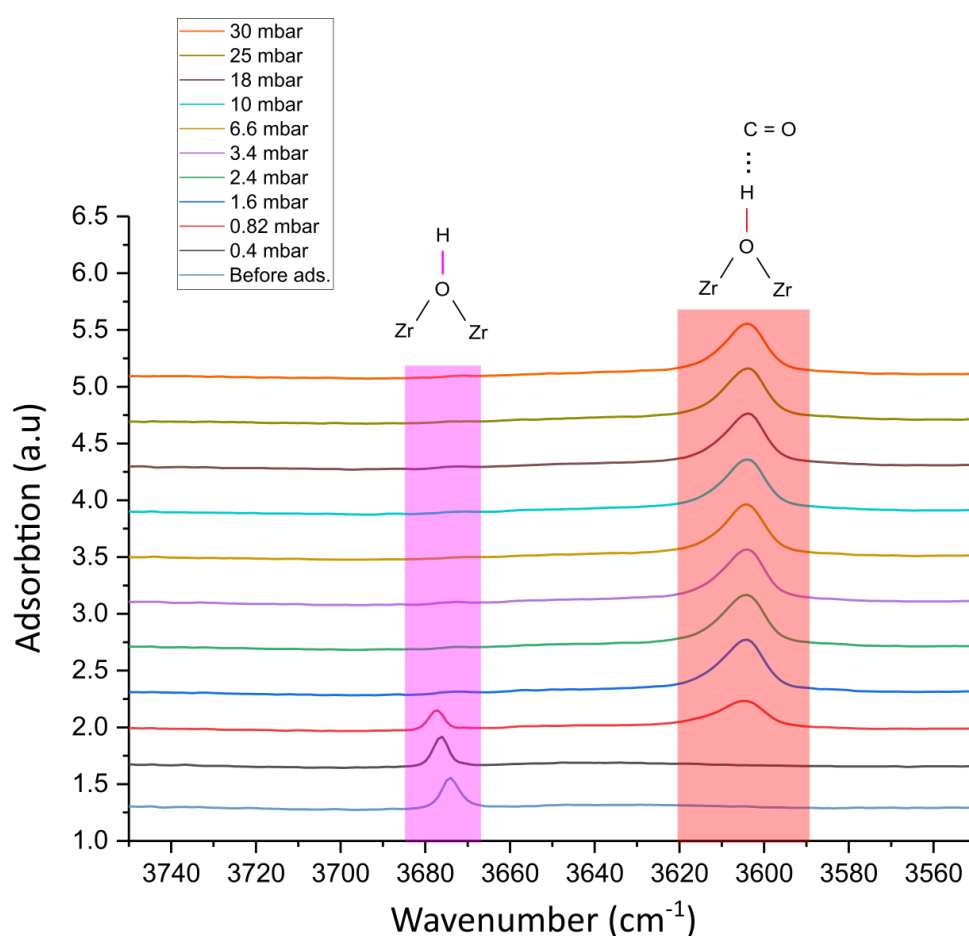


Figure 26. CO-IR spectrum of UiO-67 BA. Purple section indicates CO before acid site adsorption. Red highlight indicates CO being adsorbed to acid site via the CO carbon atom with a concurrent bathochromic shift

The extent of the shift indicates the strength of the acid site. Rivera-Torrente *et al*³³. showed that MIL-100 Al – and Cr – based analogues exhibited an -OH wavenumber shift, $\Delta\nu(\text{OH})$, of 90 and 86 cm^{-1} , respectively. This was considered to be weakly acidic. In Section 4 MeOH conversion will be used as a test reaction to evaluate these acid sites in UiO-67. The effects of mixing the MOF with CS will also be studied in terms of these acid sites. This data shows

that LA and BA sites are indeed present in UiO-67 and so can be probed with a test reaction such as MeOH conversion.

3.2 Sieving for the Effective Dispersion of MOF Crystals:

A number of sieve fractions were chosen to improve the dispersion of the UiO-67 before it was incorporated into the CS biomatrix in order to achieve a better distribution of the MOF. Figure 27 below shows the SEM images of the different sieving fractions used: $>78\ \mu\text{m}$ (A and B); $78 - 38\ \mu\text{m}$ (C and D); and $< 38\ \mu\text{m}$ (E and F). The sieving fraction above $78\ \mu\text{m}$ showed large clusters of UiO-67 with low dispersion. These clusters had diameters in the 100 micron range. Moving to the smaller $78 - 38\ \mu\text{m}$ sieve fraction showed a breakdown of these clusters and as a result higher dispersion of the MOF. These clusters exhibited diameters in the 10 micron range, i.e., image D of Figure 27 shows a cluster approximately $30\ \mu\text{m}$ in width. Finally, the $< 38\ \mu\text{m}$ sieve fraction showed well dispersed MOF crystals. Some larger clusters remained but not to the same extent as the larger sieve fractions. The largest cluster of image F was roughly $20\ \mu\text{m}$ across. The individual crystals are approximately $3\ \mu\text{m}$ in length. It is likely that catalytic substrates will interact with the acid sites of the MOF more effectively because of this increased dispersion which allows the sites to be more exposed. This method would be employed when synthesising CS:MOF composites to ensure the highest possible dispersion in the composites. The smallest sieving fraction was used to ensure maximum dispersion i.e., $< 38\ \mu\text{m}$.

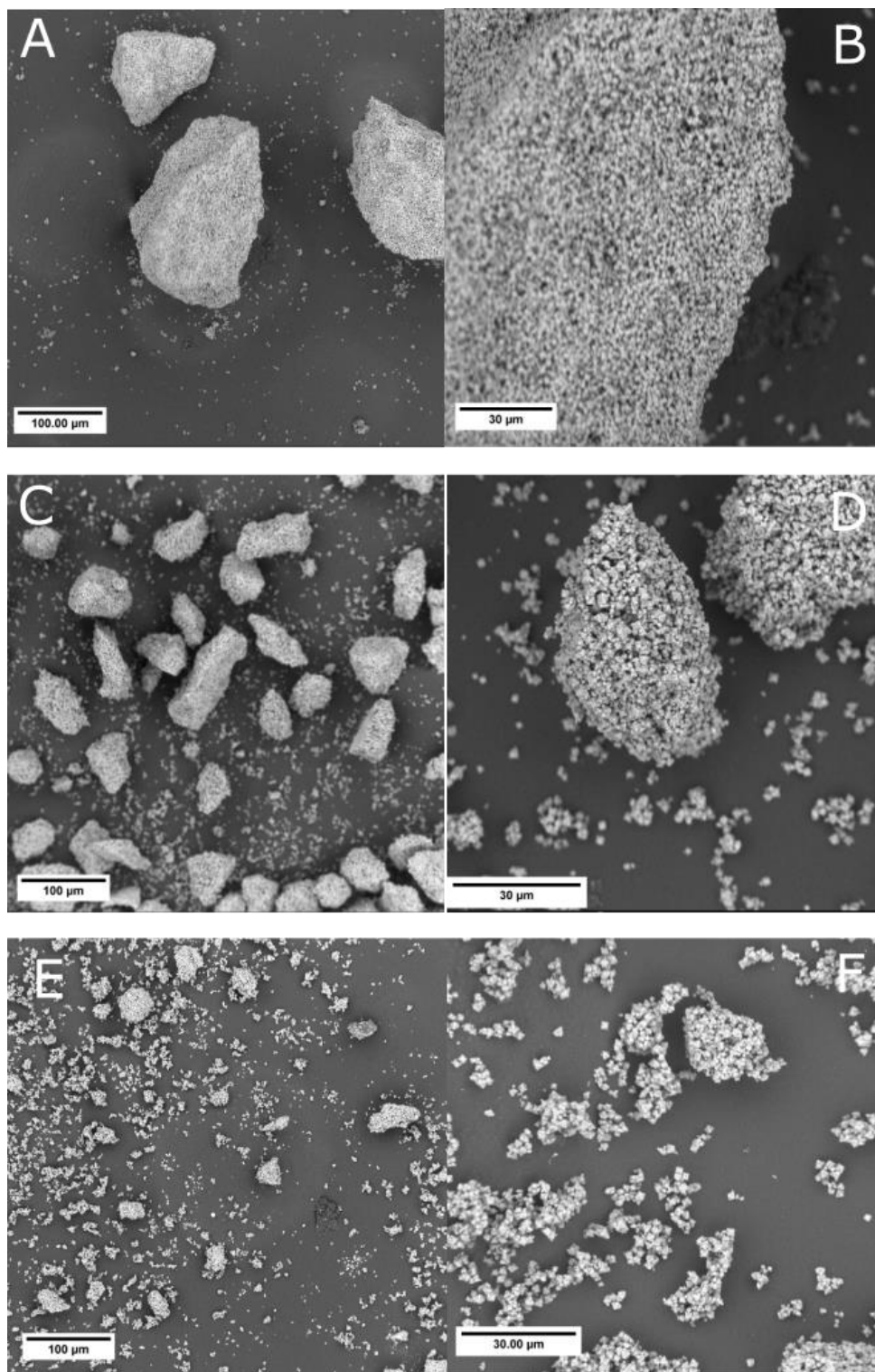


Figure 27. SEM images of sieved UiO-67 fractions > 78 μm (A and B), 38 – 78 μm (C and D), and < 38 μm (E and F)

3.3 Different Drop-Casting Techniques and their Efficacy for Producing CS:UiO-67 Beads:

A number of techniques were tested for the production of CS:UiO-67 beads. The initial methods involved experimental procedures taken from literature which made use of a 1.0 M solution of NaOH^{34,35}. A number of permutations of the parameters chosen (see experimental

section) were tested in the hopes of making stable CS and CS:UiO-67 beads. Figure 28 shows the methods graphically. These methods were ineffective however since the shapes of the beads were not maintained i.e., they formed transparent, disordered films (see Figure 29, samples 7 and 8).

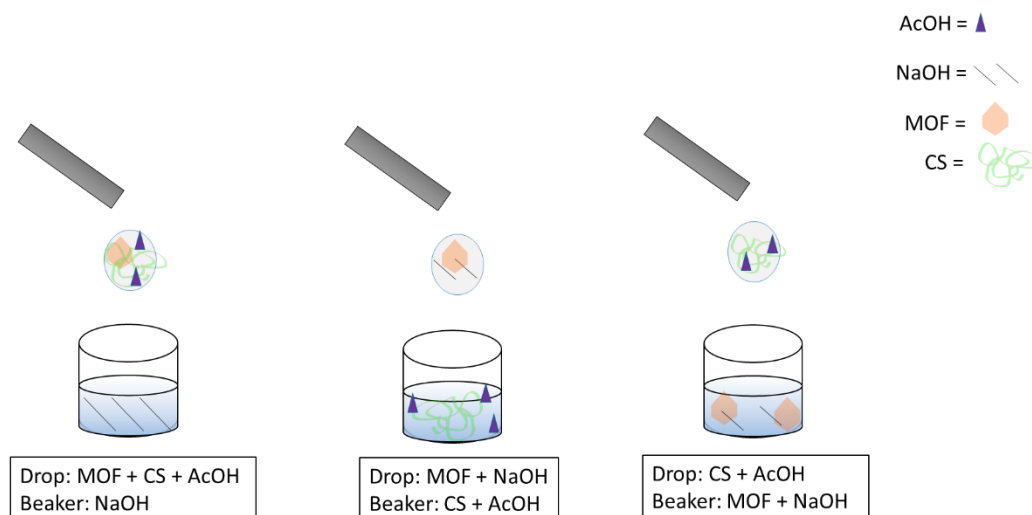


Figure 28. Initial drop-casting procedures using NaOH. The contents of the droplet and the beaker were varied to determine the best method. All methods using 1.0 M NaOH failed to produce beads with a stable shape.

Figure 29 shows the results of the various techniques employed in an attempt to synthesise beads. All samples were freeze dried after being drop-casted to remove any water that may be present. The vials labelled 1 and 2 were beads formed via direct drop-casting of a 1% CS solution directly into liquid N_2 . As depicted, the beads were stable under atmospheric conditions. Samples 3 and 4 were formed by drop-casting 2% (w/v) CS solution into a 1.0 M NaOH solution where they were left for 30 minutes. The beads were then washed three times with water and exposed to liquid N_2 . The beads shrivelled and did not maintain their shape after freeze drying. Samples 5 and 6 underwent the same procedure as samples 3 and 4 except the beads were left in a 1.0 M NaOH solution for 5 minutes. Once again malformed CS beads were produced which did not exhibit a well-defined shape. Samples 7 and 8 were synthesised using 25.0 mg of UiO-67 AA which was suspended in 5.0 mL of 1% (v/v) AA solution. This was added to 5.0 mL of a 2% (w/v) CS AA solution before being drop-cast into NaOH and subsequently washed. This procedure was ineffective as amorphous films formed instead of beads.

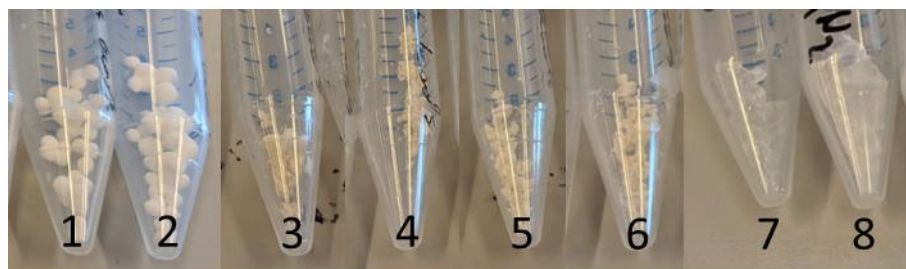


Figure 29. Beads formed via different drop-casting methods. All samples were freeze-dried after drop-casting. Samples labelled 1 and 2 were drop-cast directly into liquid N_2 and then freeze dried. All other samples were drop-cast into NaOH,

washed, subjected to liquid N₂, and then freeze dried. Samples 1 – 6 were drop-cast using only CS AA solution. Samples 7 and 8 included UiO-67 AA which was suspended in AA before being added to a 2% CS AA solution.

As can be seen in Figure 29 it is clear that drop-casting into NaOH was producing malformed beads. This may have been due to the introduction of excess water from the NaOH solution. Freeze-drying expels water present in the beads and so the higher concentration of water may have caused the beads to collapse when it was expelled. To overcome this it was decided to abandon the NaOH method and instead drop-cast the beads directly into liquid N₂ with subsequent freeze drying. This method did not form amorphous films or shrivelled beads but instead the beads maintained their shape for months after even under atmospheric conditions.

The average diameter of the drop-casted beads was then determined. The beads were drop-casted directly into liquid nitrogen with subsequent freeze drying. 32 1:3 CS:UiO-67 ratio beads, as depicted in Figure 30, were measured with the average diameter being equal to 0.277 cm. However, some clumping of the beads was observed during drop-casting. To overcome this an autoinjector may be utilised or perhaps an array of cells for each bead could be incorporated to prevent them from coming into contact with one another thus preventing clumping/agglomeration.



Figure 30. 1:3 CS:UiO-67 AA beads measured for average bead size determination. Scale is in cm

3.4 Bead Characterisations

The liquid N₂ drop-casting method produced CS:UiO-67 beads that were stable under atmospheric conditions. The concentrations of MOF present were varied to analyse its influence on the physico-chemical characteristics of the beads. The following sub-sections contain data pertaining to the different bead ratios.

3.4.1 ATR-IR Spectroscopy of Beads

In the stacked ATR-IR spectra of Figure 31 below the characteristic peaks of 1027 cm⁻¹ (green) for CS and 769 cm⁻¹ (blue) for UiO-67 AA are highlighted. The spectra for the CS:MOF bead ratios 1:4, 1:3, and 1:2 are present as well as the ATR-IR spectrum of the BPDC linker. The gold

highlighted boxes at 1680 cm^{-1} and 1297 cm^{-1} appear in the spectra of the 1:2 and 1:3 bead ratios but not the 1:4 ratio. These peaks originate from the BPDC linker which can be seen in Figure 31. This implies that free linker is present in the 1:3 and 1:2 CS:MOF bead ratios i.e. MOF was being broken down by some process involved in bead making. These golden highlighted peaks do not appear in the CS bead or the pure UiO-67 powder which means they must originate from the linker.

The characteristic MOF peak at 769 cm^{-1} (blue highlight) is also shifted in the spectra of the 1:3 and 1:2 beads. Figure 32 shows that these shifted peaks in the 1:3 and 1:2 beads have wavenumber values of approximately 757 cm^{-1} which resembles that of the linker (758 cm^{-1}). This further suggests that free linker is present in the 1:3 and 1:2 beads and was likely formed via MOF decomposition as a result of bead synthesis. As can be seen in Figure 31, the 1:4 bead spectrum has a shallow peak with an apex of approximately 769 cm^{-1} which is characteristic of UiO-67 implying that MOF was present and was not degraded by bead formation. The linker-specific peaks are also missing from the 1:4 bead spectrum which suggests that MOF was still present.

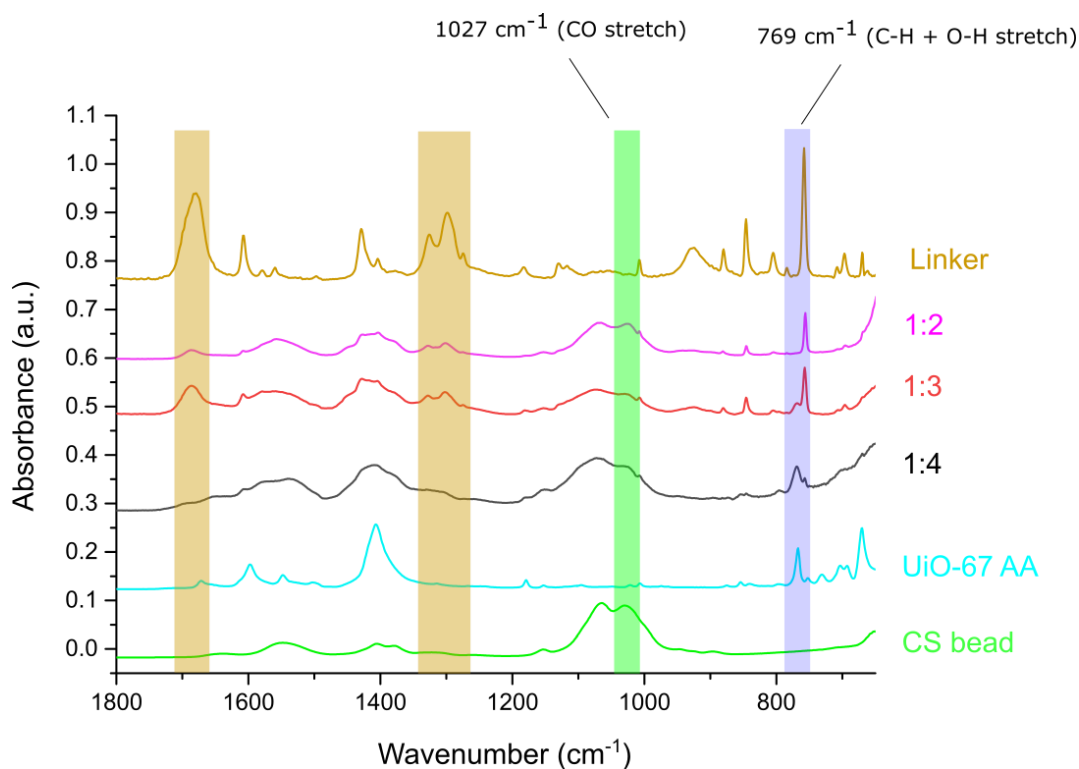


Figure 31. ATR-IR spectra of CS bead (green), UiO-67 AA (cyan), BPDC linker (gold) and CS:UiO-67 beads with ratios 1:4 (black), 1:3 (red), and 1:2 (pink) with characteristic C-O stretches of CS at 1027 cm⁻¹ (green highlighted box) and Zr-O-Zr stretching for UiO-67 AA at 769 cm⁻¹ (blue highlighted box). Peaks arising from BPDC linker are highlighted in gold boxes.

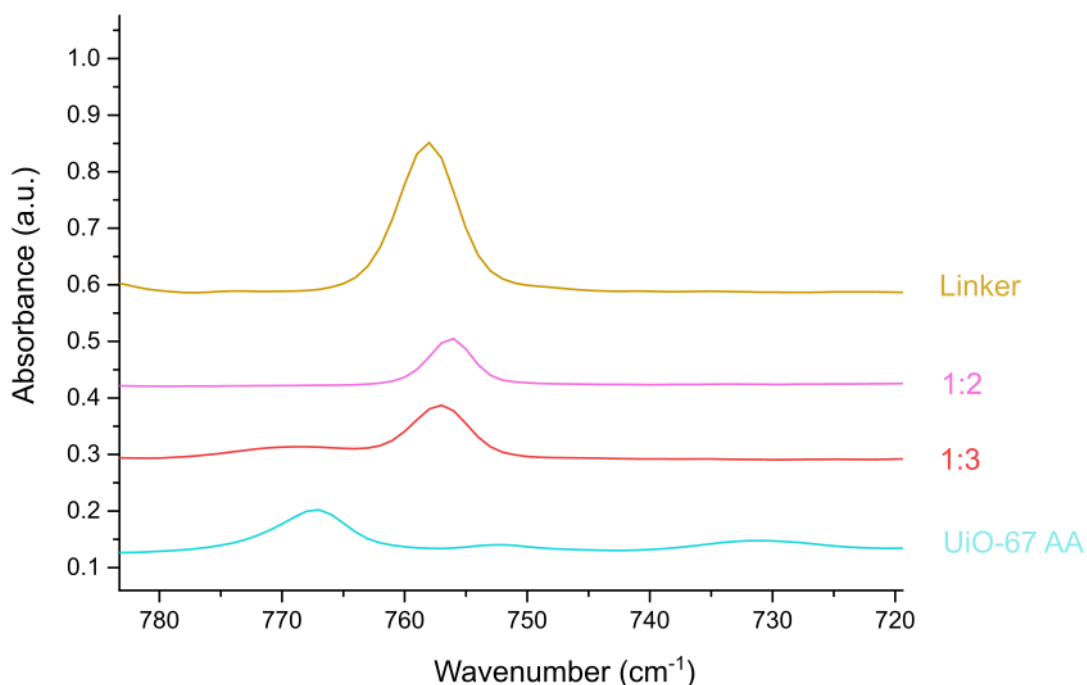


Figure 32. ATR-IR spectra of UiO-67 AA (cyan), 1:3 (red), 1:2 (pink) beads and BPDC linker (gold) showing shift in peak wavenumber values for 1:3 and 1:2 beads to 759 cm⁻¹ which more closely resembles the linker spectrum.

3.4.2 Scanning Electron Microscopy of Beads

With an established procedure for synthesising the CS:UiO-67 beads it was decided to visualise their interiors and exteriors to see how the CS and MOF interacted. Firstly, CS beads were analysed using SEM as shown in Figure 33. High resolution SEM images of a CS bead are also given in Figure 34. There appears to be unreacted CS present in the 5 μm scale image of Figure 34 as shown by the crystal-like appearance of CS in the bead.

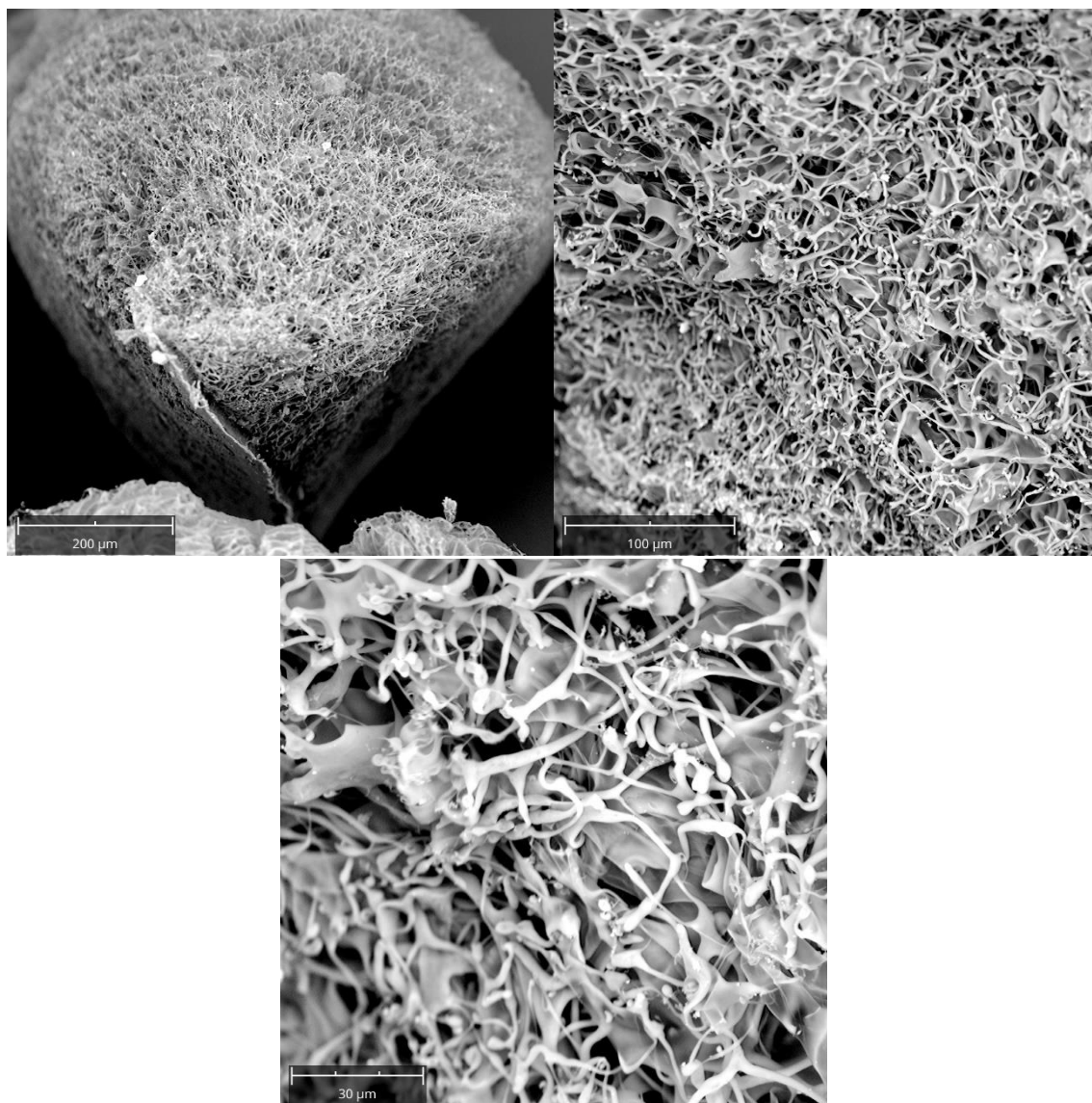


Figure 33. SEM images of pure CS beads. The images at 100 and 30 μm show the interior of the bead structure for variety

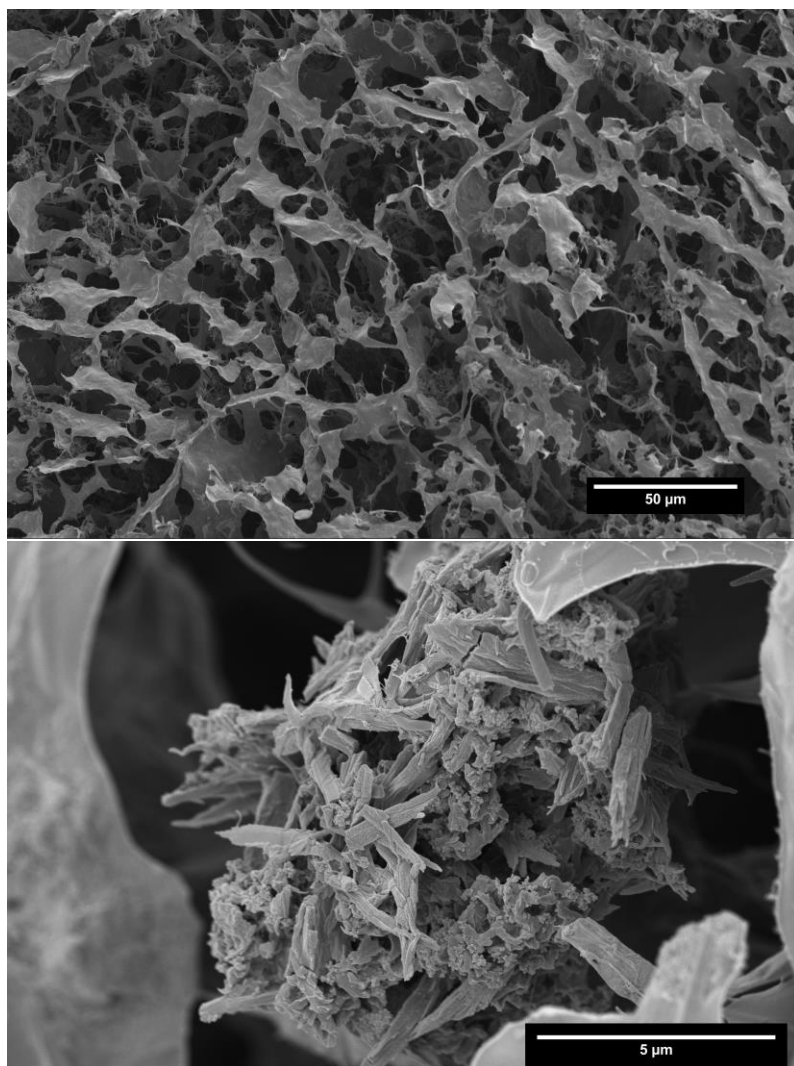


Figure 34. High resolution SEM images of CS bead showing fibrous structure and pore architecture. The 5 μm scale bar image shows unreacted CS crystals.

The bead ratios imaged were 1:2, 1:3, and 1:4. As previously discussed a $< 38 \mu\text{m}$ sieve was used to effectively disperse the MOF within the CS:UiO-67 bead. The MOF was also sonicated for 5 minutes prior to bead formation to improve its dispersion further. Images of the bead interiors and exteriors were taken to highlight the effective incorporation of the MOF (or lack thereof). Figure 35 shows both the exterior (A and B) and interior (C and D) of the 1:2 bead sample. The grey net-like material is the CS while the white specs are the MOF crystals. It is worth noting that the MOF is incorporated into the bead interior and not just the exterior.

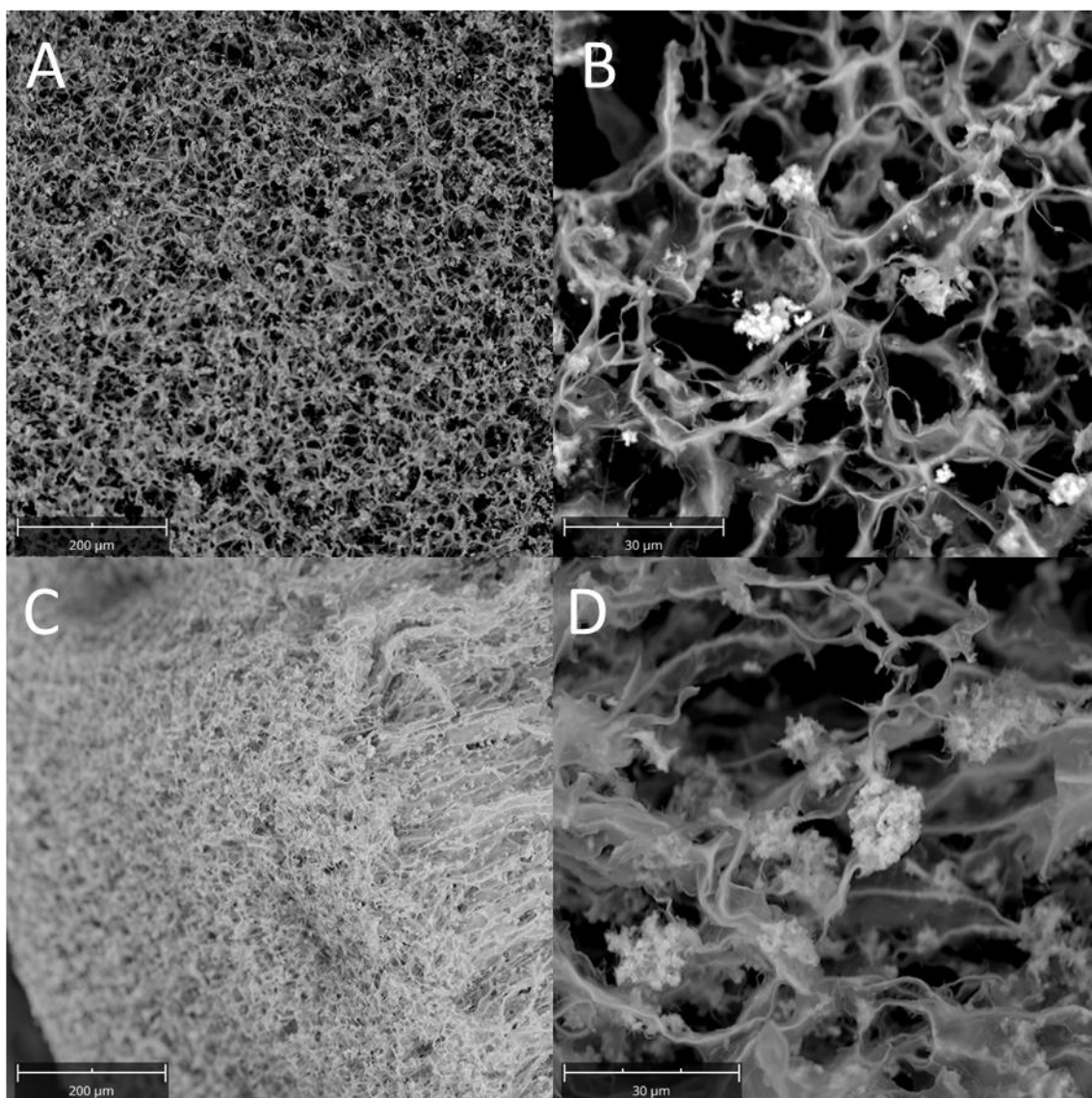


Figure 35. SEM images of 1:2 sieved and sonicated bead exterior (A and B) and interior (C and D) with scale bars of 200 and 30 μm . The grey fibrous network is the CS. The white specs are MOF clusters. The contrast in C and D is not as distinctive as A and B but MOF clusters can be visualised in D. The interior was also imaged to show that MOF incorporation was also occurring within the bead, not just on the surface.

The same can be seen for the 1:3 CS:UiO-67 beads in Figure 36 albeit with more MOF present due to the higher ratio of MOF to CS. This bead ratio shows a greater quantity of MOF compared to the 1:2 bead.

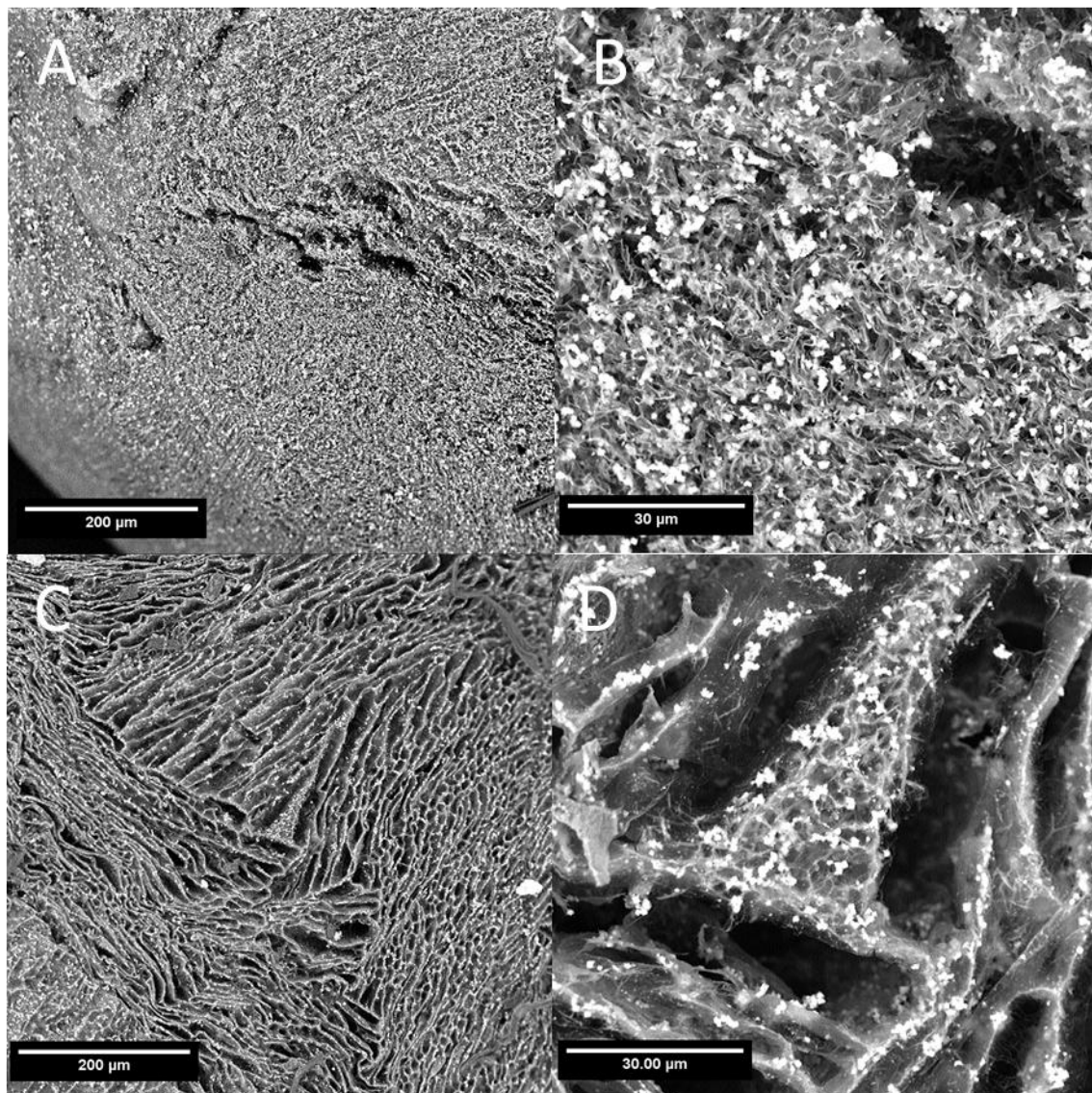


Figure 36. SEM images of 1:3 sieved and sonicated CS:UiO-67 bead exterior (A and B) and interior (C and D). The amount of MOF present is greater than that of the 1:2 sieved and sonicated bead exterior and interior due to the higher ratio of MOF to CS. This is evident from the greater abundance of white specs present in all images. . Once again MOF was shown to be incorporated within the bead and not just at the surface.

For the 1:4 ratios it was decided to observe the difference between non-sonicated/non-sieved (Figure 37) MOF and sonicated/sieved MOF (Figure 38) on its distribution within the composite beads (both the interior and exterior). As can be seen, similar to the previous case, increasing the ratio of UiO-67 to CS increases the coverage of the bead interior and exterior. Sieving and sonicating the MOF prior to bead formation appears to disperse the MOF more effectively throughout the CS matrix.

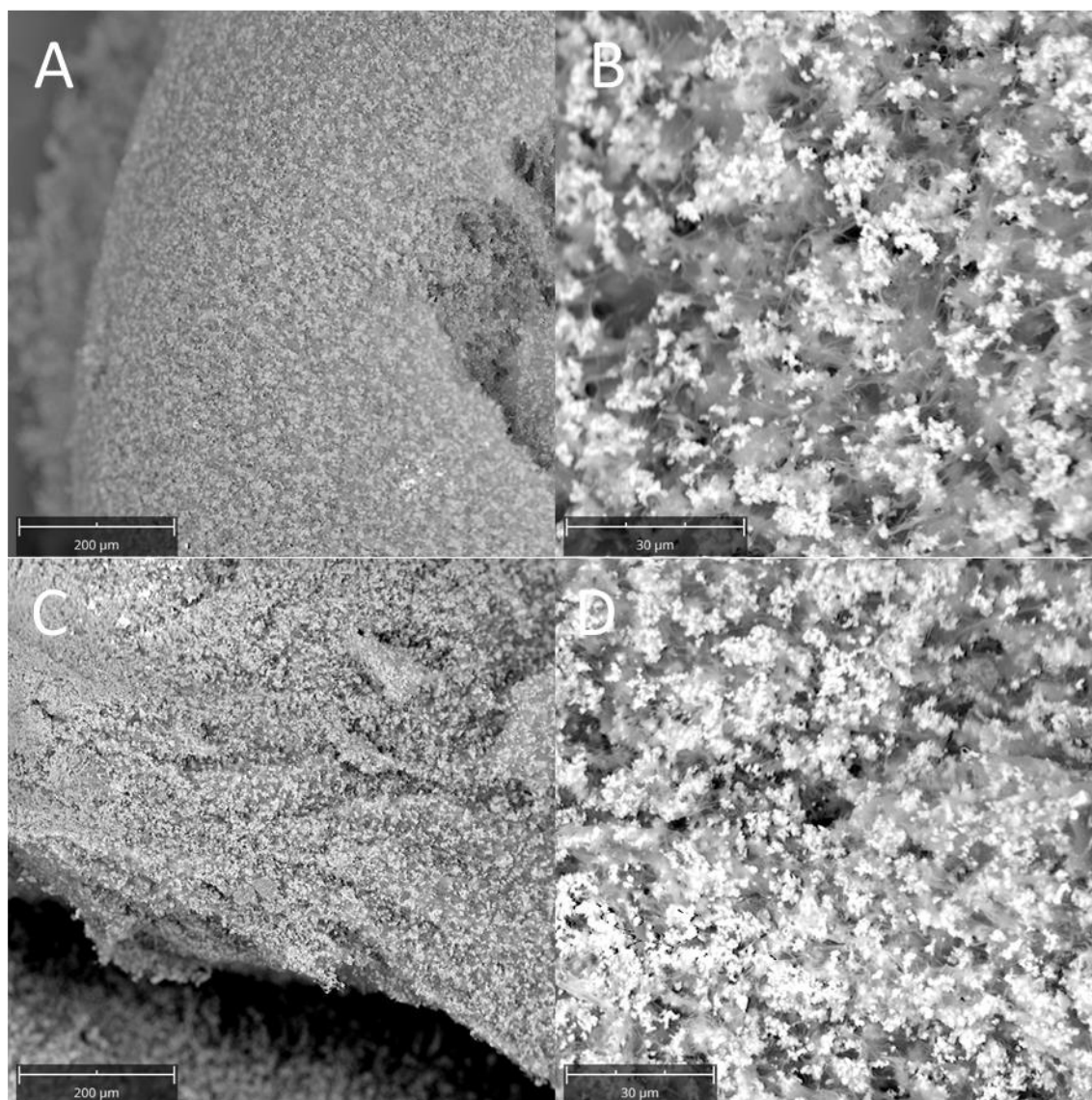


Figure 37. SEM images of 1:4 CS:UiO-67 bead non-sieved and non-sonicated exterior (A and B) and interior (C and D). These images show an even higher abundance of white specs than the 1:2 and 1:3 cases. The MOF was left un-sieved and un-sonicated to compare with the sieved and sonicated 1:4 beads (see Figure 38). It is difficult to visualise the CS matrix in these images due to the high abundance of MOF present.

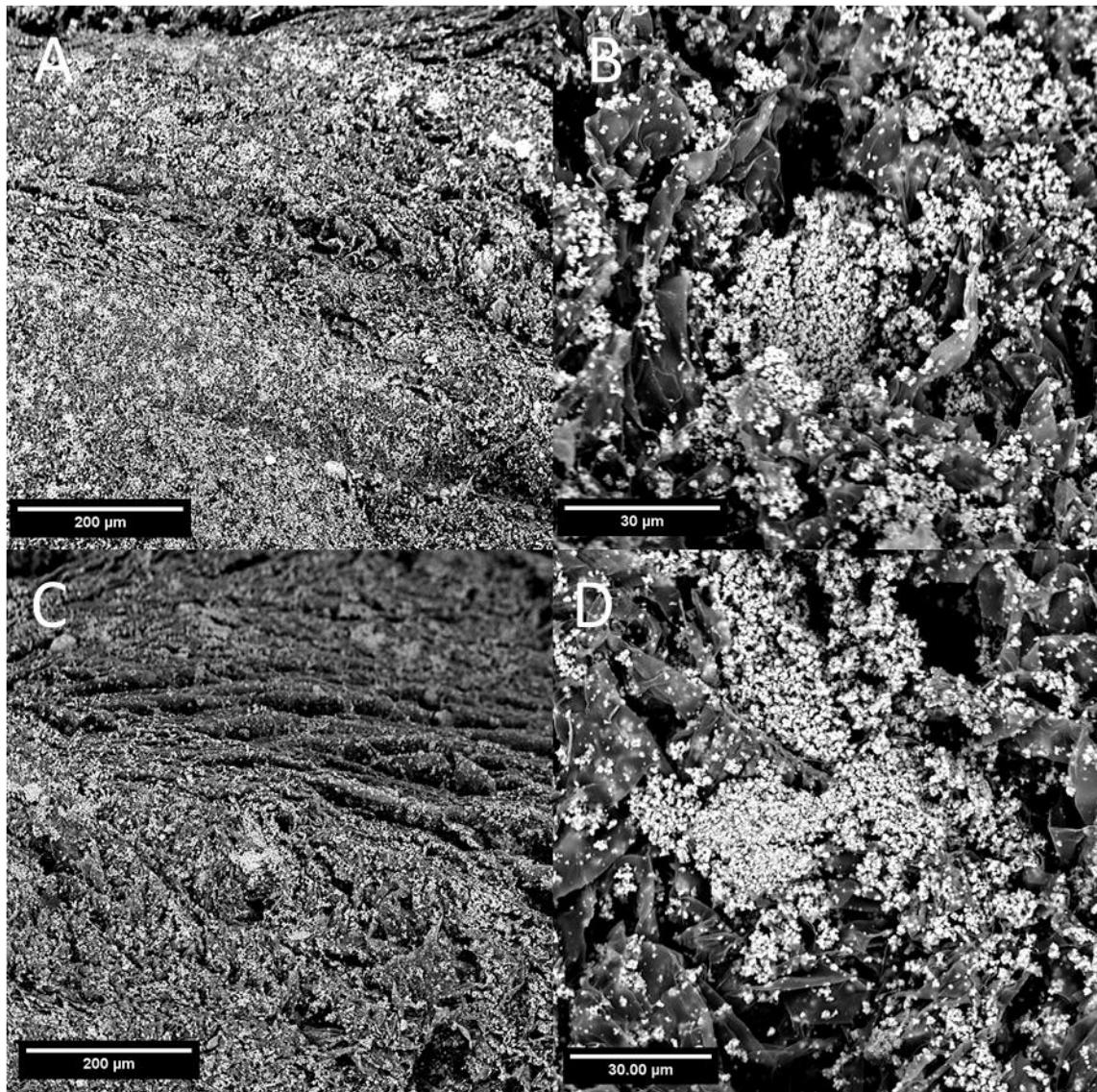


Figure 38. SEM images of 1:4 CS:UiO-67 bead with sieved and sonicated MOF. The exterior (A and B) and interior (C and D) appear to have a greater dispersion of MOF compared to the non-sieved non-sonicated case. This is evident because the CS matrix (dark grey folds) can be seen underneath the white specs more clearly than in the non-sonicated and non-sieved case (see Figure 37).

3.4.3 Scanning Electron Microscopy Energy Dispersive X-ray (SEM-EDX) Spectroscopy of Beads

SEM-EDX was carried out to obtain quantitative data relating to the CS:UiO-67 composite beads formed. To test the efficiency of the bead-forming process i.e., how much MOF was present, the EDX was set to scan for carbon, oxygen, and zirconium. The CS bead was expected to contain only oxygen and carbon from the repeating CS polymer unit as shown in Figure 3. It was anticipated that no zirconium would be present in the CS bead. A SEM-EDX map of the CS bead exterior was obtained as shown in Figure 39 (dashed line rectangle labelled 1). Figure 40 shows the SEM-EDX chemical weight concentration profile of the CS bead.

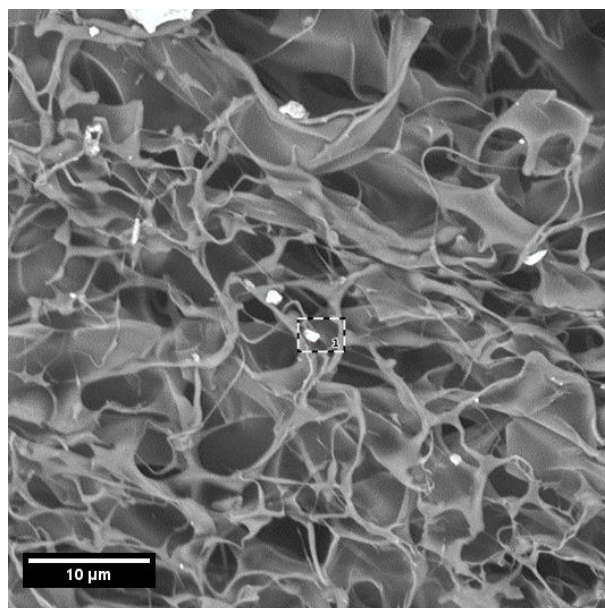


Figure 39. SEM-EDX map of CS bead exterior showing map region (dashed line rectangle).

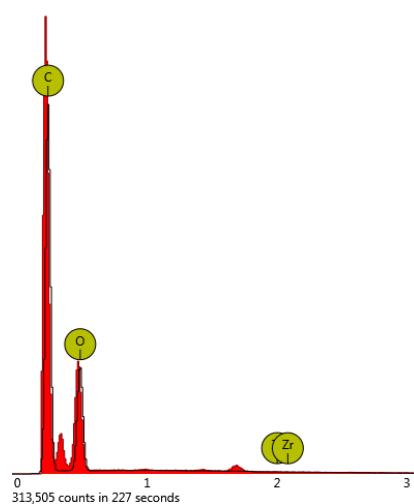


Figure 40. Chemical weight concentration profile of CS bead exterior

SEM-EDX spot analysis was carried out on the exterior of the 1:3 composite beads as shown in Figure 41. However, the appearance of the point at which analysis was conducted did not appear to have the characteristic UiO-67 crystal shape. This may be due to the degradation of the MOF crystals as a result of drop-casting using acetic acid which may have displaced an excess amount of linker leaving only zirconium metal oxide clusters i.e., the characteristic bipyramidal shape could not be formed. Figure 42 depicts the SEM-EDX chemical weight concentration profile of the 1:3 CS:UiO-67 bead exterior

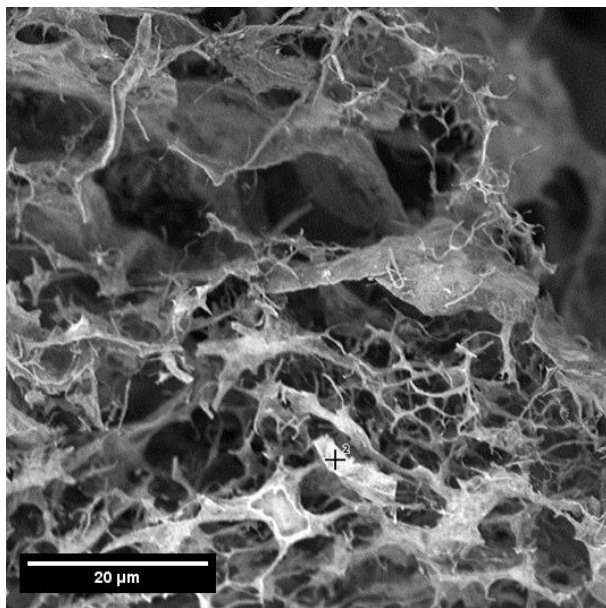


Figure 41. SEM-EDX spot analysis of 1:3 CS:UiO-67 bead exterior

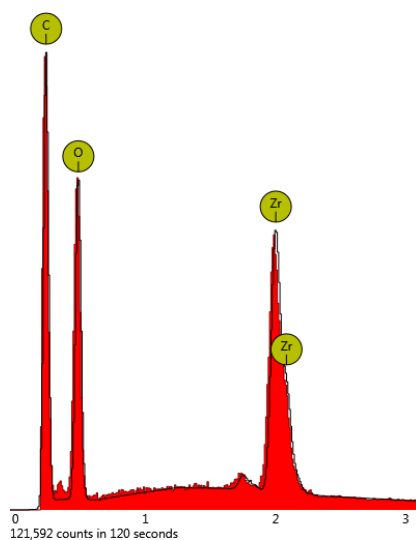


Figure 42. Chemical weight concentration profile of 1:3 CS:UiO-67 bead exterior

An EDX spot analysis of the 1:4 bead exterior was also acquired as shown in Figure 43. This time the characteristic MOF crystal structure could be observed. A point analysis was taken away from the large cluster of MOF (white clump) to ensure a reliable measurement for the

amount of CS present. The results of the chemical weight concentration profile are given in Figure 44.

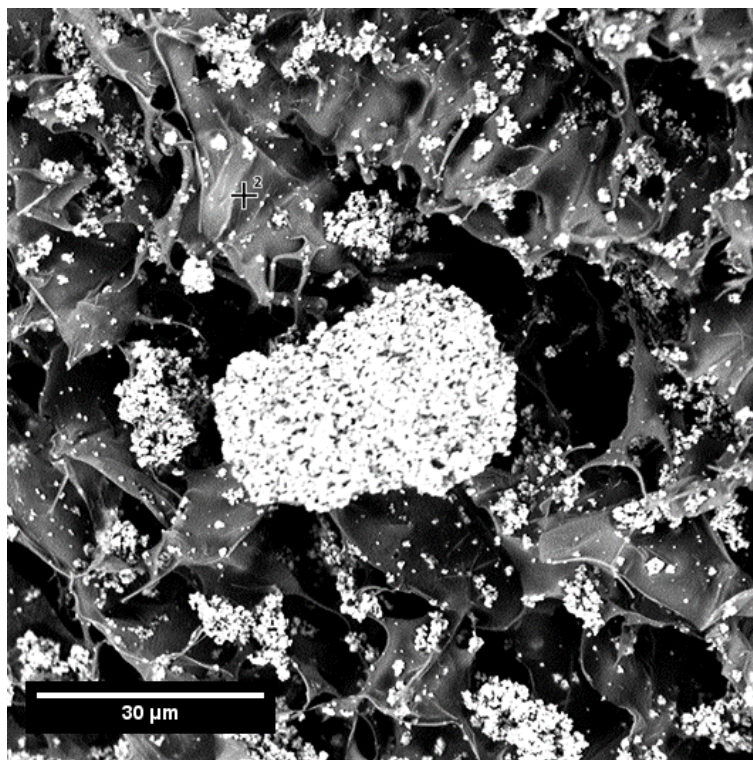


Figure 43. SEM-EDX spot analysis of 1:4 bead exterior showing spot analysis at point labelled 2.

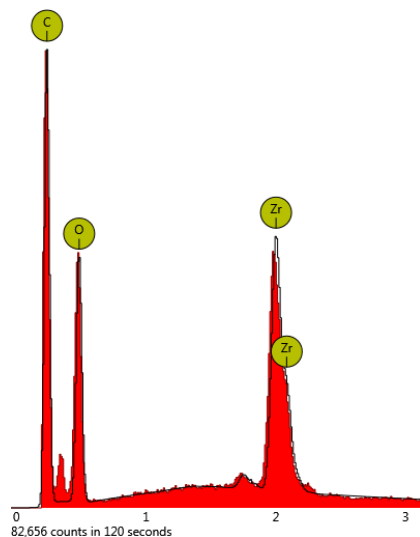


Figure 44. Chemical weight concentration profile of 1:4 bead exterior

The results obtained from the EDX map of the CS bead exterior, the spot analysis of the 1:3 and 1:4 CS:UiO-67 bead exteriors are given in Table 3. As was expected no zirconium was present in the CS bead case, however it was present in the 1:3 and 1:4 bead cases. As can be seen from Table 3 zirconium was the most abundant element in the 1:3 and 1:4 bead cases suggesting that incorporation of MOF into CS was a success. Table 3 shows that the spot analysis of the 1:4 bead had an even greater weight concentration than the 1:3 case of 64.2%. The weight concentration of zirconium was not much greater so it may be the case that the

CS started to become saturated with MOF after a certain point. However, SEM-EDX analysis was only used as an indication for MOF being mixed with CS. Further testing suggested that this may not be the case.

Table 3. Element weight concentration of carbon, oxygen, and zirconium for SEM-EDX map of CS bead exterior, spot analysis of 1:3 CS:UiO-67 bead exterior, and spot analysis of 1:4 bead exterior

Element	Weight concentration (CS bead)	Weight concentration % (1:3 bead)	Weight concentration % (1:4 bead)
Carbon	68.2	24.1	25.6
Oxygen	31.8	12.5	10.2
Zirconium	0.0	63.4	64.2

3.4.4 CS:UiO-67 Ratios for the Establishment of a Calibration Curve to Determine MOF Concentration

Figure 45 shows the stacked spectra of CS:UiO-67 AA ratios as powders with increasing amounts of MOF. The absorbance ratios of 769 cm^{-1} (MOF-specific peak, Zr-O-Zr stretching) over 1027 cm^{-1} (CS-specific peak, C-O stretching) for each sample were fitted to obtain a calibration curve. The strength of the CS-specific absorption at 1027 cm^{-1} was weak compared to that of the MOF-specific absorption at 769 cm^{-1} , however, it was strong enough to develop a calibration curve. This curve was used to determine the concentration of MOF present in the different bead ratios by evaluating their absorbance ratios.

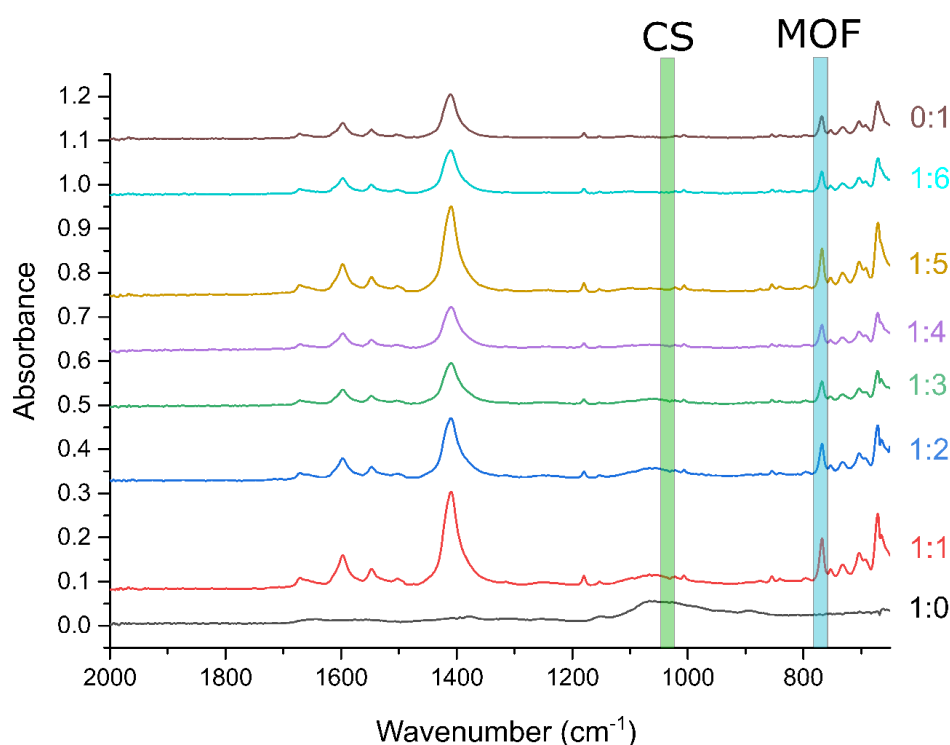


Figure 45. ATR spectra of CS:MOF powder ratios. Blue highlight indicates peak at 769 cm^{-1} which corresponds to MOF-specific Zr-O-Zr stretching. Green highlight at 1027 cm^{-1} corresponds to CS-specific C-O stretching

The absorbance ratio of a pure MOF sample (0:1 from Figure 45) had a value of 16.03 which was set to equal 100 % MOF concentration while that of pure CS (1:0 from Figure 45) had a

value of 0.42 which was set to equal 0 % MOF concentration. The absorbance ratios of the different samples (1:6 to 1:1 from Figure 45) were then plotted to develop the curve as shown in Figure 46. Equation 3 below was used to obtain the MOF percentages.

Equation 3. MOF % equation from absorbance values

$$\left[\frac{A(769 \text{ cm}^{-1})}{A(1027 \text{ cm}^{-1})} \right] * 100 = \text{MOF \%}$$

$A(769 \text{ cm}^{-1})$ and $A(1027 \text{ cm}^{-1})$ are the absorbance values at 769 cm^{-1} and 1027 cm^{-1} for each spectrum, respectively. MOF % is the percentage of MOF present.

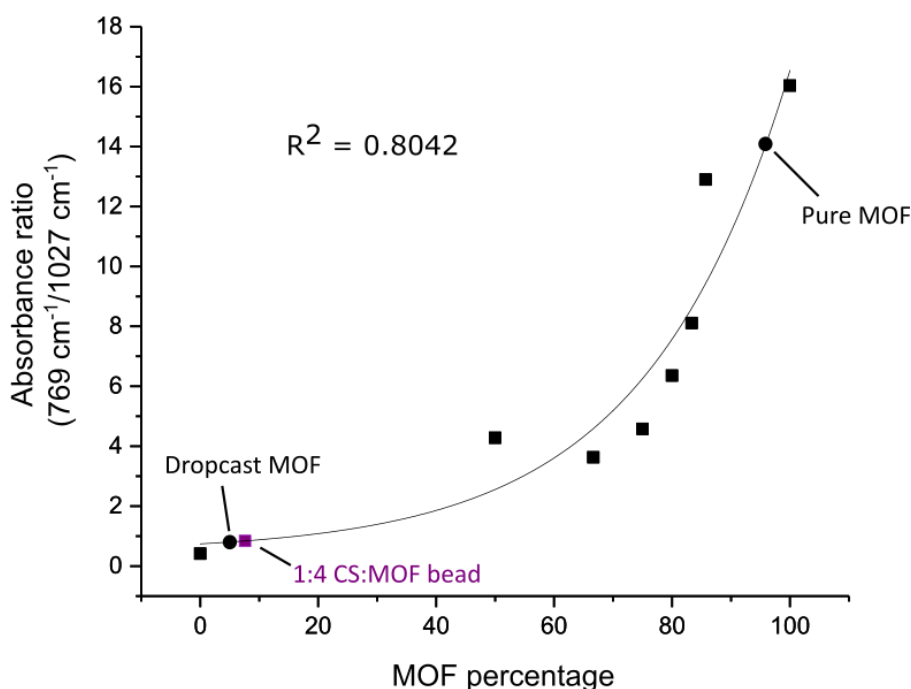


Figure 46. Fitted plot of $769 \text{ cm}^{-1}/1027 \text{ cm}^{-1}$ absorbance ratio versus MOF percentage. The MOF percentage values of pure MOF, Dropcast MOF, and a 1:4 CS:MOF bead were fitted to the curve.

The absorption ratio of $769 \text{ cm}^{-1}/1027 \text{ cm}^{-1}$ from a different MOF batch was found to be 14.08 which corresponded to a MOF percentage of 95.9%. The absorption ratio of a 1:4 CS:MOF bead was also plotted to determine the concentration of MOF present. As a 1:4 bead, the MOF percentage was expected to have a value somewhere near 80%. From the curve in Figure 46 it can be seen that this number was much lower with a MOF percentage of 7.61%. As was discussed previously this is most likely due to MOF decomposition as a result of drop-casting with AA.

To study this further, a pure MOF bead was drop-casted using AA i.e., one containing no CS. This sample was labelled Dropcast MOF. The drop-casted beads were formed in the same way as those containing CS. After freeze-drying, the drop-casted MOF beads lost their shape when exposed to the atmosphere. This was to be expected since no CS was present to maintain the bead structure. ATR-IR of the drop-casted MOF was then taken. The absorbance ratio of $769 \text{ cm}^{-1}/1027 \text{ cm}^{-1}$ yielded a value of 0.80 which corresponded to a MOF percentage of 5.01%

i.e., a decrease in MOF percent of approximately 90% compared to the pure non-drop-casted MOF. From this it was concluded that drop-casting was degrading the MOF.

Table 4 shows the sample ID's, absorbance ratios, and corresponding MOF percentage values. The data had to be fitted to a polynomial curve as the 1:2 powder ratio had a lower than expected absorbance ratio of 3.63

Table 4. Calibration curve data showing powder ratios 0:1 - 1:0, Dropcast MOF (pure MOF dropcasted with AA), 1:4 Bead, and Pure MOF from a different batch. The corresponding MOF percentages are given according to the absorbance ratio of the sample

Sample ID	Absorbance Ratio (769 cm ⁻¹ /1027 cm ⁻¹)	MOF Percentage (%)
0:1	0.42	0
Dropcast MOF	0.80	5.01
1:4 Bead	0.84	7.61
1:1	4.28	50
1:2	3.63	66.66
1:3	4.58	75
1:4	6.36	80
1:5	8.11	83.33
1:6	12.90	85.7
Pure MOF	14.08	95.9
1:0	16.03	100

3.4.5 Stability Tests of UiO-67 as a Bead

To better understand the effects of drop-casting on the MOF content of the composite beads pure MOF beads (those without CS) were analysed. Figure 47 shows the stacked ATR-IR spectra of UiO-67 before drop-casting (red, labelled "pre-bead"), after drop-casting with AA (black, labelled "post-bead"), UiO-67 subjected to AA as a stability test without drop-casting (green, labelled "stability"), and the linker BPDC (blue). The orange highlighted peaks that emerge in the red, green, and blue spectra indicate that AA was affecting the structure of the MOF leading to its degradation since these peaks are absent from the UiO-67 sample which was not subjected to AA.

The peaks at 1700 cm⁻¹, 1300 cm⁻¹, and 825 cm⁻¹ suggest that the MOF had been decomposed leaving excess linker since these peaks also appear in the linker spectrum. The characteristic MOF peak at 769 cm⁻¹ is absent in both the post-bead and stability test spectra and a new peak has emerged at 759 cm⁻¹ which is also present in the spectrum of the linker (blue). This further implies that the MOF is being broken down to linker. The peaks that emerge in the blue, green, and black spectra around 1700 cm⁻¹ are characteristic C=O stretches of BPDC which indicates the presence of linker carboxyl groups which are no longer bonded to the zirconium metal clusters.

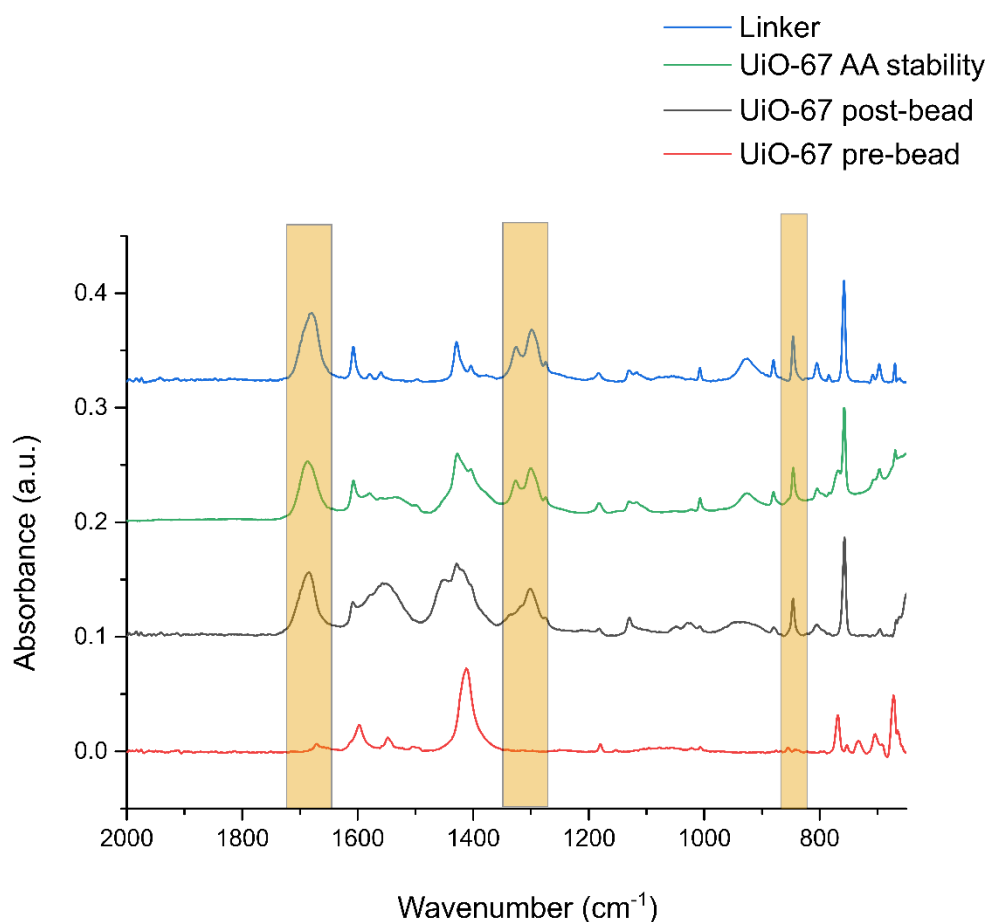


Figure 47. Stacked ATR-IR spectra showing the emergence of peaks (orange highlights) at 1700 cm^{-1} , 1300 cm^{-1} , and 825 cm^{-1} as a result of drop-casting with AA and the effects of an AA stability test on the MOF structure. The emergence of these peaks suggest that the MOF structure is being broken down by AA leaving only linker.

TGA data was obtained to corroborate this. In the TGA thermogram of Figure 48 we see that the initial thermal event of Wt% loss occurs at a decreased temperature after the MOF has been drop-casted with AA (post bead, red curve). However, there is a shallow decline in the TGA curve of the post-bead MOF at approximately $550 \text{ }^\circ\text{C}$. This suggests, that a small amount of undisturbed MOF may still be present.

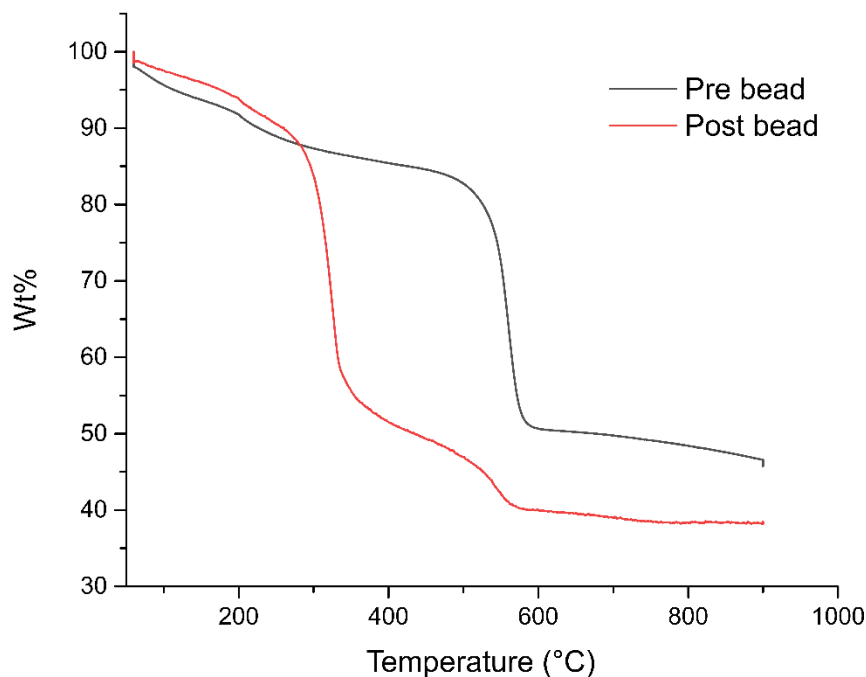


Figure 48. TGA thermogram of UiO-67 before drop-casting with AA (pre-bead, black) and after drop-casting (post-bead, red). The lower temperature inflection point of the post-bead curve suggests that free BPDC linker is being decomposed rather than linker which is connected to zirconium oxide nodes in the MOF.

Figure 49 shows the first derivatives of the TGA curves for the pre- and post-bead MOF samples (black and red, respectively). The apex of the peak in the post-bead UiO-67 (i.e., after drop-casting) is at approximately 325 °C which corresponds to the melting point of free BPDC³⁶, whereas for pre-bead UiO-67 the main inflection point occurs at approximately 561 °C which more closely resembles the volatilization of BPDC linkers in UiO-67⁹ when they are coordinated to a zirconium cluster. There is a shallow minimum at approximately 542 °C in the post-bead TGA derivative which suggests that some MOF may still be present. The differences between the two derivatives implies that the MOF structure has been broken down by dropcasting with AA leaving free linker which undergoes thermal degradation at 325 °C but there may still be some MOF remaining.

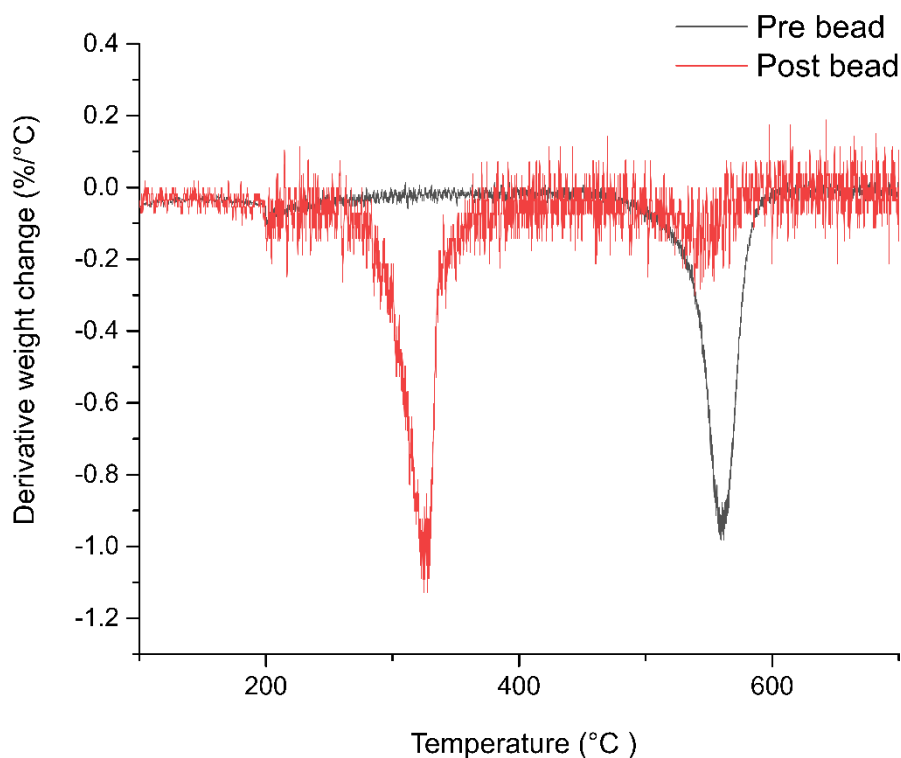


Figure 49. First derivatives of TGA curves for pre- (black) and post-bead (red) UiO-67. The peak for the post-bead curve at 325 °C suggests that the linker is not connected to any zirconium oxide nodes. The shallow peak at approximately 542 °C in the post-bead case suggests that some undisturbed MOF still remains. The pre-bead MOF shows a peak at 550 °C which indicates the presence of UiO-67

This two-step decomposition for the post-bead MOF may be explained by the presence of “guest” AA molecules which are hosted by the pores of the MOF. Schaate *et al*³⁰ reported that so-called “guest-removal” of AA modulator occurs up to 300 °C which is also observed here. The thermal decomposition then occurs at temperatures above 400 °C which can also be seen in the TGA data obtained. However, the Wt% loss seen in the TGA data presented by Schaate is not as severe as the data shown here. In Schaate’s case there is a Wt% loss of 11.3%. In our case there is a decrease of roughly 45%. This greater weight loss implies that it was not guest molecules being removed (although there might have been some) but rather the MOF structure had been disturbed by the effects of AA drop-casting leaving free linker which was decomposed at its melting point at approximately 325 °C

The post-bead TGA profile may be a result of BPDC linker displacement from the Zr_6O_8 clusters of the MOF. Figure 50 demonstrates how acetate ligands from the AA modulator may displace the linker to yield extra-framework linker which hangs “loose”. This phenomenon is not uncommon when using AA as a modulator and can in fact be beneficial for catalysis since it can lead to increased numbers of acid sites which is preferential for catalysis³⁷. However, using AA for the drop-casting of CS:MOF beads may have a detrimental effect on the MOF structure i.e., an over-displacement of linker which causes the breakdown of the MOF structure. This would explain why the TGA profile of the post-bead sample more closely resembles BPDC.

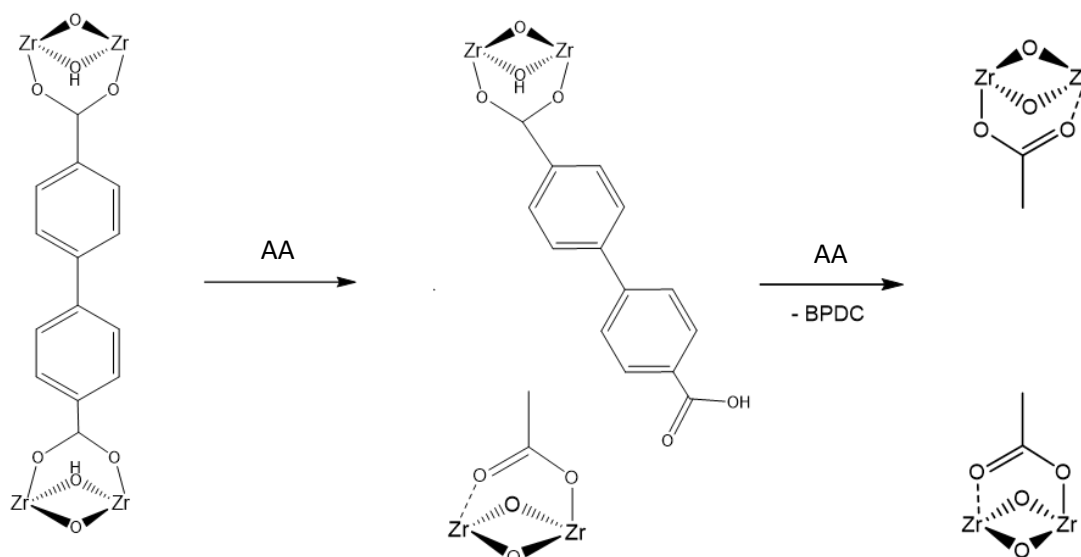


Figure 50. Displacement of BPDC linker from defect-free UiO-67 via AA

3.4.6 TGA of beads:

Thermogravimetric analysis (TGA) was used to analyse the thermal properties of the CS:UiO-67 AA beads e.g. temperature of moisture loss. Figure 51 shows the different TGA curves of pure UiO-67 AA, as well as 1:4 and 1:2 beads which were sieved and sonicated, pure CS powder, and a CS bead.

The CS bead and pure CS powder have an initial weight loss event in the temperature range from 100 – 200 °C with an associated Wt% loss of 15% for the bead and 10% for the powder. This is likely due to the loss of residual water from the CS matrix. The greater weight loss from the bead implies that there is more water present in the bead which would make sense since an aqueous AA solution is used for dropcasting. The main inflection point of the CS bead corresponds to a further Wt% loss of 65% leaving a final Wt% of approximately 20%. This is most likely due to the carbonization of the CS³⁸. The CS powder experiences its main weight loss stage at a higher temperature compared to the CS bead which brings with it a 60 Wt% loss leaving 30 Wt% by the end of the run. The higher Wt% loss in the bead compared to the pure CS powder may be due to the drop-casting conditions i.e., the use of AA and liquid N₂ may damage the CS structure when it is being formed as a bead making it less stable to TGA measurements.

UiO-67 AA exhibits minor fluctuations from 100 – 500 °C which is again likely due to the loss of residual moisture. The main inflection point at 545 °C indicates linker volatilization⁹. The curve for the MOF plateaus after this with a remaining 45 Wt%.

The 1:4 and 1:2 bead ratios show curves which exhibit a number of decomposition stages after the initial moisture loss from 100 – 200 °C. Following this loss of moisture the first event occurs at approximately 300 °C. This is most likely the carbonization of the CS as was seen in the CS bead at 290 °C. This carbonization event takes place at a higher temperature than in the CS bead curve which is likely due to the presence of the MOF in the 1:2 and 1:4 beads. The MOF may improve the thermal stability of the CS since the carbonization event takes

place at a higher temperature compared to the CS bead. The second event occurs at approximately 500 °C which is most likely the volatilization of the MOF linker, as was the case with the pure MOF at 545 °C. It is also interesting to note that there is lower weight loss percentage in the 1:4 bead compared to the 1:2 bead i.e., by the end of the analysis the 1:2 bead had a final Wt% of 35 % while the 1:4 bead had a final Wt% closer to the pure MOF at 50 %. This is due to the higher ratio of MOF present in the 1:4 case. This implies that adding more MOF reduces the weight loss percentage of the bead during TGA measurements.

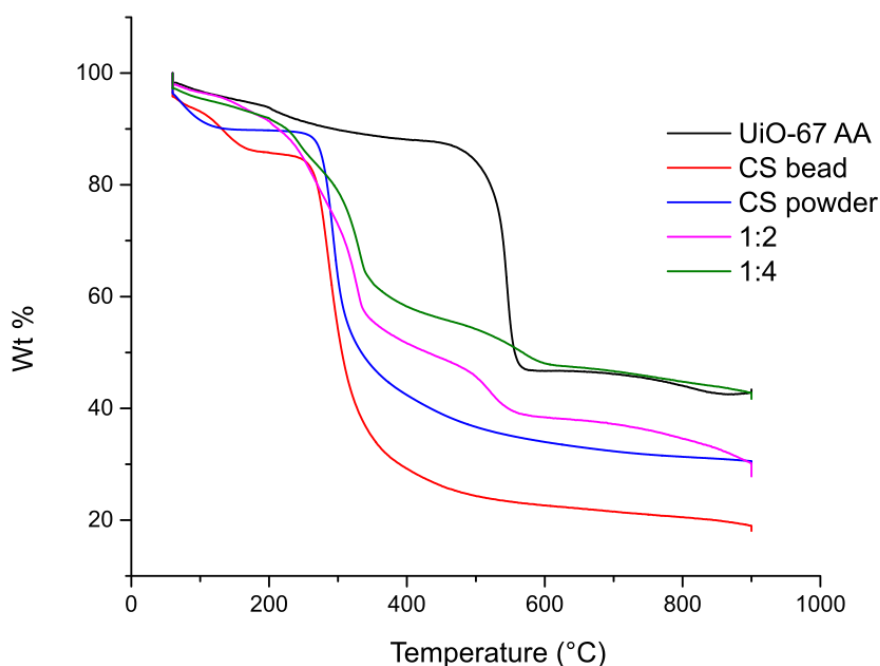


Figure 51. TGA curves for UiO-67 AA, 1:4, 1:2, and CS beads. The pure MOF and the MOF used in the 1:2 and 1:4 beads was sieved and sonicated.

Figures 52 and 53 show the first derivatives of the TGA curves for the 1:4, 1:2, CS beads, CS powder, and UiO-67 AA. Figure 52 shows the initial loss of water from the materials which is followed by the degradation of the CS. The CS bead has a lower inflection point of approximately 285 °C compared to that of the CS powder (approximately 292 °C). This means that CS beads undergo carbonization at a lower temperature than pure CS powder. However, the CS bead has a lower derivative weight change compared to the pure CS powder. The CS bead has a derivative weight change of $-1.03 \text{ \%}/^\circ\text{C}$ whereas the CS powder has a derivative weight change of $-1.21 \text{ \%}/^\circ\text{C}$.

Figure 52 shows that the 1:4 (green) and 1:2 beads (pink) exhibit an initial thermal event at 242 °C and 255 °C, respectively. A second thermal event occurs at 326 °C for the 1:2 bead and at 331 °C for the 1:4 bead. It is difficult to say what these thermal events correspond to. The first two events at 242 and 255 °C are likely the carbonization of CS as discussed previously, however the next set of decompositions at 326 °C and 331 °C are difficult to assign. This may be further CS carbonization or the melting of free BPDC linker present which has a melting point of over 300 °C³⁶. BPDC linker may be melting due to the effects of AA drop-casting which causes MOF decomposition and so a thermal event at a lower than expected temperature is observed. The derivative weight changes of the 1:4 bead at 331 °C and that of the 1:2 bead

at 326 °C are similar. The 1:4 bead experiences a derivative weight change with a maximum of $-0.51\%/^{\circ}\text{C}$ at 331 °C while the 1:2 bead has a weight change of $-0.55\%/^{\circ}\text{C}$ at 326 °C. Further tests are required to elucidate the thermal events occurring in the composite beads.

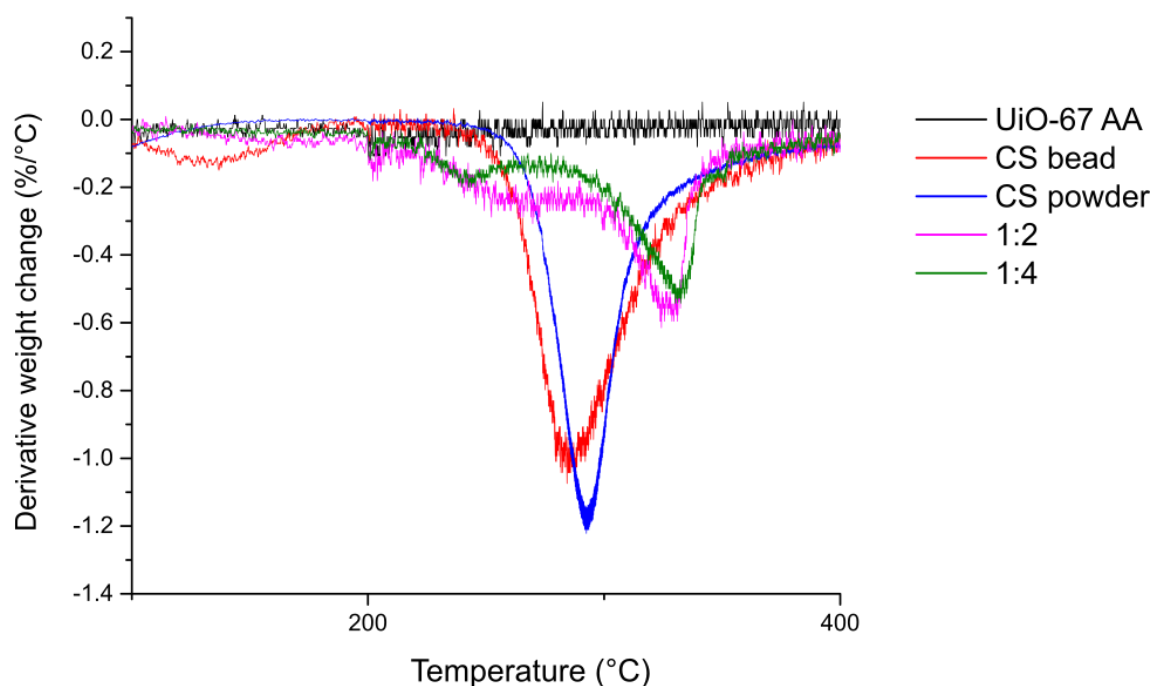


Figure 52. First derivative of TGA curves showing inflection points representing H_2O and CS loss. Two decomposition stages can be observed for the 1:2 and 1:4 beads. This suggests the loss of excess linker which has a melting point of $> 300\text{ }^{\circ}\text{C}$.

Figure 53 shows the derivative weight change of pure UiO-67 AA at 545 °C which represents linker volatilization when it is coordinated to zirconium oxide nodes⁹. However, no such signal can be observed for the 1:2 and 1:4 beads (pink and green curves, respectively). This suggests that there is no MOF present in the 1:2 and 1:4 beads. This is likely due to the effects of drop-casting i.e., the MOF may have been destroyed by AA or liquid N_2 or a combination of both. As was expected, no change is observed for the CS powder and bead. These observations are in line with what was achieved with the stability tests of UiO-67 i.e., drop-casting with AA is decomposing the MOF.

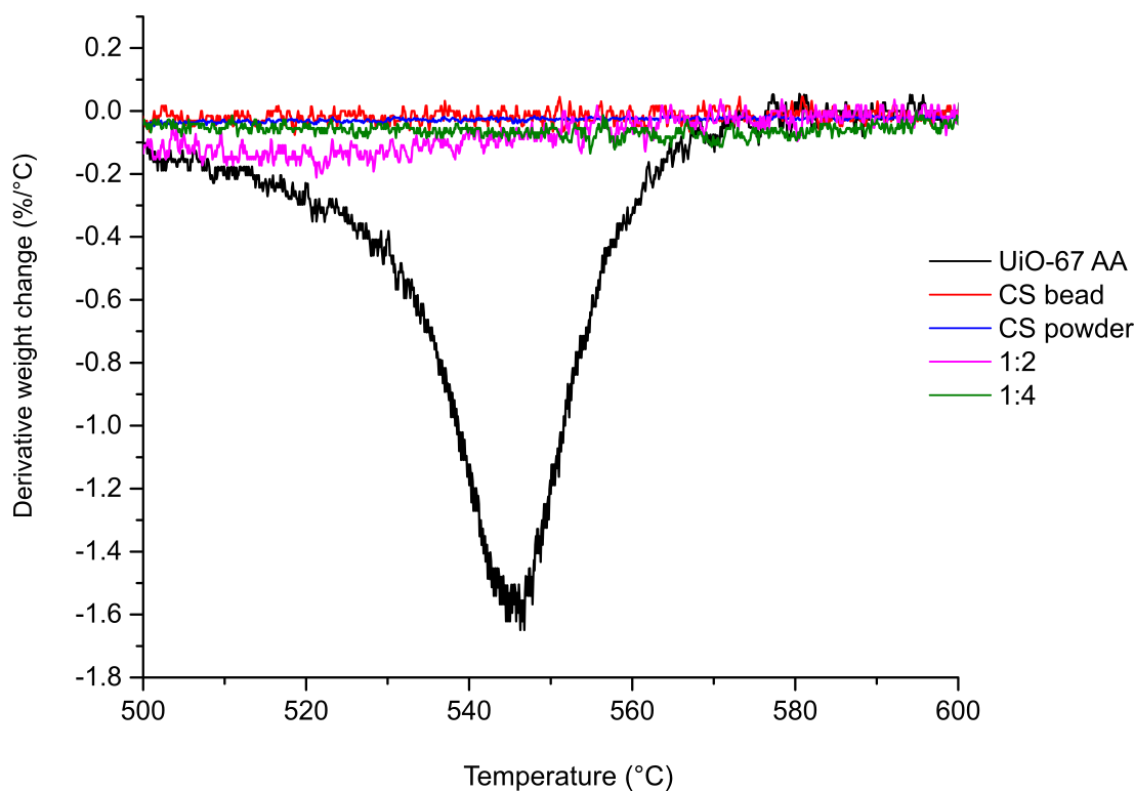
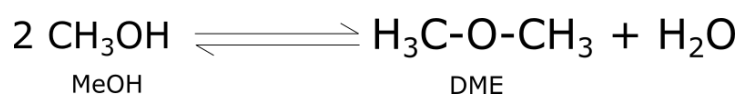


Figure 53. First derivative of TGA curves showing the inflection point representing loss of MOF. Only UiO-67 AA shows a peak implying that no MOF was present in the 1:2 and 1:4 beads.

4. MeOH Conversion Test Reaction

MeOH conversion was chosen as a test reaction to probe the acid sites of UiO-67 since the acid sites may become blocked when they are mixed with CS to form beads. CO-IR could not be used to determine whether or not this was the case since the CS:MOF beads would need to be crushed into pellets for testing. As a consequence of this pelletisation, the true catalytic activity of the active sites would not be represented i.e., the beads need to keep their shape for there to be an accurate analysis of their catalytic activity. To the best of our knowledge MeOH conversion using UiO-67 embedded in a CS matrix has not been reported. A modified setup was used for the initial tests to see whether MeOH conversion was occurring or not. After this a Linkam cell was used to analyse the proliferation of products. As shown in the previous sections, drop-casting appears to degrade the MOF. It was of interest to see whether this impacted the catalytic abilities of UiO-67. The main expected product of MeOH conversion is dimethyl ether (DME) as demonstrated in *Equation 4*. DME may be used as an alternative fuel source in the future in place of conventional liquid petroleum gas which would be beneficial for humanity since it is an environmentally benign fuel³⁹.

Equation 4. Reversible MeOH conversion to DME



The flow rate of MeOH and He (15% MeOH in He) over the MOF was kept at 1 ml min⁻¹ with reaction times of 1 hour and 3 hours for UiO-67 AA. 1:4 CS:UiO-67 AA beads were also tested at 1 ml min⁻¹ with a reaction time of 3 hours. The reactions took place at 120 °C for each cycle with a regeneration step in between each cycle at 150 °C under He. Each cycle showed the proliferation of 4 products: DME; diethyl ether (DEE); unknown product 1; and unknown product 2. These products were identified with an online Rtx-Wax fused silica gas chromatography (GC) column. Figure 54 shows a schematic of the setup used. Only data points exhibiting conversion of MeOH were chosen for the plots showing product formation. Some product data points showed either negative conversion or no conversion was recorded which meant they could not be compared to product data points which did exhibit conversion. For the longer 3-hour reaction time a number of data points showed either negative conversion or no data points were recorded. These points were excluded which explains the shorter than expected reaction times given in the product selectivity plots (Section 4.3).

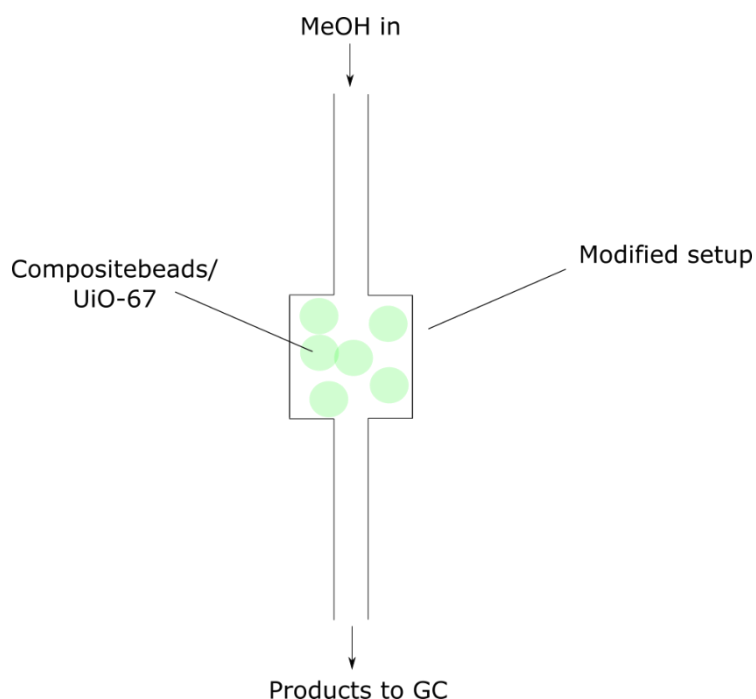


Figure 54. Modified reactor setup showing MeOH flowing over composite beads or UiO-67. Products are then analysed by online GC.

4.1 ATR-IR Results of Sample Preparation and Catalysis

Sieving and pelletisation were carried out to ensure that the reactor did not become clogged with large particles. First the MOF was pressed to form a pellet at 1.5 atm pressure to evenly distribute it. This pellet was then crushed and sieved between a fraction of 425 – 212 µm before being tested for MeOH conversion in the modified reactor setup. The stacked ATR-IR spectra in Figure 55 exhibit the effects of sieving and pelletisation on UiO-67 before catalysis

was conducted. It is evident from the spectra that sieving and pelletisation affected the MOF structure as can be seen from the peak broadening, particularly at 1400 cm^{-1} which corresponds to the $\nu_s(\text{COO}^-)$ stretch.

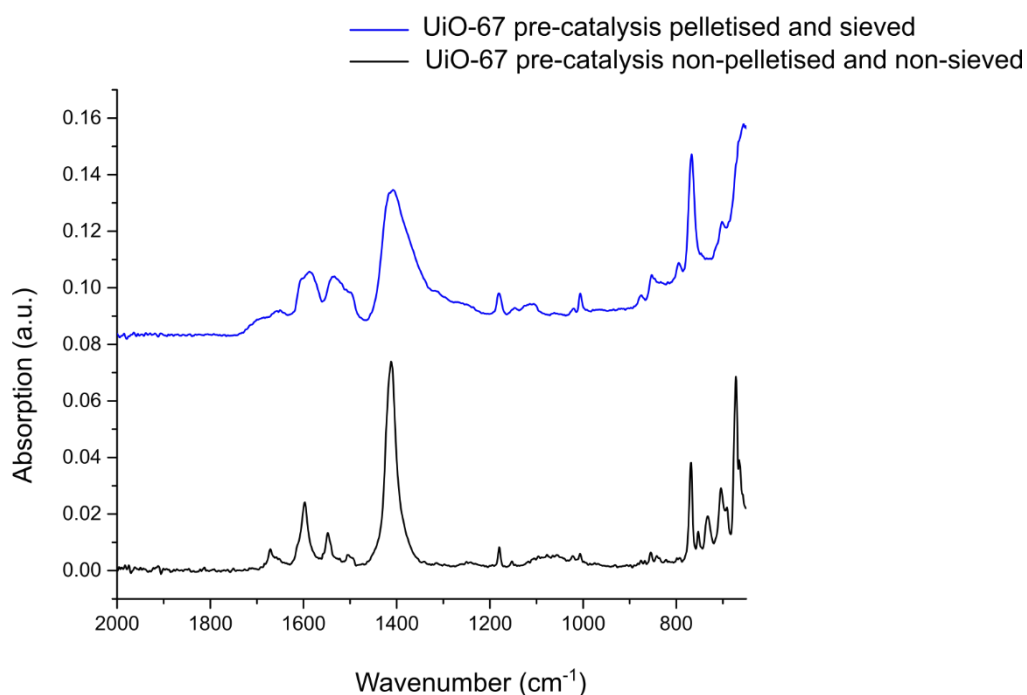


Figure 55. Stacked ATR-IR spectra of pre-catalysis UiO-67 in sieved and pelletised form and non-sieved non-pelletised form

Figure 56 shows the ATR-IR spectra of UiO-67 before (blue) and after it had been tested for MeOH conversion at 5 ml min^{-1} (red) and 1 ml min^{-1} (black) i.e., the effects of catalysis on the ATR-IR spectra of the MOF i.e., peak broadening at 1600 , 1400 , and 769 cm^{-1} (orange highlighted sections). Arrozi *et al.*⁴⁰, reported that peak broadening from $500 - 1000\text{ cm}^{-1}$ and $1500 - 1750\text{ cm}^{-1}$ indicates the presence of remaining organics when UiO-67 was used as a catalyst for the acetalization of benzaldehyde. A similar phenomenon may be occurring here which would explain the peak broadening i.e., organic molecules formed during MeOH conversion may still be present. From this data it is evident that sample preparation for catalysis and the process of catalysis itself were affecting the MOF structure which can be seen by the lower intensity of the ATR-IR spectra.

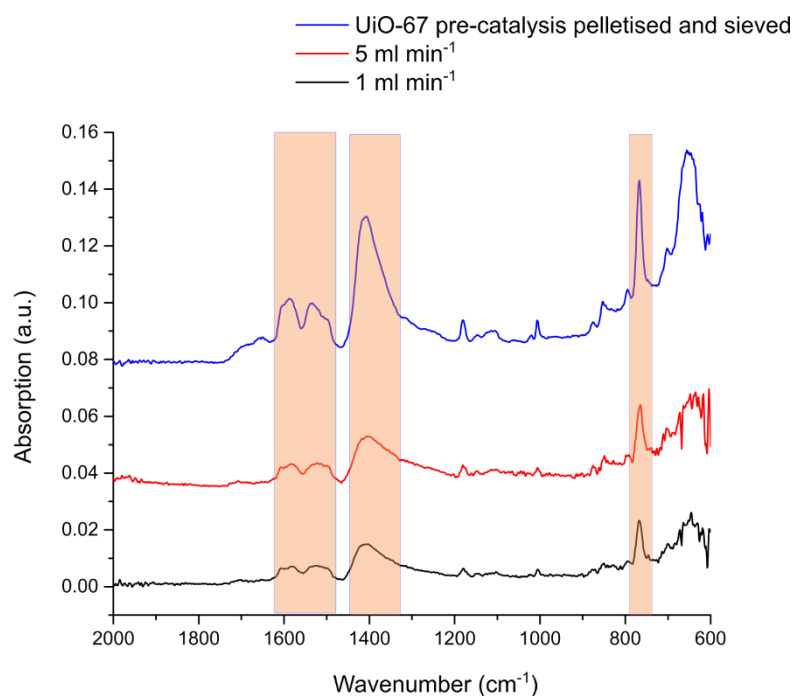


Figure 56. Stacked ATR-IR spectra of pre-catalysis UiO-67, post-catalysis UiO-67 at 1 ml min⁻¹, and 5 ml min⁻¹ flow rate of MeOH in He. All samples were sieved and pelletised. Orange highlighted sections show peak broadening.

4.2 XRD Results of Sample Preparation and Catalysis

XRD data was used to study the effects of MeOH conversion on the crystal structure of UiO-67 AA. From Figure 57 we can see that sieving and pelletisation (blue) reduces the crystallinity of non-sieved and non-pelletized UiO-67 (pink). However, some crystallinity remains in the sieved and pelletized sample. With these diffractograms we can see that mechanical action affects the crystallinity of the MOF substantially.

The crystallinity decreases further after catalysis. Both the 1 ml min⁻¹ (red) and 5 ml min⁻¹ (black) flow rates appear to affect the crystal structure in the same way i.e., there appears to be a total loss of crystallinity for both samples. Yang *et al*⁴¹ reported the trade off between catalytic activity and stability in terms of missing linker defects. Their work demonstrated that MOFs with greater amounts of missing linker defects are deactivated more easily than those which possess more linkers, however MOFs with greater amounts of missing linker defects tend to exhibit greater catalytic activities. XRD data of UiO-66 and UiO-67 synthesized with a HCl modulator in their work showed rapid deactivation during ethanol dehydration, similar to what is witnessed here. The deactivation was attributed to the unzipping of the MOF structure due to the esterification of the linker carboxylate groups by ethanol. This would explain the loss of crystallinity observed in the post-catalysis XRD data given in Figure 57.

Figure 50 demonstrated that the BPDC linker may be displaced by an AA modulator even if the MOF framework does not have defective linker sites⁴². In this case, the MOF structure may be decomposed further when MeOH is flowed over the MOF during catalysis i.e. methoxy ligands may displace the acetate ligands which were introduced by the AA modulator. The diffractograms give insight into the effects of mechanical pressure from sieving as well as the effects of MeOH flow on the crystal structure of the MOF.

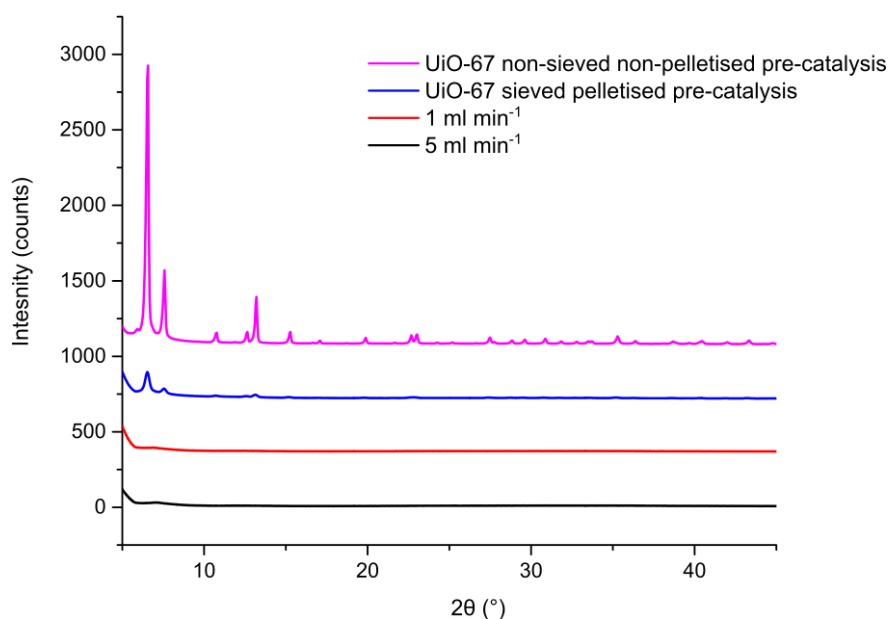


Figure 57. XRD diffractograms of UiO-67 pre-catalysis non-sieved, non-pelletised (pink), UiO-67 pre-catalysis sieved and pelletised (blue), and post-catalysis sieved and pelletised with MeOH/He flow rates of 1 ml min⁻¹ (red) and 5 ml min⁻¹ (black).

Figure 58 shows how acetate ligands may be displaced by methanol during catalysis. Zhuang *et al*⁴³ demonstrated that MeOH is capable of displacing formate ligands from the Al₃O nodes of MIL-100 during catalysis to yield monodentate and bidentate methoxy ligands on the node defect sites. Acetate ligands may also be displaced by methoxy ligands during methanol dehydration. These methoxy species were shown to be intermediate species for catalytic methanol dehydration to yield DME. In this way, node ligands help control the catalytic activity of the MOF. A similar situation may be happening with UiO-67 since UiO-66 (an analogue of UiO-67) shares similarities with MIL-100 due to the presence of metal oxide nodes (Al₃O for MIL-100, and Zr₆O₈ clusters for UiO-66). The breakdown of these nodes affects the efficacy of the catalyst for MeOH conversion. Wei *et al*⁴⁴ showed that the number of defect sites present in UiO-66 increased dramatically with the amount of AA modulator used and that these defects were primarily missing linkers. Their research also showed that number of acetate ligands per missing linker node increased with increasing modulator concentration used during synthesis.

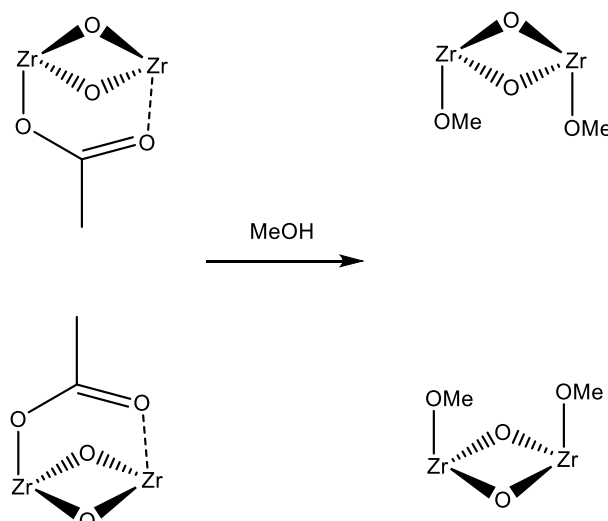


Figure 58. Methoxy ions from MeOH displacing acetate ligands on UiO-67

4.3 Product Selectivity and MeOH Conversion

The selectivity results for the products formed during MeOH conversion are given in this section. The flow rate and reaction times were varied to determine their effects on product selectivity and MeOH conversion. 3 cycles were carried out for each experiment with a regeneration step in between each cycle to remove any remaining MeOH/products formed. The 3 cycles were conducted to observe how effective MeOH conversion was with each regeneration i.e. the longevity of the catalyst.

Pure UiO-67 AA which was pelletised and sieved prior to catalysis was tested with a MeOH/He flow rate of 1 ml min⁻¹ at 1- and 3-hour reaction times. As mentioned previously the MOF is degraded with pelletisation and sieving. Unknown products 1 and 2 were produced during catalysis, most likely as a result of this mechanical breakdown. The flow of MeOH over the degraded MOF may also explain the formation of these unknown products. A 1:4 CS:MOF bead was also tested with a flow rate of 1 ml min⁻¹ with a reaction time of 3-hour per cycle. These beads were not sieved or pelletised but kept whole.

The products obtained from cycle 1 of MeOH conversion with a 1-hour reaction time using UiO-67 AA are depicted in figure 59. DME is formed initially with a selectivity of 84.5%. This rapidly to less than 2% by the end of the cycle. Unknown product 2 starts forming after the 10-minute mark reaching a maximum of 81.4%. Unknown product 1, like unknown product 2, is formed in low amounts at the start of the cycle but its production increases at the 10-minute mark to approximately 29.7%. However, after the 10-minute mark its production decreases. DEE is formed in negligible quantities throughout the cycle, reaching a maximum production of 2.3% at the 6-minute mark. This then falls to below 1% for the rest of the cycle.

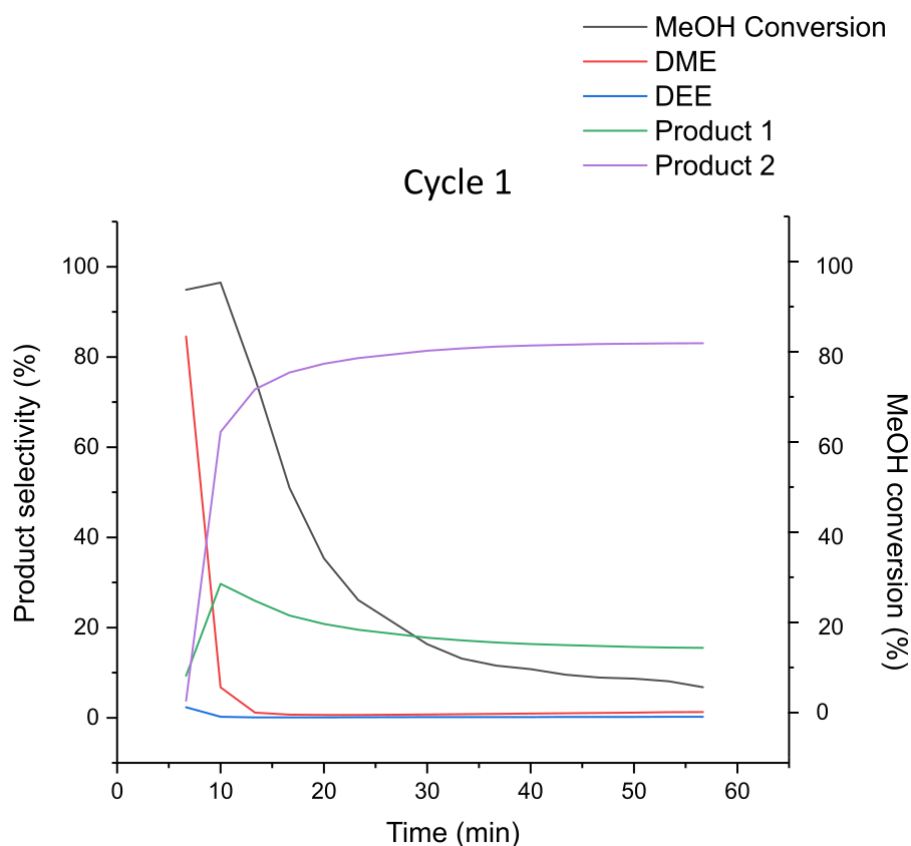


Figure 59. Cycle 1 of MeOH conversion at 1 ml min^{-1} of MeOH/He for UiO-67 AA with 1-hour reaction time. High concentrations of product 2 are met with low MeOH conversion %. DME formation declines rapidly in the early stages of the reaction.

It is likely that the unknown products are either fragmented linker which was displaced as a result of pelletisation and sieving or by acetate ligands being desorbed as methyl acetate in the presence of MeOH⁴³ (or perhaps a combination of both). The initial rise in MeOH conversion with DME production suggests that MeOH is being converted to DME at the start of the reaction i.e., the acid sites of UiO-67 AA are catalytically active for MeOH conversion. After the apex of DME production we see a decline in MeOH conversion while the production of unknown product 2 (and to a certain degree, the production of unknown product 1) rises. It is likely that this is occurring as a result of the mechanical degradation from sieving and pelletising of the MOF which prevents the active sites from converting MeOH to DME. Instead there is only the proliferation of the fragmented linker and/or methyl acetate.

Figure 60 shows cycle 2 which follows a similar trend to that of cycle 1 but with initially higher concentrations for unknown products 1 and 2. This suggests that greater amounts of broken down linker are displaced or methyl acetate is desorbed in greater amounts from the node defect sites with each new cycle. Unknown product 1 is initially produced in higher concentrations compared with cycle 1 but plateaus early on. DME is formed in initially lower quantities compared to cycle 1. It's production decreases from 156.66 minutes onwards to negligible values. DEE is formed in minimal amounts throughout. Once again, MeOH conversion increases with increased production of DME in the initial stages of the cycle but decreases when the formation of DME ceases. This is met with an increase in the production

of unknown products 1 and 2, similar to cycle 1. This implies that the acid sites of UiO-67 are affected by the presence of unknown product 2.

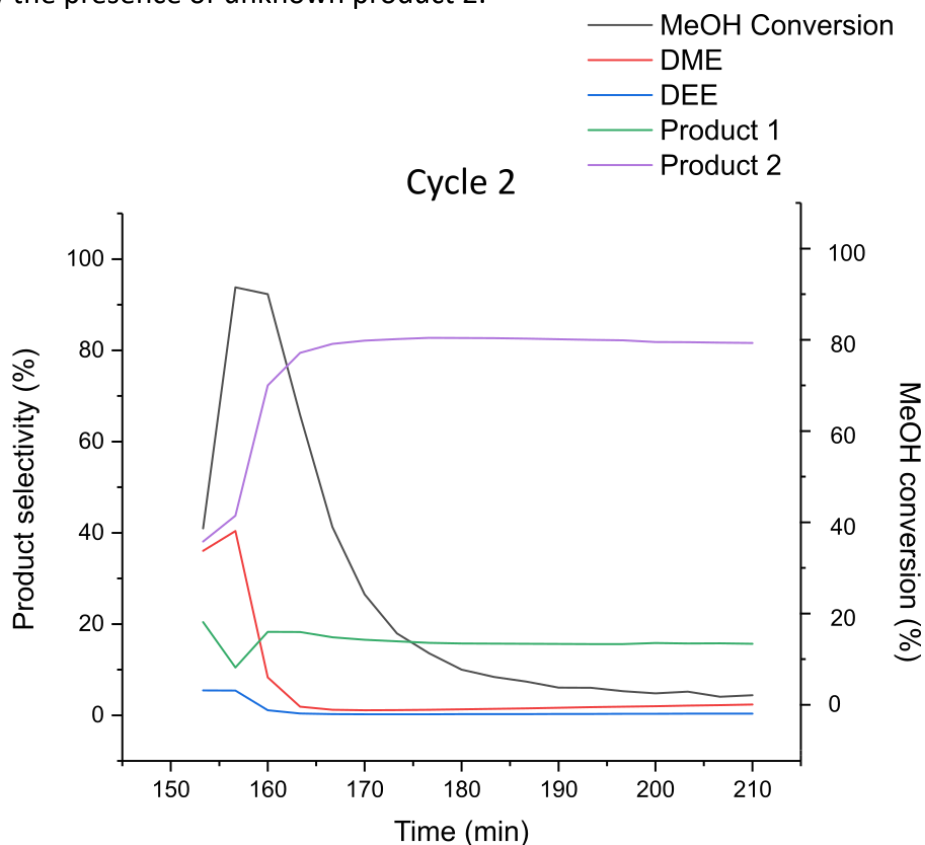


Figure 60. Cycle 2 of MeOH conversion at 1 ml min^{-1} of MeOH/He for UiO-67 AA with 1-hour reaction time. MeOH conversion % starts at a lower value compared to cycle 1 but quickly increases with DME production. MeOH % conversion declines with product 2 formation.

Cycle 3 in Figure 61 shows an initial increase in DME production similar to cycle 2 and 1, however this decreases after 306.66 minutes. Like the first two cycles, the conversion of MeOH increases initially with DME selectivity which shows that the acid sites are active for MeOH conversion but decreases dramatically after DME selectivity decreases and unknown product 2 selectivity increases i.e., unknown product 2 is not a product of MeOH conversion. It can be reasoned that unknown product 2 is linker which has been broken down by sample preparation. This broken down linker is then removed by the flow of MeOH which explains its increase in selectivity with increasing reaction time.

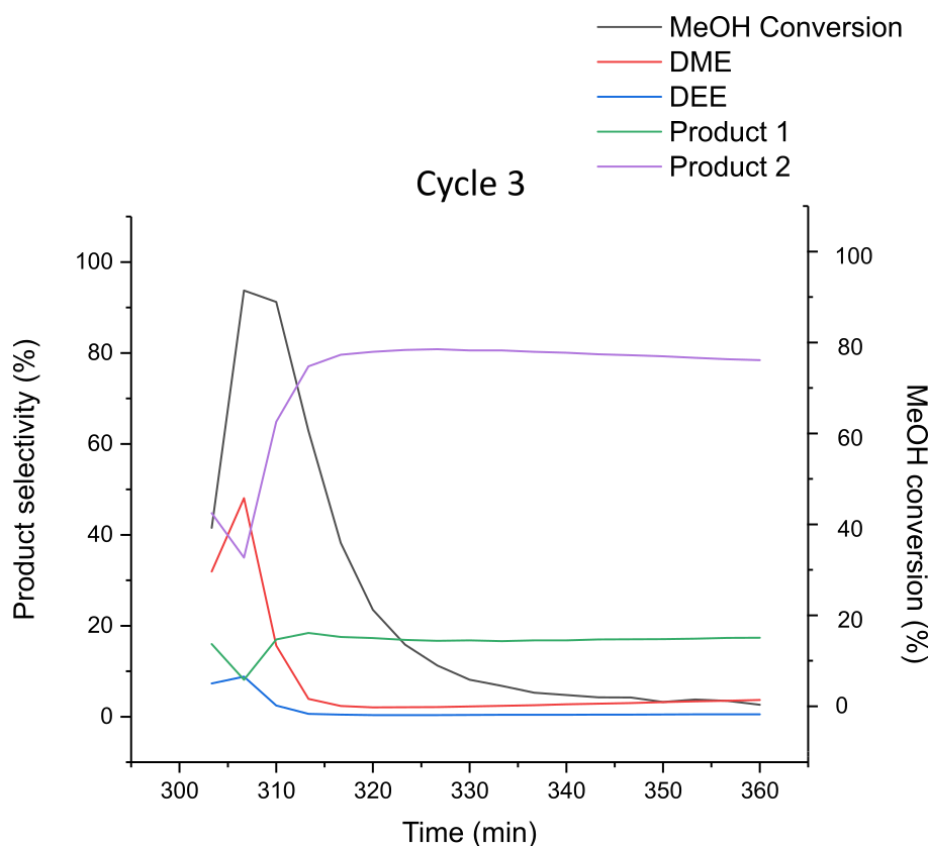


Figure 61. Cycle 3 of MeOH conversion at 1 ml min^{-1} of MeOH/He for UiO-67 AA with 1-hour reaction time

The same flow rate was used but with a longer reaction time of 3 hours for UiO-67 AA. Once again, only data points exhibiting conversion were included from the 3 cycles. Cycle 1 of the 3-hour reaction setup is shown in Figure 62. In contrast to cycle 1 of the 1-hour experiment, unknown product 1 was formed in the highest concentration reaching a maximum concentration of 80% at the 10-minute mark. Unknown product 2 is initially present at 15%, however it gradually increases with time and seems to converge with the profile of unknown product 1. DME and DEE are initially present in low amounts (22% and 7.3%, respectively) at the beginning of the experiment. Their values decrease to negligible quantities after this with DEE being produced in slightly higher quantities than DME.

MeOH conversion decreases throughout the entirety of the cycle. This is likely due to the low DME formation and the concurrent increase in product 2 formation, as was the case with the 1-hour reaction time experiment. Many of the data points for this experiment exhibited either negative values or no values at all which might suggest that this experiment produced unreliable data, as shown by the shorter than expected reaction time x-axis. The decrease in MeOH conversion and increase in product 2 formation is in agreement with the 1-hour experiment previously described suggesting that mechanical breakdown of the MOF was affecting the catalytic activity of the acid sites of the MOF. However, the comparatively higher formation of unknown product 1 was unexpected as was the negligible formation of DME.

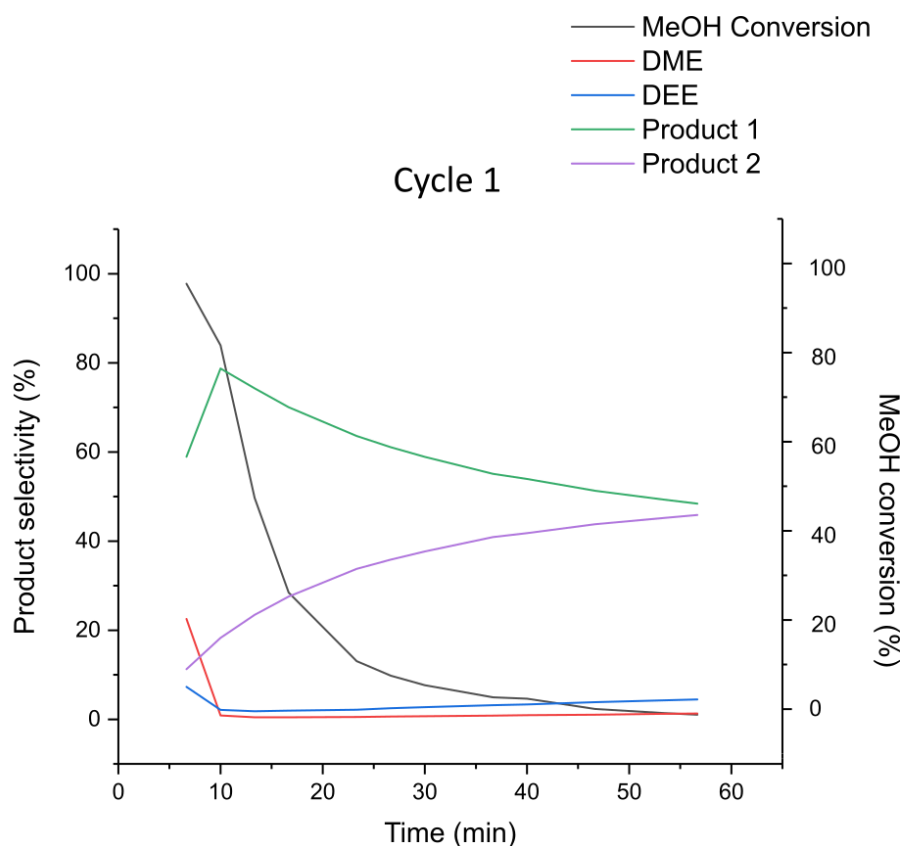


Figure 62. Cycle 1 of MeOH conversion at 1 ml min^{-1} of MeOH/He for UiO-67 AA with 3-hour reaction time

Cycle 2 for the 3-hour reaction time setup is shown in Figure 63. Similar to cycle 2 of the 1-hour setup (Figure 60), mirroring in the product profiles between unknown product 1 and DEE and between unknown product 2 and DME was observed. The formation of products 1 and 2 appear to converge with time, as was the case in cycle 2 of the 1-hour reaction. The conversion of MeOH in this cycle seems to increase with the increased production of unknown products 1 and 2 at the start of this cycle. This is contrary to the data we have seen up until this point. However, there is a substantial decrease in MeOH conversion when the production of unknown products 1 and 2 increases past the 283.33 minute mark which supports the data obtained from the previous cycles. This again suggests that the acid sites of the MOF are inhibited by the formation of products 1 and 2 which are likely formed as a result of mechanical degradation.

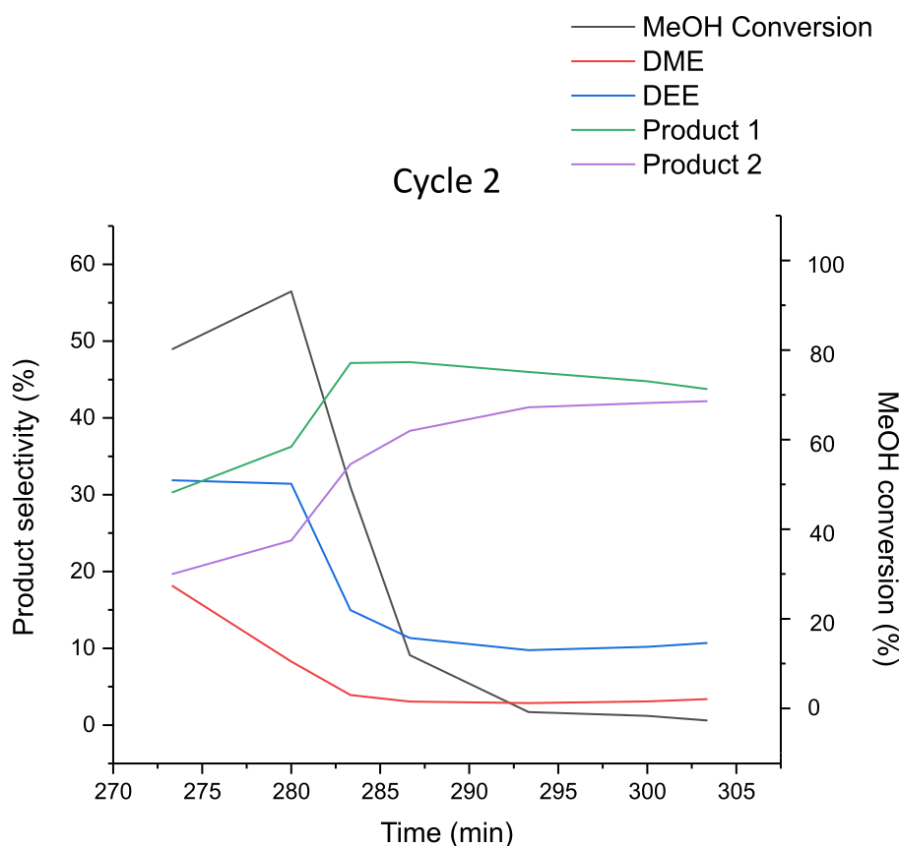


Figure 63. Cycle 2 of MeOH conversion at 1 ml min^{-1} of MeOH/He for UiO-67 AA with 3-hour reaction time

Cycle 3 depicted in Figure 64 shows an even stronger mirroring in the product profiles. In this cycle DEE has the highest initial selectivity reaching a maximum of 62.9%. The formation of DEE drops to approximately 19.5% after this. DME is initially the second most formed product at 24.5%, however its production declines to approximately 7.5% for the rest of the cycle. MeOH conversion increases initially with increasing amounts of DME, and DEE being formed during the cycle which shows that the acid sites of the MOF are converting MeOH to DME and DEE. The decline of DME and DEE production is met with a decrease in MeOH conversion along with an increase in unknown products 1 and 2 formation at the 546.66 minute mark. Once again the decline in the formation of DME and DEE is a consequence of the acid sites of the MOF being inhibited by the formation of unknown products 1 and 2.

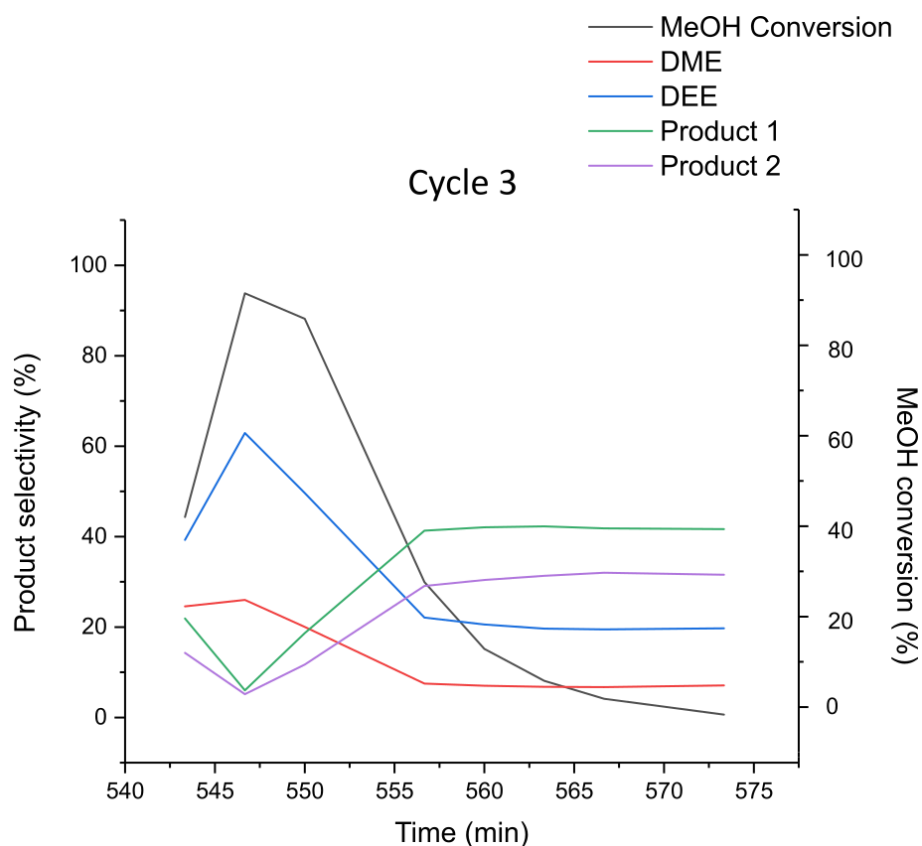


Figure 64. Cycle 3 of MeOH conversion at 1 ml min^{-1} of MeOH/He for UiO-67 AA with 3-hour reaction time

The following data represents the 3 cycles of methanol product selectivity using a 1:4 CS:UiO-67 bead with a flow rate of 1 ml min^{-1} MeOH/He and a reaction time of 3 hours. The product selectivity profile for cycle 1 of the 3-hour 1:4 CS:UiO-67 bead in the modified setup as depicted in Figure 65 shows a lower starting MeOH conversion percentage compared to the first cycles of the 1-hour and 3-hour reactions for pure UiO-67. This is likely due to the MOF being degraded as a result of AA drop-casting and the presence of CS which may block the active sites of UiO-67. The low MeOH conversion % and the proliferation of unknown product 2 which is likely degraded linker shows that the catalytic ability of the MOF is reduced as a result of drop-casting. Unknown product 2 has the highest product selectivity reaching a maximum of 97 % early on in the cycle. The conversion percentage of MeOH decreases as the formation of unknown product 2 increases. The selectivity for all other products is negligible.

The low concentration of products formed may be due to acetate ligands blocking the active sites of UiO-67 AA in the bead. This phenomenon was reported by Yang *et al*⁴¹ on UiO-66 with methanol dehydration as a test reaction. In their research the catalytic deactivation of UiO-66 synthesised with an AA modulator was caused by MOF degradation after the acetate ligands introduced by the modulator had desorbed from the MOF defect sites as methyl acetate which occurred at 473 K. The study did not attempt to conduct this reaction at temperatures lower than 473 K so it cannot be said whether this is the case for the experiments conducted here at 393.15 K (120 °C). Methyl acetate may be one of the unknown products we observe here, the other unknown product is likely BPDC linker which was displaced by drop-casting with AA.

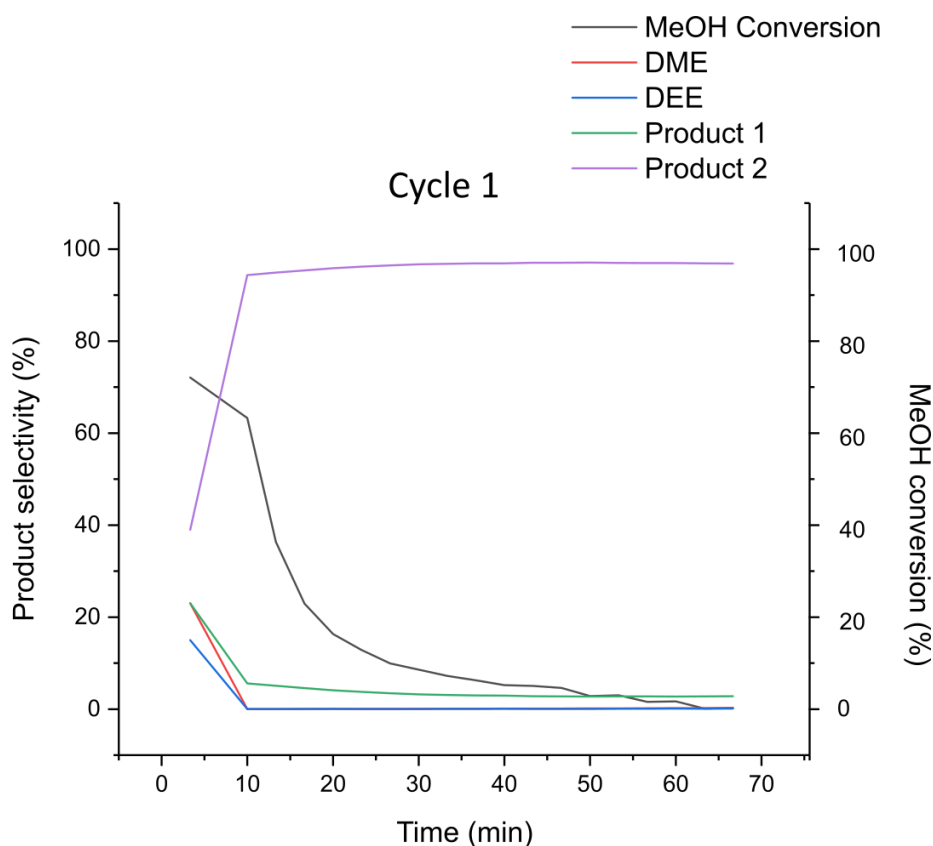


Figure 65. Cycle 1 of MeOH conversion at 1 ml min^{-1} of MeOH/He for 1:4 CS:UiO-67 beads with 3-hour reaction time

Cycle 2 in Figure 66 shows an increase in the percentage of MeOH conversion in the early stages of the experiment. DME and DEE are produced during this increased conversion while the selectivity for unknown product 1 and 2 decreases. This shows that the acid sites of the MOF in the bead are still capable of MeOH conversion even after drop-casting has been carried out which led to MOF decomposition as shown in previous sections. This observation also suggests that the CS is not blocking the active sites of the MOF since we see DME and DEE being formed, albeit at low quantities. The conversion of MeOH reaches a maximum of 93.87% before it begins to decline at the 270-minute mark. The selectivity for DME and DEE also decreases at this point while the selectivity for unknown product 2 increases, again suggesting that the active sites are affected by its proliferation.

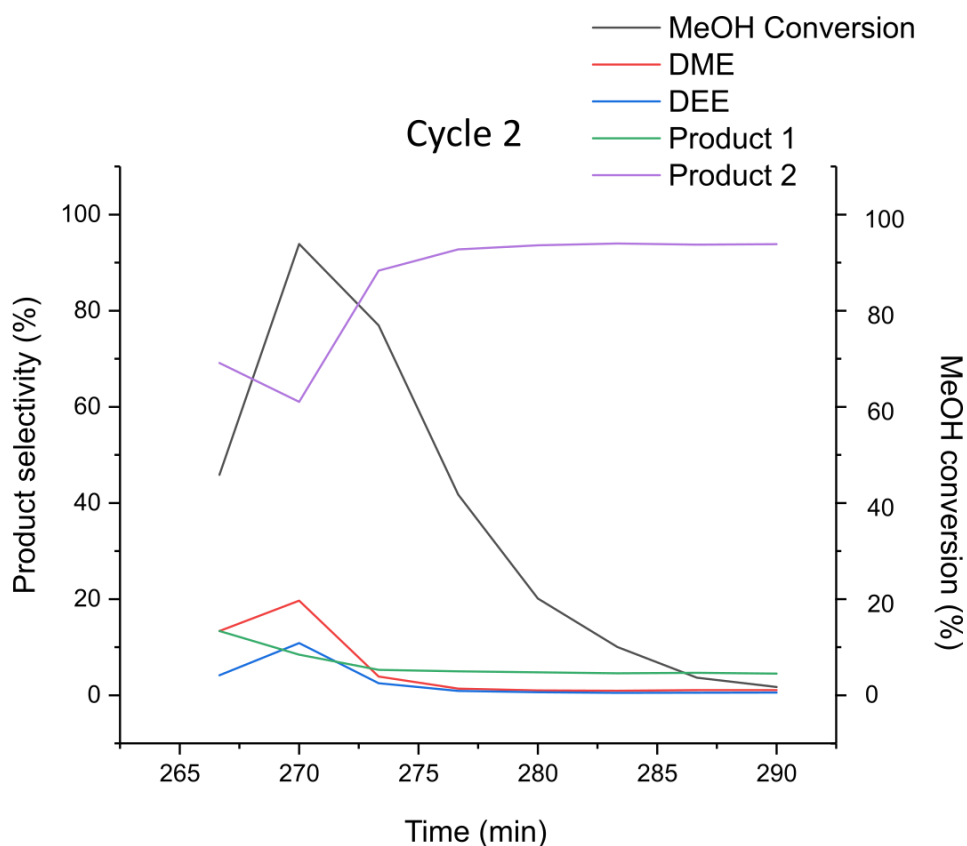


Figure 66. Cycle 2 of MeOH conversion at 1 ml min^{-1} of MeOH/He for 1:4 CS:UiO-67 beads with 3-hour reaction time

Cycle 3 in Figure 67 shows a maximum MeOH conversion of 92.81 %. The increase in MeOH conversion is met with an increase in DME selectivity. In fact the DME selectivity of this cycle is close to that of cycle 3 for pure UiO-67 AA with a 1-hour reaction time at 1 ml min^{-1} MeOH/He flow rate which is given in Figure 61. The DME selectivity reached a maximum of approximately 46 % for pure UiO-67 while it reaches a maximum of around 40 % for the 1:4 CS:UiO-67 AA bead here. As in the previous cycles, DME selectivity increases with increasing MeOH conversion while unknown product 2 selectivity decreases. This high selectivity for DME in this cycle suggests that the acid sites of the MOF are still quite active, almost as active as when pure MOF was used under similar reaction conditions. This tells us that the 1:4 CS :UiO-67 AA bead is capable of converting MeOH to DME.

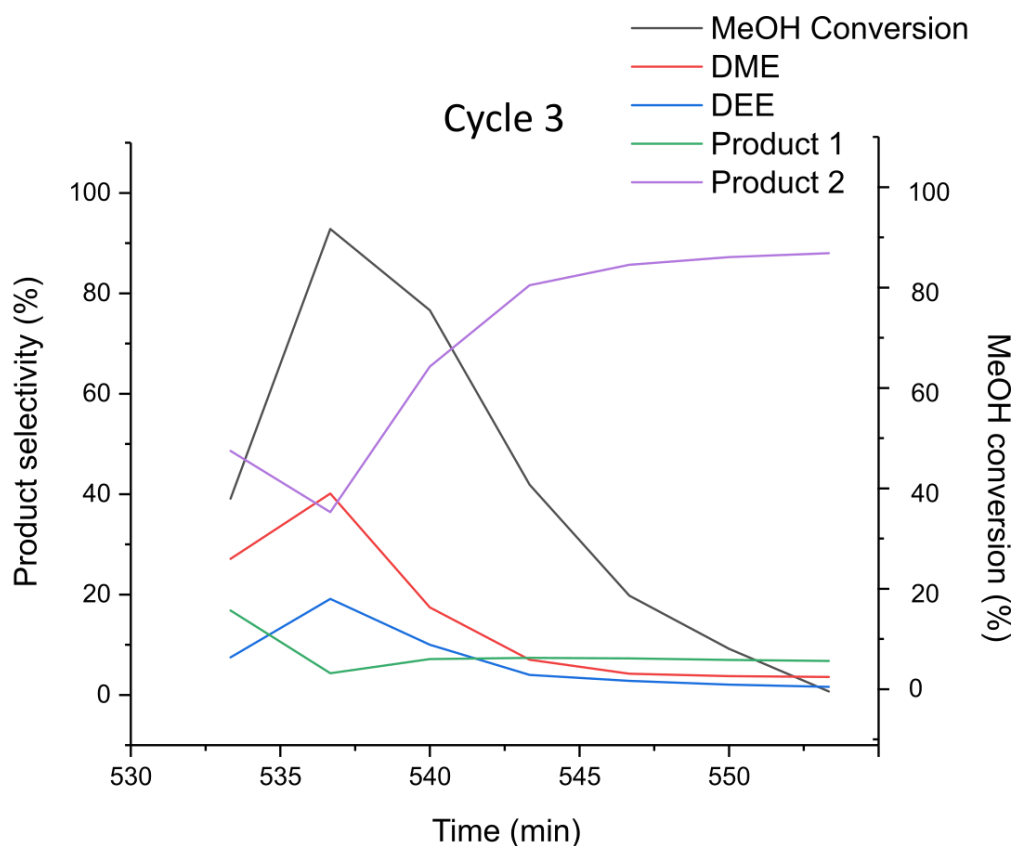


Figure 67. Cycle 3 of MeOH conversion at 1 ml min^{-1} of MeOH/He for 1:4 CS:UiO-67 beads with 3-hour reaction time showing MeOH conversion and DME production

Unknown products 1 and 2 may be present as a consequence of MeOH “washing” the MOF. To test this a 1:4 bead ratio was subjected to MeOH. Figure 68 shows the ATR spectra of the BPDC linker (pink), a 1:4 bead ratio (blue), and a 1:4 bead ratio which was subjected to MeOH (red). The orange highlighted boxes indicate characteristic BPDC linker peaks which are of course present in the linker spectrum but also in the spectrum of the 1:4 bead. The displacement of the BPDC linker from the MOF structure as a result of drop-casting using AA is what causes the proliferation of these peaks in the 1:4 bead spectrum. However, these peaks are not present in the spectrum of the 1:4 bead which was washed with MeOH. This is likely due to the MeOH “washing away” the excess linker which was displaced by the AA in drop-casting. The MeOH may be displacing the acetate ligands which were introduced by AA in drop-casting with methoxy ligands which has been observed in UiO-66 treated with methanol⁴⁵. The acetate ligands may have desorbed from the MOF surface as methyl acetate which is likely one of the unknown products (most likely unknown product 2 because of its higher concentration and selectivity). Further in-situ data will be needed to determine if this is in fact the case.

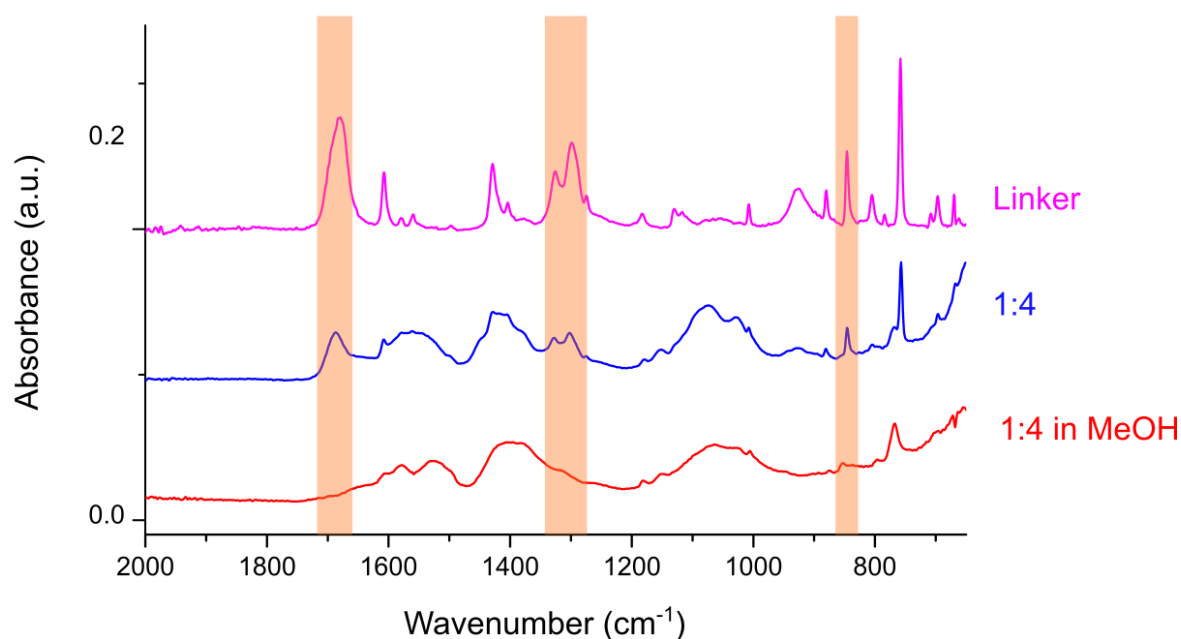


Figure 68. ATR-IR spectra of BPDC linker, 1:4 bead and 1:4 bead washed with MeOH. The orange highlights represent characteristic linker peaks which are present in the 1:4 bead but absent for the 1:4 bead washed with MeOH

4.4 MeOH conversion using a linkam cell

The same sieving and pelletising conditions were used for methanol conversion in a linkam cell. 10% MeOH/N₂ with a flow rate of 10 mL min⁻¹ was flowed over 50.0 mg of UiO-67 AA in the linkam cell, and the resulting products were isolated in a bubbler containing dichloromethane (DCM). The DCM and products it contained were then measured using offline GC-MS. As seen in the previous sections, two unknown products were identified when conducting MeOH conversion experiments on UiO-67 in the modified setup. The aim of using the linkam cell was to establish the identity of these products which had retention times of 2.90 and 2.95 minutes. An Agilent CP97713 column was used to analyze the products obtained. As previously stated, the potential identities of unknown products 1 and 2 were considered to be either defective linker or methyl acetate. Methyl acetate may have been formed via the esterification of the acetate ligands at the MOF node defects by methanol. Mekala and Goli⁴⁶ studied this reaction using sulfuric acid as a catalyst and determined that the reaction rate is dependent on both the temperature of the system and the concentration of the catalyst. Their studies showed that this reaction reaches equilibrium in 100 minutes at 333.15 K. Yang *et al*⁴¹ demonstrated that methoxy and acetate ligands adsorbed to the acid sites of UiO-66 are capable of forming methyl acetate during MeOH dehydration, although this was observed at a higher temperature in their case (473 K for their reaction versus 393.15 K here).

The first signal obtained at a retention time of 2.90 minutes had a single peak at $m/z = 58$ which is given in Figure S1. However, this was likely due to remaining acetone still present in the column from washing since acetone has a peak at 58 m/z ⁴⁷. Ethene methoxy, like acetone, also has a peak at 58 m/z , albeit with a greater intensity⁴⁸. Further in-situ data is required to determine the structure of this product.

The mass spectrum with a retention time of 2.95 had peaks at 55 and 70 m/z as depicted in Figure S2. Figure 69 shows the mass spectrum of 2-propenoic acid which exhibits major peaks at 55 and 72 m/z⁴⁹ similar to the peak m/z values which were obtained for the product at 2.95 minutes retention time. However, the peak intensities are different for the two spectra. Once again, more in-situ GC-MS data is required to elucidate the exact nature of these unknown products.

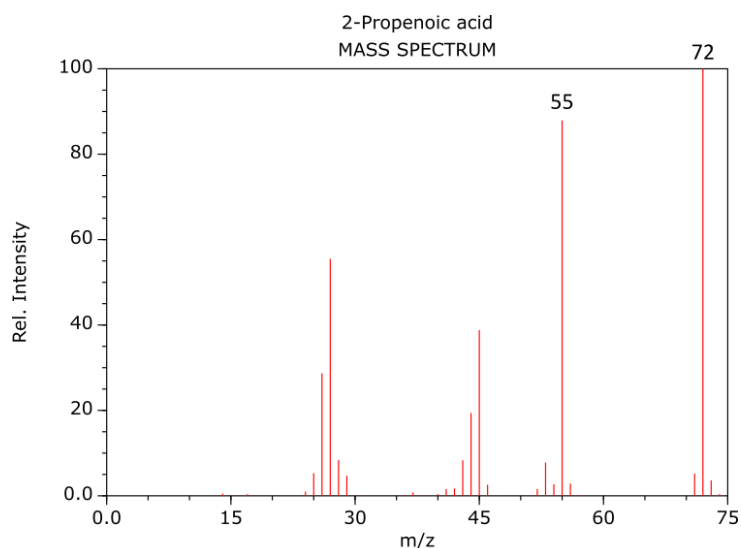


Figure 69. GC-MS of 2-propenoic acid (reproduced from Reference 49)

4.5 Pre- and Post-Catalysis SEM-EDX Regional Analysis of 1:4 Bead

A 1:4 bead was chosen for SEM-EDX experiments which sought to analyse the differences in chemical weight concentrations before and after MeOH conversion catalysis. The objective of these measurements was to determine whether MeOH conversion had any influence on the chemical composition of the 1:4 bead. Regional analyses conduct SEM-EDX measurements at every point of the image which gives the chemical weight concentration of everything depicted in the SEM image. The SEM images depicted in Figure 70 show the bead pre-catalysis (A) and post-catalysis (B).

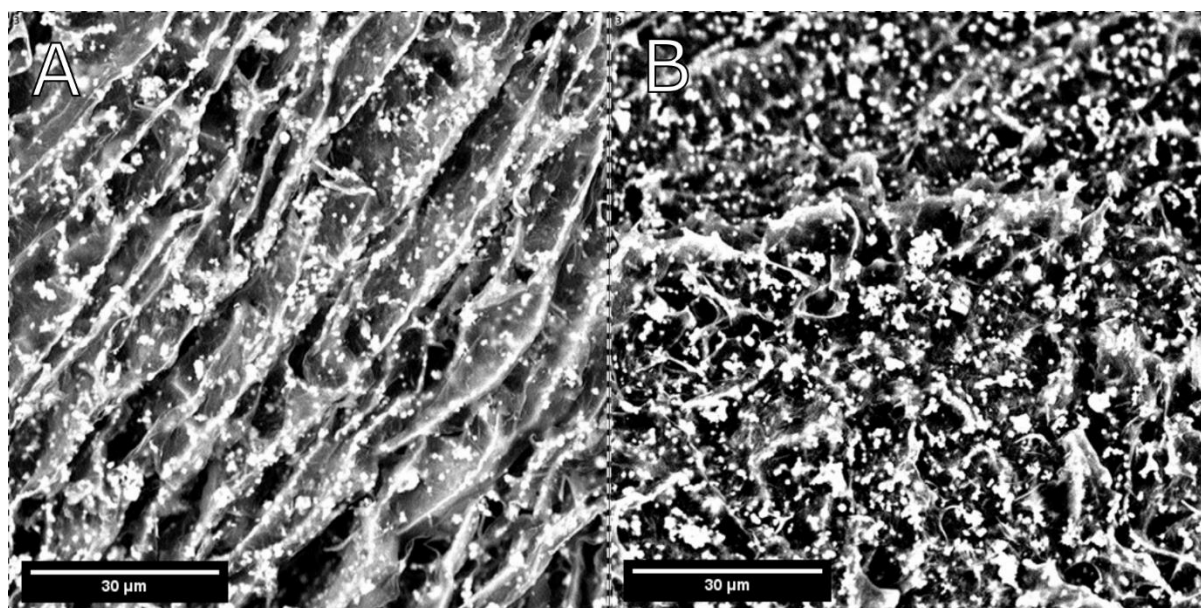


Figure 70. Regional SEM-EDX analysis of 1:4 bead pre-catalysis (A) and 1:4 bead post-catalysis (B)

Table 5 shows the elemental weight concentrations obtained from the SEM-EDX analysis of the 1:4 bead pre- and post-catalysis. Zirconium is lower in the post-catalysis case (23.6 % for pre-catalysis and 11.3 % for post-catalysis). This is likely due to the extensive breakdown of the MOF when subjected to catalytic conditions after drop-casting has already left uncoordinated metal clusters which may have been removed by the flow of MeOH.

Table 5. SEM-EDX weight concentration results for regional analysis of 1:4 bead pre- and post-catalysis

Element	1:4 bead pre-catalysis weight concentration (%)	1:4 bead post-catalysis weight concentration (%)
Carbon	46.0	49.4
Oxygen	30.3	39.3
Zirconium	23.6	11.3

5. Conclusions and Outlook

From the results obtained, it appears that AA used for drop-casting the beads was causing the MOF to degrade. The ATR-IR data of UiO-67 AA which was subjected to AA after synthesis showed the proliferation of peaks which resembled the BPDC linker. The ATR-IR spectra depicted in Figure 47 showed the occurrence of peaks at 1700 cm^{-1} , 1300 cm^{-1} , and 825 cm^{-1} after the MOF had been subjected to acetic acid and when it was drop-casted with AA. These peaks are all characteristic BPDC linker peaks. These peaks were absent from the MOF sample which was not subjected to acetic acid suggesting that drop-casting with AA was degrading the MOF. TGA data corroborated this observation as thermal degradation was observed for a MOF sample which was drop-casted using AA at 326°C . This temperature is closer to the melting point of free BPDC linker which occurs at 325°C . A MOF sample which was not drop-casted with AA showed thermal degradation at 545°C , the temperature at which thermal degradation of the MOF is expected to occur. This implies that the MOF sample which was drop-casted with AA was degraded and MOF was no longer present. Thermograms of the 1:2

and 1:4 bead ratios also showed no degradation at 545 °C which also implies the absence of any MOF. Again, these beads were drop-casted using AA so MOF degradation was most likely occurring.

The calibration curve obtained from the absorbance ratio between characteristic MOF (769 cm^{-1} , Zr-O-Zr stretching) and CS (1027 cm^{-1} , C-O stretching) peaks for the determination of MOF percentages in different composite ratios showed a low concentration of MOF in the 1:4 bead ratio. This was in agreement with the ATR-IR and TGA data mentioned above i.e. the MOF was being degraded in the bead as a result of drop-casting using AA. A sample of MOF drop-casted with AA was also analysed using this calibration curve. The percent of MOF present in this sample was also very low at 5.01% which again implied that the MOF was degraded by the AA.

It was also shown that sieving and pelletising the MOF caused structural degradation which was evident from the ATR-IR spectra and XRD data obtained (see Section 4.2). MeOH conversion at 1 ml min^{-1} and 5 ml min^{-1} were seen to cause further degradation of the MOF's crystal structure which was exemplified by ATR-IR and XRD data. MeOH conversion was observed during the production of DME which shows that the MOF possessed catalytically active acid sites. The conversion of MeOH was shown to decrease with decreasing DME production. This trend was met with an increase in the selectivity of unknown product 2 which suggests that the formation of product 2 inhibits the catalytic conversion of MeOH to DME. Unknown product 2 was likely broken down linker which had been produced as a result of drop-casting with AA and mechanical action from the sample preparation. Tests involving MeOH suggested that the broken linker could have been "washed away" by the flow of MeOH in the catalytic testing. ATR-IR spectra of a 1:4 bead (Figure 68) showed peaks which were characteristic of the BPDC linker however washing the beads with MeOH caused these peaks to disappear meaning the linker was no longer present i.e. the MeOH had most likely washed away the broken down linker.

The highest percentages of unknown product 2 selectivity were observed for the 1:4 bead catalytic test. This was to be expected since drop-casting with AA is involved in the bead synthesis which creates an excess of free linker as demonstrated by ATR-IR data which was acquired prior to testing. The percentage of unknown product 2 formed decreased with subsequent catalytic cycles of the 1:4 bead. At the same time DME production and MeOH conversion increased with each new cycle. This shows that MeOH conversion is occurring within the beads even after the MOF was degraded by drop-casting i.e., there is still a small amount of MOF present in the bead which possesses catalytic acid sites allowing for MeOH conversion. This also demonstrates that CS in the bead did not block the active sites of the MOF since MeOH conversion was occurring. The broken down linker was most likely washed away the flow of MeOH which explains the decrease in unknown product 2 selectivity. This would explain why MeOH conversion and DME production increased with each cycle of the 1:4 bead catalytic test. The removal of the broken down linker by MeOH allowed for effective MeOH conversion at the catalytically active acid sites of the MOF. Unknown product 2 was also observed in the catalytic tests of pure MOF which was not drop-casted. This may be due to the presence of unreacted BPDC linker which was still present.

Further data are required to elucidate the exact structures of the unknown products formed. To improve the stability of the MOF structure it may be beneficial to use an alternative drop-casting agent to the modulator being used for the synthesis of the MOF (i.e., use a different weak acid as a drop-casting agent and acetic acid as a modulator or vice versa) or perhaps forego the use of a modulator entirely. However, excluding a modulator in the MOF synthesis would reduce the number of acid sites present as a lower number of defect sites would be produced which could result in a lower catalytic activity. The effects of using different modulators and drop-casting agents on the number and type of defect sites present in the MOF may be an interesting factor to consider for future catalytic studies.

6. Acknowledgements

I would like to thank my family whose love and support made this thesis possible. I would like to thank the friends I have made in the Netherlands who made life during Covid-19 the best it could be. I would like to thank my supervisors Kordula Schnabl, Christia Jabbour, and Dr. Laurens Mandemaker whose support and guidance helped me to become a better chemist. From the Utrecht University Inorganic Chemistry Department, I would like to thank Dr. Florian Meirer, Dr. Ina Vollmer, Dr. Jochem Wijten, Pascal Wijten, Dennie Wezendonk, Oscar Kerkenaar, Joren Dorresteyn, Sophie van Vreeswijk, and Caroline Versluis

7. References

1. Aizat, M. A. & Aziz, F. Chitosan Nanocomposite Application in Wastewater Treatments. *Nanotechnology in Water and Wastewater Treatment: Theory and Applications*, 243–265 (Elsevier, 2019)
2. Lee, M., Chen, B. Y. & Den, W. Chitosan as a natural polymer for heterogeneous catalysts support: A short review on its applications. *Applied Sciences (Switzerland)*, **5**, 1272–1283 (2015).
3. Gutterød, E. S. *et al.* CO₂ Hydrogenation over Pt-Containing UiO-67 Zr-MOFs - The Base Case. *Industrial and Engineering Chemistry Research*, **56**, 13206–13218 (2017).
4. Ha, J., Lee, J. H. & Moon, H. R. Alterations to secondary building units of metal-organic frameworks for the development of new functions. *Inorganic Chemistry Frontiers*, **7**, 12–27 (2019).
5. Wang, Z. & Cohen, S. M. Postsynthetic modification of metal-organic frameworks. *Chemical Society Reviews*, **38**, 1315–1329 (2009).
6. Batten, S. R., Champness, N. R., Chen, X-M., Garcia-Martinez, J., Kitagawa, S. & Öhrström, L., O’Keeffe, M., Paik Suh, M., Reedijk, J. Terminology of metal-organic frameworks and coordination polymers (IUPAC Recommendations 2013). *Pure Appl. Chem*, **85**, 1715 (2013).
7. Zhou, H.-C., Long, J. R. & Yaghi, O. M. Introduction to Metal-Organic Frameworks. *Chemical Reviews*, **112**, 673–674 (2012).

8. Øien, S. *et al.* Probing reactive platinum sites in UiO-67 zirconium metal-organic frameworks. *Chemistry of Materials*, **27**, 1042–1056 (2015).
9. Katz, M. J. *et al.* A facile synthesis of UiO-66, UiO-67 and their derivatives. *Chemical Communications*, **49**, 9449–9451 (2013).
10. Schoenecker, P. M., Belancik, G. A., Grabicka, B. E. & Walton, K. S. Kinetics study and crystallization process design for scale-up of UiO-66-NH₂ synthesis. *AIChE Journal*, **59**, 1255–1262 (2013).
11. Chavan, S. *et al.* H₂ storage in isostructural UiO-67 and UiO-66 MOFs. *Phys. Chem. Chem. Phys.*, **14**, 1614–1626 (2012).
12. Jambovane, S. R. *et al.* Continuous, One-pot Synthesis and Post-Synthetic Modification of NanoMOFs Using Droplet Nanoreactors. *Scientific Reports*, **6**, 36657 (2016).
13. Lawrence, M. C., Schneider, C. & Katz, M. J. Determining the structural stability of UiO-67 with respect to time: A solid-state NMR investigation. *Chemical Communications*, **52**, 4971–4974 (2016).
14. Cavka, J. H. *et al.* A New Zirconium Inorganic Building Brick Forming Metal Organic Frameworks with Exceptional Stability. *Journal of the American Chemical Society*, **130**, 13850–13851 (2008).
15. Rinaudo, M. Chitin and chitosan: Properties and applications. *Progress in Polymer Science (Oxford)*, **31**, 603–632 (2006).
16. Kärger, J., Ruthven, D. M. & Theodorou, D. N. Metal Organic Frameworks (MOFs). *Diffusion in Nanoporous Materials*, 729–767 (2012), doi:10.1002/9783527651276.ch19.
17. Younes, I. & Rinaudo, M. Chitin and chitosan preparation from marine sources. Structure, properties and applications. *Marine Drugs*, **13**, 1133–1174 (2015).
18. Guibal, E. Heterogeneous catalysis on chitosan-based materials: a review. *Progress in Polymer Science*, **30**, 71–109 (2005).
19. Kalaj, M. *et al.* MOF-Polymer Hybrid Materials: From Simple Composites to Tailored Architectures. *Chemical Reviews*, **120**, 8267–8302 (2020).
20. Subramanian, A. & Rodriguez-Saona, L. Fourier Transform Infrared (FTIR) Spectroscopy. *Infrared Spectroscopy for Food Quality Analysis and Control*, 145–178 (2009), doi:10.1016/B978-0-12-374136-3.00007-9.
21. R. E. Dinnebier, Andy Fitch, S. J. L. Billinge, Armel Le Bail, Armel Le Bail, Ian Madsen, Lachlan M.D. Cranswick, Jeremy Karl Cockcroft, Poul Norby, and A. D. Z. *Powder Diffraction : Theory and Practice*. (2008).
22. Stan, C. v., Beavers, C. M., Kunz, M. & Tamura, N. X-ray diffraction under extreme conditions at the advanced light source. *Quantum Beam Science*, **2**, 4 (2018).
23. Sing, K. S. W. Physisorption of Nitrogen by Porous Materials., *Journal of Porous Materials*, **2**, 5–8 (1995).

24. Geerlings, P., Tariel, N., Botrel, A., Lissillour, R. & Mortier, W. J. Interaction of Surface Hydroxyls with Adsorbed Molecules. A Quantum-Chemical Study. *The Journal of Physical Chemistry*, **88**, 5752–5758 (1984).
25. Becker, C., Braun, T. & Paulus, B. Theoretical Study on the Lewis Acidity of the Pristine AlF₃ and Cl-Doped α -AlF₃ Surfaces. *Catalysts*, **11**, 565 (2021).
26. Egerton, R. F. *Physical Principles of Electron Microscopy: An Introduction to TEM, SEM, and AEM*. (2016).
27. Fan, J. *et al.* Adipose-derived stem cells and BMP-2 delivery in chitosan-based 3D constructs to enhance bone regeneration in a rat mandibular defect model. *Tissue Engineering - Part A*, **20**, 2169–2179 (2014).
28. Nanakoudis, A. EDX Analysis with SEM: How Does it Work? *ThermoFisher Scientific* <https://www.thermofisher.com/blog/microscopy/edx-analysis-with-sem-how-does-it-work/> (2019).
29. Loganathan, S., Valapa, R. B., Mishra, R. & Pugazhenti, G. *Thermogravimetry Analysis for Characterization of Nanomaterials*. (2017). doi:10.1016/B978-0-323-46139-9.12001-8.
30. Schaate, A. *et al.* Modulated Synthesis of Zr-Based Metal-Organic Frameworks: From Nano to Single Crystals. *Chemistry - A European Journal*, **17**, 6643–6651 (2011).
31. Queiroz, M. F., Melo, K. R. T., Sabry, D. A., Sasaki, G. L. & Rocha, H. A. O. Does the use of chitosan contribute to oxalate kidney stone formation? *Marine Drugs*, **13**, 141–158 (2015).
32. Zhang, W., Li, Q., Mao, Q. & He, G. Cross-linked chitosan microspheres : An efficient and eco-friendly adsorbent for iodide removal from waste water. *Carbohydrate Polymers*, **209**, 215–222 (2019).
33. Rivera-Torrente, M. *et al.* Spectroscopy, microscopy, diffraction and scattering of archetypal MOFs: Formation, metal sites in catalysis and thin films. *Chemical Society Reviews*, **49**, 6694–6732 (2020).
34. Sowmya, A. & Meenakshi, S. Zr(IV) loaded cross-linked chitosan beads with enhanced surface area for the removal of nitrate and phosphate. *International Journal of Biological Macromolecules*, **69**, 336–343 (2014).
35. Ruiz, M., Sastre, A. & Guibal, E. Pd and Pt recovery using chitosan gel beads. I. Influence of the drying process on diffusion properties. *Separation Science and Technology*, **37**, 2143–2166 (2002).
36. Sigma-Aldrich. SAFETY DATA SHEET: Biphenyl-4,4'-dicarboxylic acid., 09/01/2022 <https://www.sigmaaldrich.com/IE/en/product/aldrich/225266>.
37. Wang, Z. *et al.* Dialing in Catalytic Sites on Metal Organic Framework Nodes: MIL-53(Al) and MIL-68(Al) Probed with Methanol Dehydration Catalysis. *ACS Applied Materials & Interfaces*, **12**, 53537–53546 (2020).
38. Zhang, W., Li, Q., Mao, Q. & He, G. Cross-linked chitosan microspheres: An efficient and eco-friendly adsorbent for iodide removal from waste water. *Carbohydrate Polymers*, **209**, 215–222 (2019).

39. T.H. Fleisch, A. Basu, M.J. Gradassi, J. G. M. Dimethyl ether: A fuel for the 21st century. *Studies in Surface Science and Catalysis*, **107**, 117–125 (1997).
40. Arrozi, U. S. F., Wijaya, H. W., Patah, A. & Permana, Y. Efficient acetalization of benzaldehydes using UiO-66 and UiO-67 : Substrates accessibility or Lewis acidity of zirconium. *Applied Catalysis A: General*, **506**, 77–84 (2015).
41. Yang, D. *et al.* Structure and Dynamics of Zr₆O₈ Metal–Organic Framework Node Surfaces Probed with Ethanol Dehydration as a Catalytic Test Reaction. *Journal of the American Chemical Society*, **140**, 3751–3759 (2018).
42. Marreiros, J. *et al.* Active Role of Methanol in Post-Synthetic Linker Exchange in the Metal–Organic Framework UiO-66. *Chemistry of Materials*, **31**, 1359–1369 (2019).
43. Zhuang, S. *et al.* Pair sites on Al₃O nodes of the metal-organic framework MIL-100 : Cooperative roles of defect and structural vacancy sites in methanol dehydration catalysis. *Journal of Catalysis*, **404**, 128–138 (2021).
44. Wei, R. *et al.* Tuning the Properties of Zr₆O₈ Nodes in the Metal Organic Framework UiO-66 by Selection of Node-Bound Ligands and Linkers. *Chemistry of Materials*, **31**, 1655–1663 (2019).
45. Yang, D. *et al.* Tuning the Surface Chemistry of Metal Organic Framework Nodes: Proton Topology of the Metal-Oxide-Like Zr₆ Nodes of UiO-66 and NU-1000. *Journal of the American Chemical Society*, **138**, 15189–15196 (2016).
46. Mekala, M. & Goli, V. R. Kinetics of esterification of methanol and acetic acid with mineral homogeneous acid catalyst. *Chinese Journal of Chemical Engineering*, **23**, 100–105 (2015).
47. NIST Mass Spectrometry Data Center. Acetone Mass Spectrum. <https://webbook.nist.gov/cgi/cbook.cgi?ID=C67641&Mask=200#Top>.
48. NIST Mass Spectrometry Data Center. Ethene Methoxy Mass Spectrum. <https://webbook.nist.gov/cgi/cbook.cgi?ID=C107255&Mask=200#Mass-Spec>.
49. NIST Mass Spectrometry Data Center. NIST 2-propenoic acid. *NIST* <https://webbook.nist.gov/cgi/cbook.cgi?ID=C79107&Mask=200#Mass-Spec> (1998).

Supporting info:

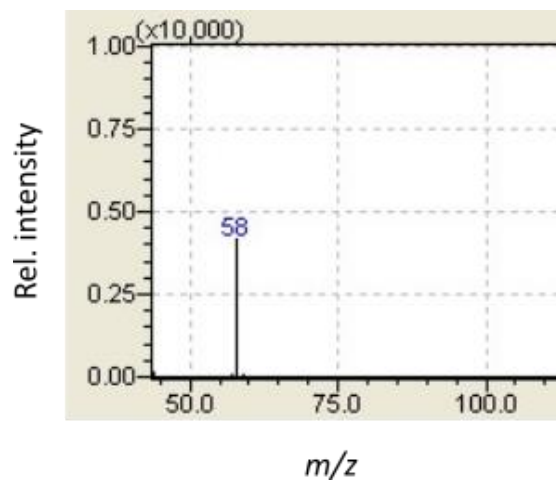


Figure S1. GC-MS spectrum of unknown product obtained at 2.90 minutes retention time

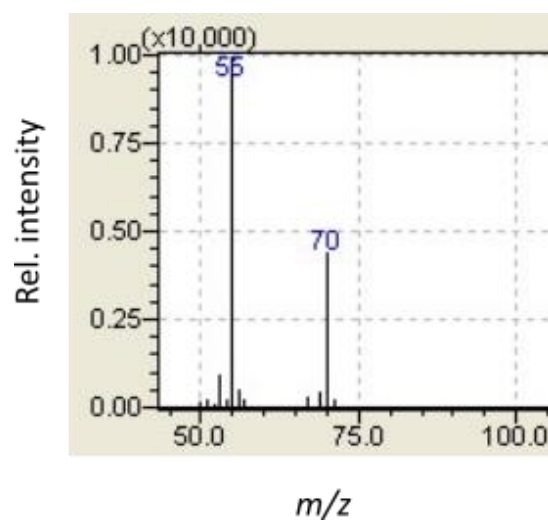


Figure S2. GC-MS spectrum of unknown product obtained at 2.95 minutes retention time.